AD-A138 999 EXPERIMENTAL OBSERVATIONS OF VORTEX RING INTERACTION WITH THE FLUID ADJAC..(U) LEHIGH UNIV BETHLEHEM PA DEPT OF MECHANICAL ENGINEERING AND M.. A W CERRA ET AL. 1/2

UNCLASSIFIED OCT 83 FM-4 AFOSR-TR-84-0130 F/G 20/4 NL

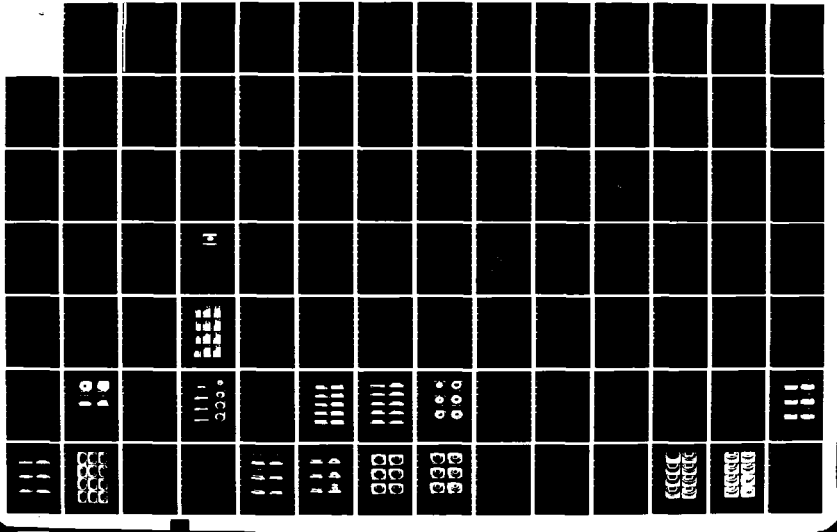

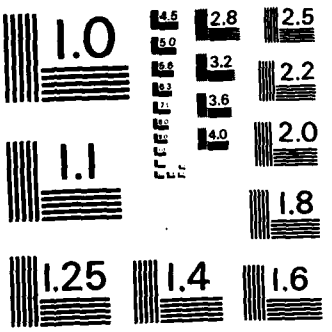

Lehigh University

EXPERIMENTAL OBSERVATIONS OF VORTEX RING
INTERACTION WITH THE FLUID ADJACENT TO A SURFACE

by

A.W. Cerra, Jr. and C.R. Smith

Report FM-4
October 1983

Prepared under Financial Support of
U.S. Air Force Office of Scientific Research
Contract F49620-78-C-0071

Department of Mechanical Engineering & Mechanics
Lehigh University, Bethlehem, PA 18015

UNCLASSIFIED

SECURITY CLASSIFICATION OF THIS PAGE (When Data Entered)

REPORT DOCUMENTATION PAGE		READ INSTRUCTIONS BEFORE COMPLETING FORM
1. REPORT NUMBER AFOSR-TR- 84-0130	2. GOVT ACCESSION NO.	3. RECIPIENT'S CATALOG NUMBER
4. TITLE (and Subtitle) EXPERIMENTAL OBSERVATIONS OF VORTEX RING INTERACTION WITH THE FLUID ADJACENT TO A SURFACE		5. TYPE OF REPORT & PERIOD COVERED INTERIM 6. PERFORMING ORG. REPORT NUMBER
7. AUTHOR(s) A W CERRA JR C R SMITH		8. CONTRACT OR GRANT NUMBER(s) F49620-78-C-0071
9. PERFORMING ORGANIZATION NAME AND ADDRESS LEHIGH UNIVERSITY DEPT OF MECHANICAL ENGINEERING & MECHANICS BETHLEHEM, PA 18015		10. PROGRAM ELEMENT, PROJECT, TASK AREA & WORK UNIT NUMBERS 61102F 2307/A2
11. CONTROLLING OFFICE NAME AND ADDRESS AIR FORCE OFFICE OF SCIENTIFIC RESEARCH/NA BOLLING AFB, DC 20332		12. REPORT DATE October 1983 13. NUMBER OF PAGES 211
14. MONITORING AGENCY NAME & ADDRESS(if different from Controlling Office)		15. SECURITY CLASS. (of this report) Unclassified 15a. DECLASSIFICATION/DOWNGRADING SCHEDULE

16. DISTRIBUTION STATEMENT (of this Report)

Approved for Public Release; Distribution Unlimited.

17. DISTRIBUTION STATEMENT (of the abstract entered in Block 20, if different from Report)

18. SUPPLEMENTARY NOTES

19. KEY WORDS (Continue on reverse side if necessary and identify by block number)

FLUID MECHANICS
VORTEX RINGS
VISCOUS-INVISCID INTERACTION
FLOW VISUALIZATION
BOUNDARY LAYERS
FLOW INSTABILITIES

20. ABSTRACT (Continue on reverse side if necessary and identify by block number)

Experimental studies have been done to examine the breakdown of initially laminar vortex rings during impact with (1) both solid and free surfaces in a quiescent environment, and (2) a solid surface beneath a developing laminar boundary layer. The flow interactions were visualized in water using dye and hydrogen-bubble techniques, and recorded with a high-speed video system. When a vortex ring approaches a surface the resulting flow interaction appears to be chaotic and turbulent, but is actually a very organized viscid-inviscid process which rapidly disperses the vorticity of the vortex ring

DD FORM 1 JAN 73 1473 EDITION OF 1 NOV 65 IS OBSOLETE

UNCLASSIFIED

SECURITY CLASSIFICATION OF THIS PAGE (When Data Entered)

throughout the surrounding fluid. ~~A~~ description of the flow interaction ~~is presented~~ which integrates the following phenomena: 1) the generation of secondary vorticity of opposite sense to that of the vortex ring; 2) ~~the~~ deviations in the trajectory of the vortex ring from that predicted by classical theory; and 3) the processes of ~~the~~ organized dispersal of vorticity. The process by which vorticity dispersal occurs is dependent upon the initial Reynolds number (Re_δ) of the vortex ring. For very weak rings, i.e. Re_o less than 350, vorticity is dispersed by laminar diffusion. For stronger rings, vorticity dispersal occurs discretely through the formation of secondary and tertiary vortex rings (SVR and TVR) via a viscous boundary layer process. Vorticity dispersal continues as a result of Biot-Savart-type interactions of the SVR and TVR with the orginal or primary vortex ring, ~~(PVR)~~. During this interaction the diameter of the SVR is compressed, causing an instability in the SVR which is characterized by an azimuthal waviness. Over the Re_o range 470 to 1600, the amplitude of the waves increases and a loop-structured SVR develops. Over the range 2500 to 3000, the amplitude remains small and a kink-structured SVR develops. These two structures differ not only in wave amplitude but also in how each interacts with the PVR. The former is deformed into loops which wrap around the core of the PVR. The latter is deformed very little and remains essentially ring-like. In both cases, vortex filaments wrap around the core of the PVR causing three-dimensional vortex stretching, decreasing scales of fluid motion, and the breakdown of the PVR. The interaction at the free surface for a vortex ring of moderate Reynolds number appears to be identical to that occurring at a solid surface. Surface tension is thought to be responsible for making the free surface behave similarly to a solid surface with respect to slip, but this could not be proven. The vortex interaction observed for the developing boundary layer flow case behaved similarly to the quiescent flow case, but was strongly modified by the mean velocity gradient at the wall. These modifications include a tilting of the PVR as it approaches the surface and an asymmetric development of the SVR and TVR. Direct similarity of the ring vortex interactions observed here with wall region interactions observed in the wall region of turbulent boundary layers was not found.

(4)

EXPERIMENTAL OBSERVATIONS OF VORTEX RING INTERACTION WITH THE FLUID ADJACENT TO A SURFACE

by

A.W. Cerra, Jr. and C.R. Smith

Prepared under Financial Support of

U.S. Air Force Office of Scientific Research

Contract F49620-78-C-0071

Report FM -4

Department of Mechanical Engineering & Mechanics

Lehigh University

Bethlehem, PA 18015

October 1983

ACKNOWLEDGEMENTS

We would like to express our appreciation to Mr. John Wellman for his assistance in processing the displacement transducer data used in the circulation measurements and to Mr. Tom Doligalski who provided data from his boundary layer analysis as well as assistance in the review of available literature. We would also like to thank Messrs. Fred Wehden, Jim Bunderla and Dick Towne for their timely assistance in the construction of the experimental apparatus. Finally, we wish to thank Mrs. Donna Reiss for her efforts in the preparation of the typed manuscript.

This work was supported by the Air Force Office of Scientific Research and performed under contract ~~F49620-78-0071~~ F49620-78-C-0071 We gratefully acknowledge the continuing support of our research by AFOSR.

A1

TABLE OF CONTENTS

LIST OF TABLES

LIST OF FIGURES

ABSTRACT

Experimental studies have been done to examine the breakdown of initially laminar vortex rings during impact with 1) both solid and free surfaces in a quiescent environment, and 2) a solid surface beneath a developing laminar boundary layer. The flow interactions were visualized in water using dye and hydrogen-bubble techniques, and recorded with a high-speed video system.

When a vortex ring approaches a surface the resulting flow interaction appears to be chaotic and turbulent, but is actually a very organized viscid-inviscid process which rapidly disperses the vorticity of the vortex ring throughout the surrounding fluid. A description of the flow interaction is presented which integrates the following phenomena: 1) the generation of secondary vorticity of opposite sense to that of the vortex ring, 2) the deviations in the trajectory of the vortex ring from that predicted by classical theory, and 3) the processes of the organized dispersal of vorticity.

The process by which vorticity dispersal occurs is dependent upon the initial Reynolds number (Re_0) of the vortex ring. For very weak rings, i.e. Re_0 less than 350, vorticity is dispersed by laminar diffusion. For stronger rings, vorticity dispersal occurs discretely through the formation of secondary and tertiary vortex rings (SVR and TVR) via a viscous boundary layer process. Vorticity dispersal continues as a result of Biot-Savart type interactions of the SVR and TVR with the original or primary vortex ring (PVR).

During this interaction the diameter of the SVR is compressed, causing an instability in the SVR which is characterized by an azimuthal waviness. Over the Re_0 range 470 to 1600, the amplitude of the waves increases and a loop-structured SVR develops. Over the range 2500 to 3000, the amplitude remains small and a kink-structured SVR develops. These two structures differ not only in wave amplitude but also in how each interacts with the PVR. The former is deformed into loops which wrap around the core of the PVR. The latter is deformed very little

and remains essentially ring-like. In both cases, vortex filaments wrap around the core of the PVR causing three-dimensional vortex stretching, decreasing scales of fluid motion, and the breakdown of the PVR.

The interaction at the free surface for a vortex ring of moderate Reynolds number appears to be identical to that occurring at a solid surface. Surface tension is thought to be responsible for making the free surface behave similarly to a solid surface with respect to slip, but this could not be proven.

The vortex interaction observed for the developing boundary layer flow case behaved similarly to the quiescent flow case, but was strongly modified by the mean velocity gradient at the wall. These modifications include a tilting of the PVR as it approaches the surface and an asymmetric development of the SVR and TVR. Direct similarity of the ring vortex interactions observed here with wall region interactions observed in the wall region of turbulent boundary layers was not found.

CHAPTER 1: INTRODUCTION

1.1 BRIEF REVIEW OF VORTEX FLOW LITERATURE

Although vortex flows were studied as long ago as 1867 by Helmholtz (31), the last fifteen years have witnessed a resurgence of interest in and research on such flows in response to many practical problems in engineering and science. Vortex motions are observed in satellite photographs of weather patterns, in turbulent flows such as jets, wakes, boundary layers and mixing layers, and also in the wake of aircraft. These are just a few of the many examples in which vortex flows play a significant role in fluid motion. Vortex flows may also occur in a variety of configurations such as two-dimensional line vortices, vortex sheets, vortex rings, and three-dimensional vortex loops to name just a few. Because the field of vortex study is so broad, it is beyond the scope of this work to provide the reader with a comprehensive overview of all the information on vortex flows relevant to the present study. For such an overview the reader is referred to two excellent review works published in the Annual Review of Fluid Mechanics by Widnall (97) and Saffman and Baker (76).

The review by Widnall (97), entitled "The Structure and Dynamics of Vortex Filaments", was prompted by the interest in trailing vortices produced by large aircraft. Widnall provides a comprehensive review of both the fluid mechanics of trailing vortices and vortex rings, as well as the more general problems of the structure, motion, and stability of free vortices (which she defines as compact regions of concentrated vorticity in free motion in a surrounding fluid that is either homogeneous and at rest or with weak background vorticity or stratification). The topics which should be of particular interest to the reader are her reviews of the governing equations and vortex theorems, and the work done on vortex rings in both ideal and real fluids. Among the topics she considers are the steady motion and the stability of vortex rings.

The other excellent review, written by Saffman and Baker (76) is entitled "Vortex Interactions". Because there is a lack of complete uniformity of terminology in the field, they begin their work by defining many of the commonly used terms such as vortex, vortex tube, vortex filament, and uniform vortex amongst others. Their review is limited to vortices in homogeneous incompressible fluids of negligible viscosity, but covers such topics as: vortex sheets and their stability, the formation of vortices from vortex sheets, and the interactions of two and three-dimensional vortices. Both works provide a fine bibliography of the literature available in the field of vortex flows.

In addition to the two works just presented, the reader should also be aware of several works which deal with the production, initial motion and stability of vortex rings. These works present information which a reader will find helpful in understanding the general formation and behavior of vortex rings.

Maxworthy published three works (51, 52, 53) which deal with experimental studies of both laminar and turbulent vortex rings. Using flow visualization and laser-Doppler velocimetry, he examined the formation process, the flow fields, ring velocities, geometry variations, vorticity, and stability of vortex rings over a wide range of Reynolds numbers.

Didden published two papers (13, 14) in which he examined the variations in velocity, diameter, and circulation of vortex rings which occur between the point of formation and a location three diameters downstream. His earlier work (13) also examines vortex ring stability. His discussion of the difference between the circulation measured at the formation of the vortex ring and that measured three diameters downstream is particularly interesting. This aspect of his work will be discussed further in a discussion of circulation measurements presented in Appendix A.

Guhler and Sallet (23) also examined the formation and initial motion of vortex rings, establishing a good comparison between their results and those from a similar investigation by Didden (13). Their investigation establishes geometric and kinematic relationships between

the vortex ring and the initial cylindrical slug of fluid which forms the vortex ring. In addition to their experimental results, they present a good synopsis of much of the published literature on vortex rings.

Widnall et al. (92, 100, 101) have theoretically and experimentally examined the stability of vortex rings. They have demonstrated that vortex rings become unstable for short azimuthal bending waves, a result that has since been demonstrated experimentally by Didden (13) and Maxworthy (51, 53).

1.2 THE APPROACH OF A VORTEX RING TO A BOUNDARY

When a vortex ring is present in a free fluid far from a boundary, the vortex can be described in an essentially inviscid manner. The relatively small effect of viscosity in real fluids such as water is to cause vorticity to diffuse across the boundary of the fluid moving with the ring, thereby contaminating the surrounding irrotational fluid. This fluid is then entrained into the ring, accounting for the slow increase in size of a laminar vortex ring (53).

When a vortex ring approaches a solid planar boundary, a very complex flow interaction takes place between the fluid in the vortex ring and the fluid adjacent to the boundary. Near a boundary, viscosity may play a significant role in the flow interaction, although there is not universal agreement on this point.

1.2.1 Experimentally Observed Characteristics

When a vortex ring approaches a solid boundary, three characteristics of the flow interaction are commonly observed. The first characteristic is the occurrence of rebound and reversal in the trajectory of the vortex ring (5, 7). As the ring approaches the surface, its axial velocity decreases and its radial velocity and diameter rapidly increase; the ring appears to approach the surface asymptotically as its diameter increases. At some point in this process the ring will pause in its approach to the surface, reverse its axial velocity, and begin to move away from the surface. This axial velocity reversal is referred to as

rebound. In addition, the vortex ring may experience an inversion of its radial velocity which results in a decrease in the diameter of the ring. This inversion in radial velocity is referred to as reversal (7).

The second characteristic of the flow interaction is the formation of a sheet of secondary vorticity along the outer perimeter of the ring close to the solid surface (5, 49, 81, 85, 7). Possessing vorticity opposite to that of the vortex ring, this sheet of vorticity will commonly be observed to roll up into a vortex ring of opposite rotation to the original vortex. To differentiate between the two vortex rings, the original vortex ring is referred to as the primary vortex ring (PVR) and the ring formed from the sheet of secondary vorticity is referred to as the secondary vortex ring (SVR). After formation, the secondary vortex ring will interact with the primary ring in a very complex flow interaction.

The third commonly observed characteristic of the flow interaction has been described as a sudden transition to turbulence after the ring has impacted the surface. Researchers (87) have observed that upon impact the coherent organized flow of the vortex ring is rapidly transformed into a chaotic flow generally associated with turbulence. The more correct way to describe the flow transformation is as a complicated, three-dimensional process in which the vorticity of the primary vortex is dispersed throughout the surrounding fluid in an organized manner (49, 7).

These three characteristics of the flow are all interrelated and must be integrated into any theory which successfully attempts to explain the interaction of a vortex ring with the fluid adjacent to a solid surface. In general, researchers have tried to interpret the flow interaction as either an inviscid process or a viscid-inviscid process.

1.3 THE FLOW INTERACTION: AN INVISCID APPROACH

Simple classical inviscid theory has been used by Helmholtz (31) to predict the behavior of a vortex ring as it approaches a solid planar surface. This theory models the ring approaching a solid surface as a

pair of vortex rings approaching each other along a common axis. The second vortex ring, known as the image vortex ring, models the hypothetical effect of the plate. This theory predicts that the vortex ring radius will become infinite as the vortex travels along a trajectory which asymptotically approaches the solid surface. Some of the assumptions used in this theory are: an inviscid and incompressible fluid, a vortex ring of torroidal shape with a core diameter much smaller than the ring diameter, and a uniform vorticity distribution over the core, outside of which the flow is irrotational (31).

Simple classical inviscid theory fails as a complete model of the approach of a vortex ring to solid boundary in a real fluid. The infinite increase in diameter of the ring predicted by the theory does not occur in any sense for a real vortex ring. The theory also does not predict any of the three commonly observed characteristics of the flow interaction; however, it does appear to adequately predict that part of the trajectory which occurs before the rebound phenomenon takes place. Although the Helmholtz theory fails in close proximity to a surface, there are those who believe that the observed flow phenomena are the result of an inviscid process and have attempted to extend the theory to better predict the real flow behavior.

1.3.1 Classical Theory with Finite Core Size Effects

In 1977 Barker and Crow (2) published an experimental study of the behavior of a pair of two-dimensional line vortices impacting with both solid and free surfaces; they attempted to explain their results by extending potential flow theory to account for finite core size effects. Visualizing the flows in water with fluorescein dye, they recorded the events with high-speed photography, framing at rates of 64 and 200 frames per second. The generated vortex pairs were turbulent with moderately high Reynolds numbers of 25,000 and 75,000 where:

$$Re_o = \Gamma/\nu \qquad (1\text{-}1)$$

and

$$\Gamma = 4\pi S \frac{dh}{dt} \qquad (1\text{-}2)$$

based on an analysis by Lamb (89).

Γ = the circulation of the line vortex

ν = kinematic viscosity

$2S$ = the core spacing of the vortex pair

$\frac{dh}{dt}$ = the propagation velocity of the pair far from the surface

h = the distance from the surface

The purpose of their study was to determine the trajectory and decay rates of a vortex pair in the vicinity of a boundary, an interaction which they felt would be qualitatively similar to that of aircraft trailing vortices in proximity to a runway. Their results are of interest to the present study because the rebound and formation of secondary vorticity should be qualitatively similar to that caused by a vortex ring.

For the three surfaces used in their investigation, smooth, rough and free, they observed rebound, but not reversal in the trajectories. Coincident with the rebound, they observed a decrease in the rate of separation of the cores. After rebound occurred, their data seems to indicate that the vortices remained at a constant height above the plate and reached a finite pair spacing of approximately 5½ times the original spacing. The uncertainty in the final height and pair spacing exists because they do not state the relation of their last trajectory data point to the final dissipation of the vortices.

Their decay rate data takes the form of a plot of "apparent" circulation vs. time, in which the apparent circulation decreases from 700 cm^2/s to a value of 550 cm^2/s after undergoing a series of oscillations supposedly caused by the rebound away from the surface. The circulation Γ is determined from a potential flow theory line-vortex trajectory formula (see (2)) given by:

$$\Gamma = 4\pi q \frac{sh(s^2 + h^2)}{(s^6 + h^6)^{\frac{1}{2}}} \qquad (1\text{-}3)$$

where

q = the propagation speed of the vortex
$((ds/dt)^2 + (dh/dt)^2)^{\frac{1}{2}}$

and s and h are previously defined.

Equation (1-3) does not give the true circulation of the vortex since Barker and Crow measured neither vorticity, nor the exact shape of the core. Since the predicted trajectory differs from the actual trajectory, indicating a deficiency in the theory, it is questionable whether they should even consider using this formula after rebound occurs. They give no other data, quantitative or qualitative, on the decay of the vortices. They also do not report the observation of the formation of secondary vorticity at the solid boundary, even though other researchers (28) who have examined two-dimensional line vortices have reported the generation of such secondary vorticity. Lighthill (44) discusses how vorticity near a surface should produce secondary vorticity of sense opposite to that of the primary vorticity. The one photograph in their report of a vortex adjacent to a boundary seems to show the presence of some secondary vorticity at the outer edge of the vortex pair, although it is impossible to determine this with certainty with just one photograph from the sequence. Since the vortices are turbulent, it is also possible that any secondary vorticity may not be readily observable with the flow visualization techniques they employed.

Their results indicate a deviation between the trajectory predicted by the simple inviscid potential flow theory, which predicts no rebound, and the actual trajectory. They attribute these observed deviations in trajectory to the effects of finite core size, which are neglected in the elementary theory. They suggest that upon impact the circular core will deform into an elliptical shape which may rotate as it moves along the boundary, causing the center of the core to rebound away from the surface. However, no proof of their contentions is presented except for a reference to an unpublished numerical simulation.

1.3.2 Saffman's Analysis of Finite Core Size Effects

To test the validity of Barker and Crow's suggestion that finite core size effects can cause vortex rebound, Saffman (75) performed an inviscid numerical analysis of the impact of a two-dimensional vortex pair with a solid boundary. He modeled the vortices to be elliptical with an axis ratio and orientation given by Moore and Saffman (59, 60) for steady uniform vortices in a steady uniform straining field. Although the validity of the analysis depends on the assumption of steady flow, Saffman does not evaluate the accuracy of this assumption for the flow.

His results show that vortex rebound cannot be explained by finite core-size effects, and that axial velocity cannot change sign as the vortices approach the surface. He further considers the possibility that the rebound of the vortices is only apparent and not real due to a divergence between the centroid of vorticity and the apparent center of rotation of a vortex identified by an observer using flow visualization techniques. Hooker (33) claimed such a divergence was responsible for an observed increase in spacing ratios of Karman vortex streets. After calculating the shapes and paths of the vortices, he found that this effect cannot occur. The trajectories of the centroids of vorticity, which were indistinguishable from those of simple point vortices, and the trajectories of the apparent center of rotation always approached the surface monotonically.

After establishing that inviscid finite core size effects as advanced by Barker and Crow (2) could not explain the observed rebounding, Saffman suggests that a theory by Harvey and Perry (28) which includes the effect of viscosity (published six years before the work of Barker and Crow) provides a more correct explanation for vortex rebound. The work of Harvey and Perry (28) will be discussed later in this introduction.

1.3.3 Classical Theory with Stability Analysis: Schneider and Krauch

Other researchers, Schneider (80-85) and Krauch (38), have attempted to explain the differences in the behavior of a real vortex ring from that predicted by simple classical theory by considering various

instabilities which may occur. Peter Schneider performed many flow visualization experiments with vortex rings in a water tank at the Max Planck Institute fur Stromungsforschung (M.P.I.S.) in Gottingen, West Germany, using essentially the same experimental facility as described in Maxworthy (53). Most of his work is published in M.P.I.S. reports, written in the German language.

In one of his reports (80), he photographically investigated the transformation of laminar and turbulent vortex rings as they approached many different surfaces such as: large and small flat plates, plates with circular holes, small and large circular plates, plates angled with respect to the axis of the ring, cylinders, cones, screens, and a free surface. His results included photographic sequences obtained using a 35mm camera and descriptions of the subsequent interactions, although he does not seem to explain in detail the causes of the interactions. His photographs of the interaction of vortex rings as they impact a flat plate do clearly show the formation of secondary vortices.

In another work (81) entitled Creation, Life, Instability, Regeneration, Dissipation of Vortex Rings, Schneider examined the instabilities of vortex rings as they propagate toward a solid surface. It appears that he uses the instabilities to explain the physics of the interaction through the following model: "a threshold of a new instability is reached, the instability is initiated by a fluctuation which leads to increasing dissipation of the vortex, which in turn causes new instabilities", or by a second model in which "the vortex is in non-equilibrium, dissipation occurs and leads to instability and the formation of new structure followed by an increase in dissipation" (81). In this report Schneider attempts to interrelate the observed rebound of the primary vortex, the formation of the secondary vortex and the eventual dissipation of the vortices through instability mechanisms. Again his results seem more to describe the phenomena, rather than to explain why the phenomena occur. After reviewing his work, the present authors are uncertain as to the exact nature of the instabilities to which he refers, how they arise, their relation to the secondary vortices,

and even why the secondary vortices should occur. It seems as if Schneider claims the secondary vortices arise from some form of instability, but this has not been verified.

In a third report by Schneider (83), entitled The Transformation and Reflection of a Vortex Ring on a Plate Oriented at an Angle to the Translational Velocity, he determined that many of the vortices rebounded away from the plate at an angle equal to one, two, or three times the angle of the plate with respect to the axis of the ring as it approaches the plate. A short discussion of turbulence is included in that work and is continued in a fourth report (84) entitled Experimental Investigation of Phases of Instability of a Laminar Vortex Ring with Respect to Comparable Instabilities in Turbulent Shear, Boundary Layer, and Channel Flows. Because of the lack of an English translation, no further discussion of this report can be given .

Another researcher at M.P.I.S., who performed complimentary research to that of Schneider was Thomas Krauch (38). Krauch comparatively examined the behavior of vortex rings impacting with both solid and free surfaces. His work was also published in German as an M.P.I.S. report. The reader is cautioned that the following comments are based on examination of photographs, diagrams, and translations of a few selected passages.

Krauch determined that rings with slower translational velocities behaved similarly in the vicinity of both solid and free surfaces. A secondary vortex ring forms, develops a wavy structure, and rotates into the center of the primary vortex ring. Parts of the secondary vortex ring are then pulled between the primary ring and the surface. The evidence presented to support this result consisted of trajectories from vortices approaching solid and free surfaces, and photographic sequences of vortices approaching only a free surface, which could presumably be compared to sequences presented by Schneider (80). The trajectories which were compared for solid and free surfaces were very similar and displayed a rebound behavior, although no reversal was observed for these trajectories. A single trajectory of a vortex ring approaching a free surface at a velocity slower than that of the others was presented which did display both rebound and reversal.

At the higher translational velocities the vortex rings behaved differently in the vicinity of the solid and free surfaces. The difference in behavior was due to the deformation of the free surface which occurred as the vortex ring approached it. At very high velocities the vortex ring even rose out of the surface.

Krauch discusses in detail the shape, deformation and rotation of the elliptical vortex core as it nears the surface. A schematic diagram of the relative positions and shapes of the cores of the primary and secondary vortices as the primary vortex follows the path of a trajectory with rebound and reversal is also presented. He fails, however, to do more than describe what he observes; he does not try to explain why certain phenomena occur, nor does he give cause and effect relationships. The causes of rebound and reversal are not explained, nor is an explanation offered for the influence of the secondary vortex on the behavior of the primary vortex.

A theory which attempts to model the behavior of a vortex in the vicinity of a surface must be able to explain the following observations: the formation of secondary vorticity, the occurrence of rebound and reversal in the trajectory of the vortex, and the mechanisms involved in the breakdown or dispersal of the vorticity of the primary vortex. The theories which rely on totally inviscid effects as proposed by Barker and Crow, and Schneider, cannot successfully explain the source of the very complicated flow phenomena which occur during vortex impact.

1.4 FLOW INTERACTION: A VISCID-INVISCID APPROACH

Several researchers have considered the effects of viscosity to explain some of their observations of vortex-surface interactions. When the vortex ring is far from the surface, inviscid theory can be used to adequately describe the behavior of the ring. Near a surface, however, the effects of viscosity may become very important.

When a vortex approaches a surface, viscous effects cause vorticity of an opposite sense to the original vortex to be created due to the boundary layer flow imposed by the presence of the vortex (44). The

boundary layer flow so created can separate at a point beneath the vortex core if the local adverse pressure gradient caused by the vortex is of sufficient strength. This separation creates a sheet of secondary vorticity with rotation opposite to that of the primary vortex (28), which if of sufficient strength will roll-up to form a secondary vortex. Once formed, the secondary vortex will interact with the primary vortex in an essentially inviscid manner.

1.4.1 Harvey and Perry

In 1971, Harvey and Perry (28) published the results of some experimental work which investigated the observed rebounding of the trailing vortex shed from the wingtip of an airplane when that vortex was in the vicinity of the ground. They simulated the flowfield by mounting a wing in a wind tunnel with a moving floor and performed a series of total head surveys to determine the flow patterns.

The boundary layer induced by the trailing vortex was observed to separate because of the local adverse pressure gradient occurring near the point of minimum pressure directly beneath the vortex core. The separated fluid formed a separation bubble which grew rapidly in strength, detaching from the surface to form a secondary vortex. Harvey and Perry could not determine the exact nature of the subsequent interaction of the trailing and secondary vortices, but they were able to determine the effect of the secondary vortex on the trajectory of the trailing vortex. The downward movement of the trailing vortex would be checked and then reversed by the secondary vortex as it rebounded away from the surface. The horizontal velocity would also be checked by the secondary vortex and in some configurations was reversed.

In his review of the previously mentioned paper of Barker and Crow (2), Saffman (75) determined Harvey and Perry's explanation of the observed rebound of a vortex to be the correct explanation for the vortex-solid surface interaction case. He expressed doubt, however, that this explanation could be used to explain the rebound from a free surface observed by Barker and Crow. He reasoned: "since a boundary

layer at a free surface is much weaker than that at a rigid surface (and is in a sense continually separating) it is most unlikely that secondary vortices would be produced in this case as required by Harvey and Perry's explanation. Unless surface contamination in Barker and Crow's experiment had the effect of making the free surface behave like a rigid boundary with respect to slip, then observations that the nature of the boundary had little effect upon the gross properties of vortex motion would suggest an inviscid explanation." (75)

It is probably this suggestion which has prompted some researchers to look for an inviscid explanation. Later results by Schneider (81), Krauch (38) and the results of the present work show that secondary vortices are generated at a free surface. Harvey and Perry's explanation then is a perfectly valid explanation of the observed rebound of the primary vortex away from the free surface, although one can question whether the free surface in the laboratory is actually free of slip. The condition of the surface and the observed behavior will be discussed in more detail in section 3.2 of the results.

1.4.2 Magarvey and MacLatchy

In 1964 Magarvey and MacLatchy (49) published what is possibly the first flow visualization study of a vortex ring impacting a rigid surface. The rings, generated in air by a rapid expulsion from an orifice, were visualized with smoke and recorded using still pictures and 16mm motion picture photography. Observing the interaction that takes place during the violent disintegration process, they found a reproducibility of detail that showed the process was rather organized and not as random as originally thought.

They noted the vortex ring formed at the orifice is not a true ring or closed torroid, but is composed of 2 layers of fluid, one consisting of fluid from the orifice and the other fluid from outside the orifice, rolled about a circular axis. Their observations are interpreted in terms of these fluid layers and their stability.

Their description of the flow interaction is as follows. The secondary vortex ring or "vortex skirt" as they described it, forms from the distortion of the core of the ring upon impact. When the ring impacts the surface, the initial increase in diameter of the axis of rotation occurs without a similar increase in the inside diameter of the ring, thereby distorting the core. An axisymmetric protuberance forms on the outside edge of the distorted core and is in turn distorted by the external velocity field and the rotary motion of the ring to form a multilayered sheet which rolls on itself. (This rolled sheet is the commonly observed secondary vortex.) The velocity field is such that the rolled skirt is carried into the center of the ring where it becomes crimped and fluted. The skirt is severed at the crimped points in its circumference and the vortical motion of the free ends of the segments mutilate the inner layers of the original ring, which results in the breakdown of the ring. They note that the predominant feature of this interaction process is the sharpness of the surfaces demarcating the fluid layers, thus indicating the absence of turbulent mixing. Although Magarvey and MacLatchy do not attempt to classify the interaction as a viscid or inviscid phenomenon, their work is included in this section for a number of reasons, foremost of which is their finding that the assumptions and conclusions of classical inviscid theory are not only unsatisfactory, but also unrealistic. Another reason is that the core distortion, which they observe to be caused by a difference in initial increase in the diameter of the inner and outer parts of the ring, is in reality a viscous or boundary layer effect caused by the interaction with the solid surface. The authors, however, either do not recognize this, or fail to call it to the attention of the reader. Rather, they prefer to discuss the interaction in terms of the stability of fluid layers, although they do not discuss this stability in much detail.

Magarvey and MacLatchy addressed two of the three commonly observed characteristics: that of formation of secondary vorticity and the breakdown of the primary vortex ring, but they made no observations on the trajectory of the PVR other than to state that the diameter does not

infinitely increase, as predicted by classical theory. Their pictures are very good; one can clearly see the crimping of the secondary vortex and the absence of turbulent mixing in the plan-view pictures. Their description of the interaction process is fair; some of their points are subject to debate, particularly the mechanism for generation of the secondary vorticity and the suggestion of the severing of the secondary vortex at the crimped points.

They consider only the effects of the distortion of the core and the velocity field to explain the formation of the secondary vortex and do not consider the effects of viscosity or the formation of boundary layers. They offer no proof for their explanation, citing only the stability of the fluid layers without offering any real discussion of the stability. This author feels that the boundary layer explanation offered by Harvey and Perry is the more correct one based on work done by Doligalski (15) which will be discussed later.

Magarvey and MacLatchy's suggestion that the secondary vortex is severed into segments at the crimped points of its circumference is subject to the interpretation of the photographs. What they describe as severed free ends may really be the cross-sectional views of the core of the secondary vortex which is parallel to the plane of the pictures. The present work will present pictures which show the secondary vortex wrapping around the primary vortex, during which the secondary vortex is not severed.

1.4.3 Boldes and Ferreri

Boldes and Ferreri (5) published a "Research Note" in 1973 on the behavior of vortex rings in the vicinity of a wall. The results of their experimental work imply a confirmation of Harvey and Perry's (28) physical model for the case of an axisymmetric vortex ring.

Vortex rings, formed by the impact of drops of fluid with the free surface of a quiescent tank of water, were filmed at a rate of 100 frames per second as they propagated toward a wall. The interaction was visualized by placing dye in the fluid forming the vortex rings or by placing dye in the fluid adjacent to the wall.

As the vortex rings approached the wall, an axially symmetric vortex sheet with vorticity opposite to that of the ring is formed, as observed in the previous studies cited here. This secondary vortex sheet was observed to rise and enfold the vortex ring. The authors presume that the strength of this secondary vortex sheet was too weak to roll-up into a secondary vortex ring. Boldes and Ferreri basically present trajectory data for the primary vortex ring, all of which indicate rebound to occur as often as twice in each trajectory, although no reversal in the radial velocity was indicated. It is the interaction of the secondary vortex sheet with the primary vortex which causes the rebound in the trajectories. The study of Boldes and Ferreri is basically a further confirmation of the axisymmetric case of Harvey and Perry's model explaining the rebound of a vortex away from a surface. However, they do not provide any insight into the mechanisms by which the primary vortex is dispersed, (i.e. the interaction of the primary and secondary vortices) beyond that of the effect on trajectory of the primary vortex.

1.4.4 Yamada and Matsui

Yamada and Matsui (103) reported the results of flow visualization experiments in which they used two smoke wires, one located at the vortex ring generating orifice and a second located next to a solid surface, to visualize the approach of a vortex ring to a solid surface. They observed the formation of a secondary vortex ring and the associated rebound phenomenon, explaining the formation of the secondary vortex ring using the boundary layer model offered by Harvey and Perry (28) and Boldes and Ferreri (5), although no trajectories were presented. They offered no observations of reversal, nor did they discuss any primary-secondary vortex interaction which could be responsible for the breakdown of the primary vortex.

1.5 ANALYTICAL WORK

1.5.1 Viets and Sforza

In 1972 Viets and Sforza (95) performed a theoretical and experimental study of the motion of bilaterally symmetric vortex rings. From the Biot-Savart law, they calculated the induced velocity at each point on the vortex ring and related the induced velocity to the motion of the ring using either a Hydrodynamic vortex model or a Rankine vortex model. In the Hydrodynamic vortex model the center of the potential vortex is assumed the only point in the velocity field which has vorticity. In the Rankine vortex model, the vorticity is distributed over a small core in solid body rotation with an external irrotational velocity field (95). For more details of the models, the reader should consult Viets and Sforza (95).

The case of a circular vortex ring approaching a solid boundary is analyzed using a Hydrodynamic vortex and an image technique. They expectedly achieved the classical results, with the vortex ring diameter increasing very rapidly in the vicinity of the wall until numerical accuracy was lost. They reported that the theoretical results agreed with the experimental results which were obtained by impulsively starting a circular ring wing to generate the vortex ring. They presented a trajectory of only the theoretical results and did not report any occurrence of rebound, reversal, or the generation of secondary vorticity in their experiments. The apparent absence of secondary vorticity may have been the result of one or more of the following three reasons: 1) an inability to photographically resolve the secondary vorticity; 2) the vortex ring may have been sufficiently weak such that no secondary vorticity could be generated or observed with the visualization techniques they employed; 3) starting vortices generated from a wing have cores which are much smaller relative to the ring diameter than those generated from an orifice (vortex rings with small core designs more closely match the assumptions of the classical model). Due to insufficient information in the reported work, it is not possible for the author to assess which, if any, of these reasons caused the apparent anomaly in the Viets and Sforza work as compared to other previously discussed works.

1.5.2 Schulz-Grunow

Schulz-Grunow (87) analytically and experimentally examined a laminar smoke ring impinging on a surface as a useful means to reveal the mechanism of sudden transition to turbulence. He described the flow as losing its stability all at once with no bifurcation taking place, although he fails to explain in what sense a vortex ring may undergo a bifurcation process. Literally a bifurcation is some sort of division into branches.

He analyzed the real viscous flow by solving the complete Navier-Stokes equations for circular flow where $V_o = \Omega r^{n+1}$ and: V_o = azimuthal velocity, Ω = the strength of the vortex ring $\Gamma/2\pi$, Γ = circulation, r = radius of vortex core, n = an arbitrary constant.

The approach he has taken seems to indicate that the flow of a vortex ring impinging on a surface breaks down randomly and undergoes transition to turbulence very quickly. In performing his analysis, he seems to have lost sight of the physics of the problem. The breakdown of the vortex occurs in a very organized, reproducible manner as described by Magarvey and MacLatchy (49) sixteen years earlier. His assumption that no bifurcation takes place may also be wrong if the dispersal of vorticity through the generation of secondary vortex rings can be considered a bifurcation process.

1.5.3 Doligalski: "The Boundary Layer Induced by a Circular Vortex Ring Impacting a Flat Plate"

In his analysis, Doligalski (15) numerically examined both the behavior of a vortex ring approaching a flat plate and the development of the boundary layer flow induced by the vortex ring. To model the effect of the plate, he used the classical inviscid image vortex technique. A Kelvin-Hicks vortex ring for which the finite sized vortex core is in solid body rotation was assumed. The constants necessary to describe such a ring were derived from experimental data provided by the authors of the present work. When the vortex ring reaches the vicinity of the plate, the effect of viscosity is numerically "turned on", creating boundary layer effects induced by the vortex ring.

Doligalski's solutions reveal an unsteady separation zone to form in the boundary layer beneath the vortex, which takes the form of a closed recirculating eddy with rotation opposite to that of the primary vortex ring. This eddy grows in size, undergoing rapid and explosive growth until the numerical scheme fails. At some point in the evolution of the boundary layer flow, he expects the boundary layer thickness will become thick with respect to the length scale of the outer inviscid flow, whereupon classical boundary layer theory breaks down. The subsequent interaction will then be of a viscid-inviscid nature, with the generation and ejection of a secondary vortex ring out of the boundary layer as experimentally observed by Boldes and Ferreri (5) and Cerra and Smith (7). The primary and secondary vortices will then interact in a primarily inviscid manner (Biot-Savart), with viscous dynamics and ring stability affecting distortion and dissipation effects through inviscid-viscid interactions.

Doligalski's analysis confirms the separation of the boundary layer, reported by Harvey and Perry (28) as the source of the secondary vortex for the axisymmetric case. His work, however, does not attempt to model the subsequent viscid-inviscid interaction between the primary and secondary vortex rings, and therefore cannot reproduce the experimentally observed rebound or reversal of the trajectory of the primary vortex ring caused by this interaction. The author knows of no work to date which has attempted to model this viscid-inviscid interaction. The results of Doligalski's analysis will be compared to experimental results in section 3.1.6 of the results.

1.6 APPLICATIONS

Understanding the physics of the interaction of a vortex ring adjacent to a solid boundary may help one to better understand the role that coherent, vortical structures play in the development of turbulent boundary layers. At one time turbulent flow was considered to be a very disorganized process with random, high frequency velocity fluctuations superimposed on a mean velocity field. Recently, however, observation

of organized coherent structures in turbulent boundary layers (e.g. Kline et al. (37)) has led to the belief that turbulent flows are much more organized than had been thought possible. Vortex structures, as detailed by Head and Bandyopadhyay (29), are commonly observed among the coherent structures in turbulent boundary layers. Several researchers, Doligalski et al. (16), Smith and Metzler (90), and Falco (18), have suggested that the coherent structures observed in a turbulent boundary layer may be the result of the interaction of vortices with fluid near the bounding surface. Development of an understanding of the interaction of a simple vortex ring with a quiescent fluid adjacent to a solid boundary is a first step toward understanding the potential interactions which can occur for three-dimensional vortex loops convecting in a boundary layer.

Another situation, in which vortices exist adjacent to a solid surface, occurs when aircraft are in proximity to airport runways. Pairs of counter-rotating vortices form from the vortex sheet leaving the trailing edges of the wings of large aircraft. During takeoff and landing these vortices may pose a danger to small aircraft using the same runway a short time later. Knowledge of how long these vortices will persist in a coherent organized state before they disperse into homogeneous turbulence would be very useful to aircraft controllers. The work of Harvey and Perry (28) was done in response to the observation made by Dee and Nicholas (11) of actual wingtip vortices in the vicinity of the ground.

1.7 SUMMARY

Deviations in the trajectories of experimentally observed vortex rings appraoching a surface from those predicted by classical theory have been reported by many researchers. They commonly observe the rebound phenomenon, in which the axial velocity of the ring reverses and the vortex "rebounds away" from the surface. Reversal, a process in which the radial velocity reverses and the diameter of the ring decreases, has been less commonly reported, with only Krauch (38) presenting actual trajectories in which this occurred.

When a vortex ring is near the surface, secondary vorticity is generated at the surface along the outer perimeter of the ring. This secondary vorticity can separate and roll-up into a secondary vortex ring which then interacts with the primary vortex ring. This subsequent interaction is apparently responsible for the rebound and reversal phenomena observed in the trajectory of the primary ring as explained by Harvey and Perry (28) and Boldes and Ferreri (5).

The interaction of the two vortex rings is a complicated process of vortex dynamics. Once formed, the secondary vortex orbits above the primary ring and develops azimuthal waves. One group of researchers, Magarvey and MacLatchy (49), describes a process in which the secondary vortex ring is severed in a few azimuthal locations. The severed ends of the SVR then mutilate the primary vortex in a process which leads to the destruction of the organized vortex flow. Another group of researchers, Schneider (81) and Krauch (38) describe a process in which the wavy ends of the SVR are not severed, but rather are pulled under the PVR. In both studies there appears to be room for improvement in both the illustration and explanation of the processes which lead to the ultimate dispersion of the primary vortex ring.

Researchers, who have examined the impact of vortices with both free and solid surfaces, have reported that the surface condition made little difference in the type of behavior observed.

1.8 OBJECTIVES

To date, it appears that no one has successfully integrated all three aspects of the flow interaction: the rebound and reversal phenomena, generation of secondary vorticity, and dispersal of primary ring vorticity, into one coherent and accurate discussion. The motivation for this work is to provide such an integrated description and explanation of the behavior of a vortex ring impacting with a solid surface.

Trajectories of primary vortex rings displaying not only rebound but also reversal will be presented. In addition, trajectories of secondary and tertiary vortex rings will be presented with the

trajectories of primary rings to more clearly illustrate how the phenomena of rebound and reversal occur.

Photographic sequences will be presented which show the generation of secondary vortex rings and the subsequent interaction of those rings with the primary vortex ring. The details of this interaction process will be illustrated by a series of visualization pictures which demonstrate how the vorticity of the primary vortex ring is dispersed. Vortices over a range of Reynolds numbers are examined and the various modes of vorticity dispersion demonstrated by the vortex impact phenomena are categorized and interpreted.

To examine the effect of surface conditions, the interaction of vortices approaching solid surfaces will also be compared with the interactions occurring at a free surface.

A secondary objective of this work is to examine the vortex ring-surface interactions as a potential flow structure contributing to the behavior of turbulent boundary layers. To further explore this suggestion, the interaction of a convecting vortex ring impacting a solid boundary beneath a developing laminar boundary layer is examined and the visualization results interpreted in relation to comparable visualizations of fully turbulent boundary layers.

CHAPTER 2: EXPERIMENTAL APPARATUS

2.1 INTRODUCTION

All experiments reported in this work were performed in the water channel flow facility located in the Fluid Dynamics Research Laboratory of Lehigh University. Vortex rings with a range of characteristics were generated by a vortex ring generator, designed and constructed at Lehigh University. Visualized with dye and hydrogen bubble techniques, the interaction of a vortex ring with the fluid adjacent to a surface was recorded using an INSTAR high speed video system. The experiments were performed for three configurations: solid surface, free surface, and a developing boundary layer.

2.2 FLOW FACILITY

The flow facility is the same as that described in Metzler (54), suitably adapted for this study. Shown schematically in figure 2.1, the facility consists of a free-surface channel in which water is circulated from one end of the channel to the other by a horizontal split-case centrifugal pump, the interior of which was coated with epoxy paint to minimize corrosion contamination of the water. The pump is powered by a variable speed, feedback controlled, 7½ horse-power, D.C. electric motor capable of circulating the 5.0 cubic meters of water in the system at a rate of 4.0 cubic meters per minute.

The water enters the inlet tank from a distribution manifold pipe and rises vertically through a 15 cm. thick plastic sponge. The flow then passes through a flow straightener consisting of honeycomb cells (7.5 cm long and 0.48 cm diameter) followed by two 20 mesh stainless steel screens (45) set 2 cm apart. A 1.75:1 inlet contraction (45) connects the inlet tank to the working section of the channel and further reduces freestream turbulence.

The working section of the channel is constructed of 1.91 cm thick plexiglass plate supported by 5 cm square steel tubing at a

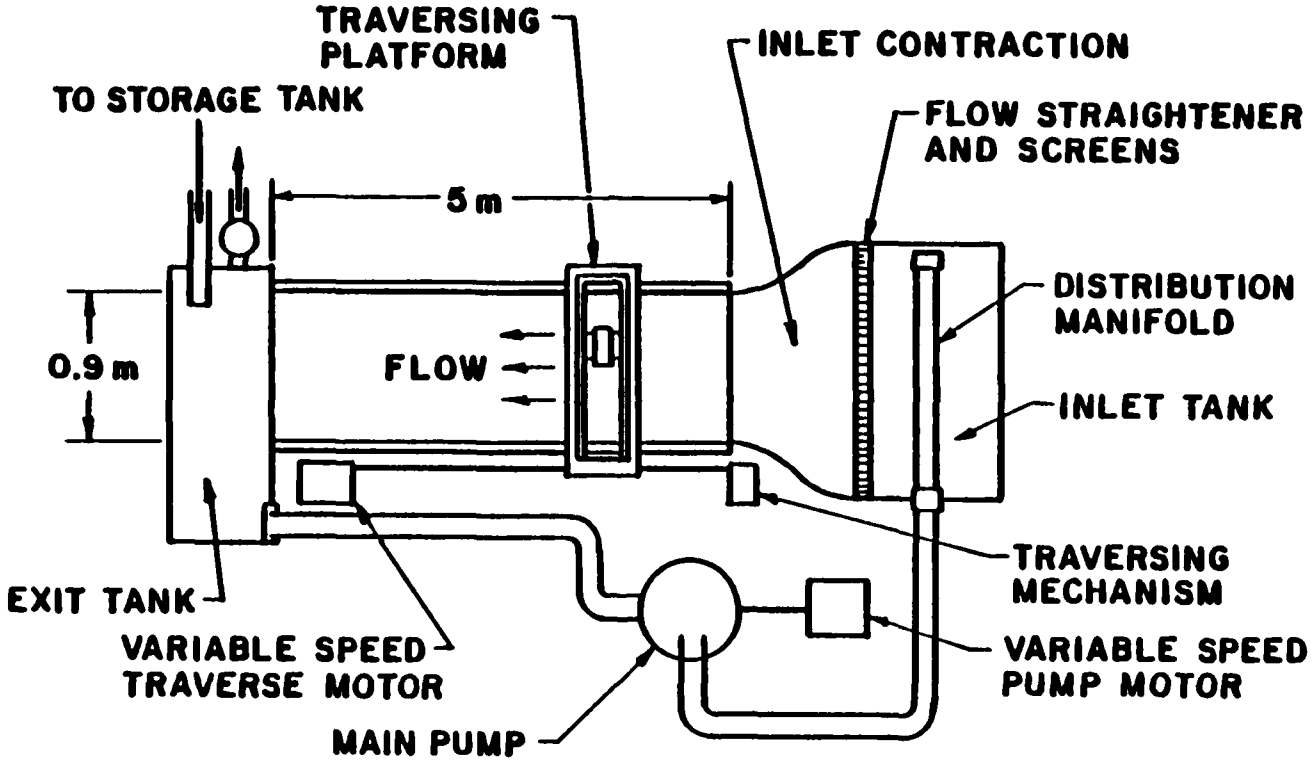

Figure 2.1 Plan - view schematic of water channel flow facility.

height approximately 1 m above the floor. This section has a depth of 40 cm, width of 88 cm, and length of 5 m.

At the termination of the working section, a folded 20 mesh stainless steel screen is placed at the entrance to the exit tank to 1) inhibit the formation of standing waves at the end of the channel and 2) prevent the upstream propagation of any disturbances originating in the exit tank. The pump circulates the water from the exit tank back to the inlet tank.

2.3 TRAVERSING PLATFORM

A traversing platform capable of traveling the length of the channel is mounted above the channel working section as shown in figure 2.1. Supported by two linear motion ball bushings and two ball bearing cam followers, the platform rides on two steel rails mounted above and on either side of the channel. An end-on view of the water channel and traversing platform is shown in figure 2.2. A cable/pulley system powered by a one horsepower, reversible, variable speed electric motor with dynamic braking can propel the platform at translational speeds from 0 to 0.5 m/s. A second traversing platform located beneath the channel is driven by a second cable/pulley system interconnected and synchronized to the first cable/pulley system by a chain/sprocket assembly.

In figure 2.2, the vortex generator and two video cameras providing side and plan-views are shown mounted on the upper platform, which is also used as a mount for other apparatus such as hydrogen bubble-probes (not shown). The lower platform is used primarily to mount lighting equipment. The unique feature of this traversing platform system is the capability to perform flow visualization from a frame of reference moving with the flow.

2.4 VORTEX GENERATOR APPARATUS

Single vortex rings were produced by ejecting slugs of fluid through a sharp edged orifice. After ejection, the moving body of fluid rolled up into a vortex ring (more precisely, into the shape of an oblate spheroid).

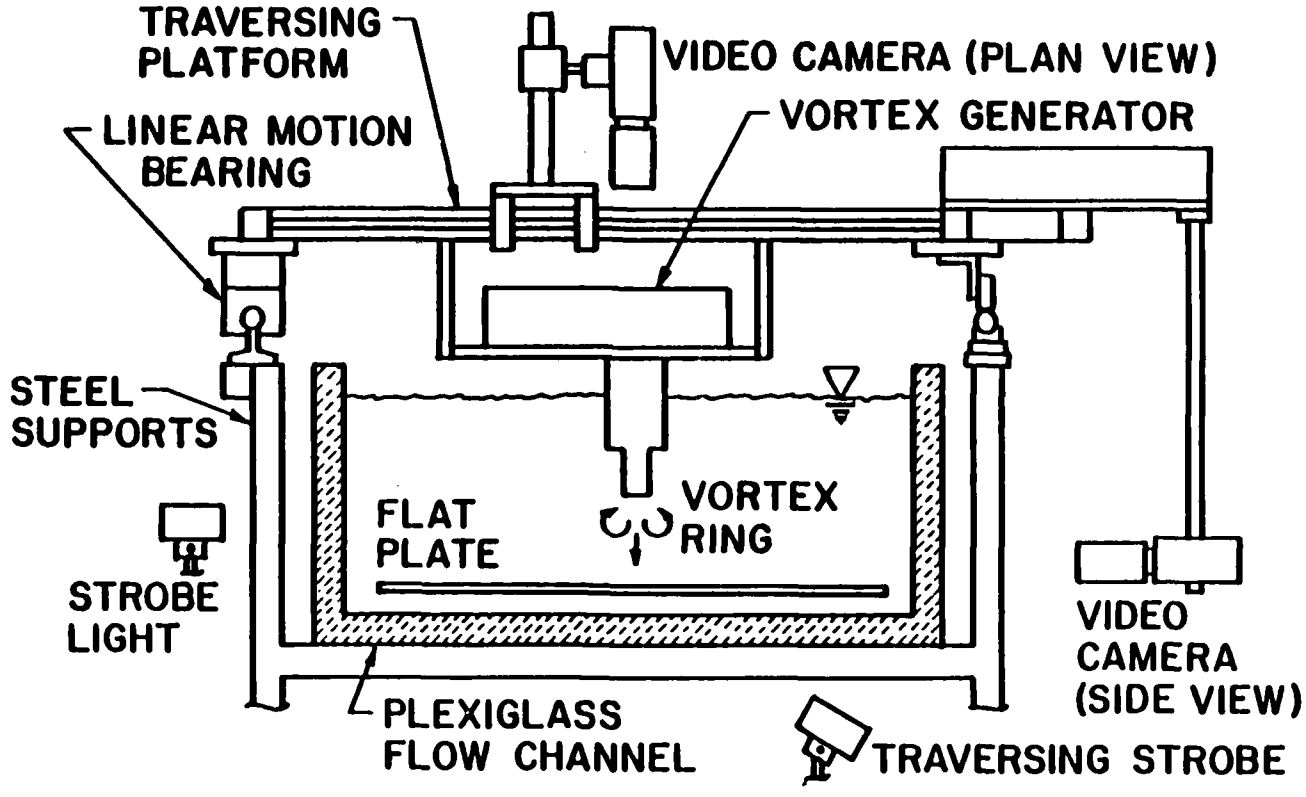

Figure 2.2 End-on view of water channel (looking downstream) and traversing platform.

Shown schematically in figure 2.3, the vortex generator is powered by a 0.044 horsepower, variable speed, reversible, direct current electric motor connected to a ball bearing lead screw by an electric clutch. The lead screw converts the rotary motion of the motor to linear motion of a piston via a constant velocity cam follower mechanism. Movement of the piston pushes fluid through the orifice. As shown in figure 2.2, the generator is attached to the traversing platform above the water with the piston, cylinder, orifice tube, and orifice submerged in the water. All parts exposed to water are made from PVC plastic to resist corrosion.

The generator was designed to have interchangeable parts which allow the generation of vortex rings over a range of characteristics. The motor speed is continuously variable up to a speed of 7400 rpm. Cams with stroke lengths of 0.64, 1.27, 1.9, and 2.54 cm are available. Stroke lengths between these values can also be obtained by adjustment of electrical and mechanical stops (not shown in figure 2.3). Piston stroke is measured by a variable reluctance displacement transducer. Piston diameters of 1.9, 2.54, 3.81 and 5.08 cm and orifice diameters of 0.95, 1.43, 1.90, 2.22, 2.54, 3.18, and 3.81 cm are available. Various combinations of stroke length, piston size, and orifice diameters allowed an examination of L_M/D_M ratios from 0.75 to 3.41, where L_M is the length of the cylindrical slug of fluid ejected from the orifice and D_M is the orifice diameter. Employing orifice tubes of different lengths, the H_M/D_M ratio, where H_M is the height of the orifice from the surface and D_M is the orifice diameter, can be varied over a range of values from 2.85 to 6.8. The ability to vary this ratio is important since the vortex ring must have sufficient distance to fully form or roll-up before it encounters the wall. Saffman (74) reports that rollup is not complete until the ring has moved several ring radii away from the orifice. Likewise, Sallet and Widmayer (79) report that vortex rings are fully developed within three ring diameters downstream from the generating orifice. All the vortices studied in these experiments were fully developed before they were close enough to the surface to be affected by it.

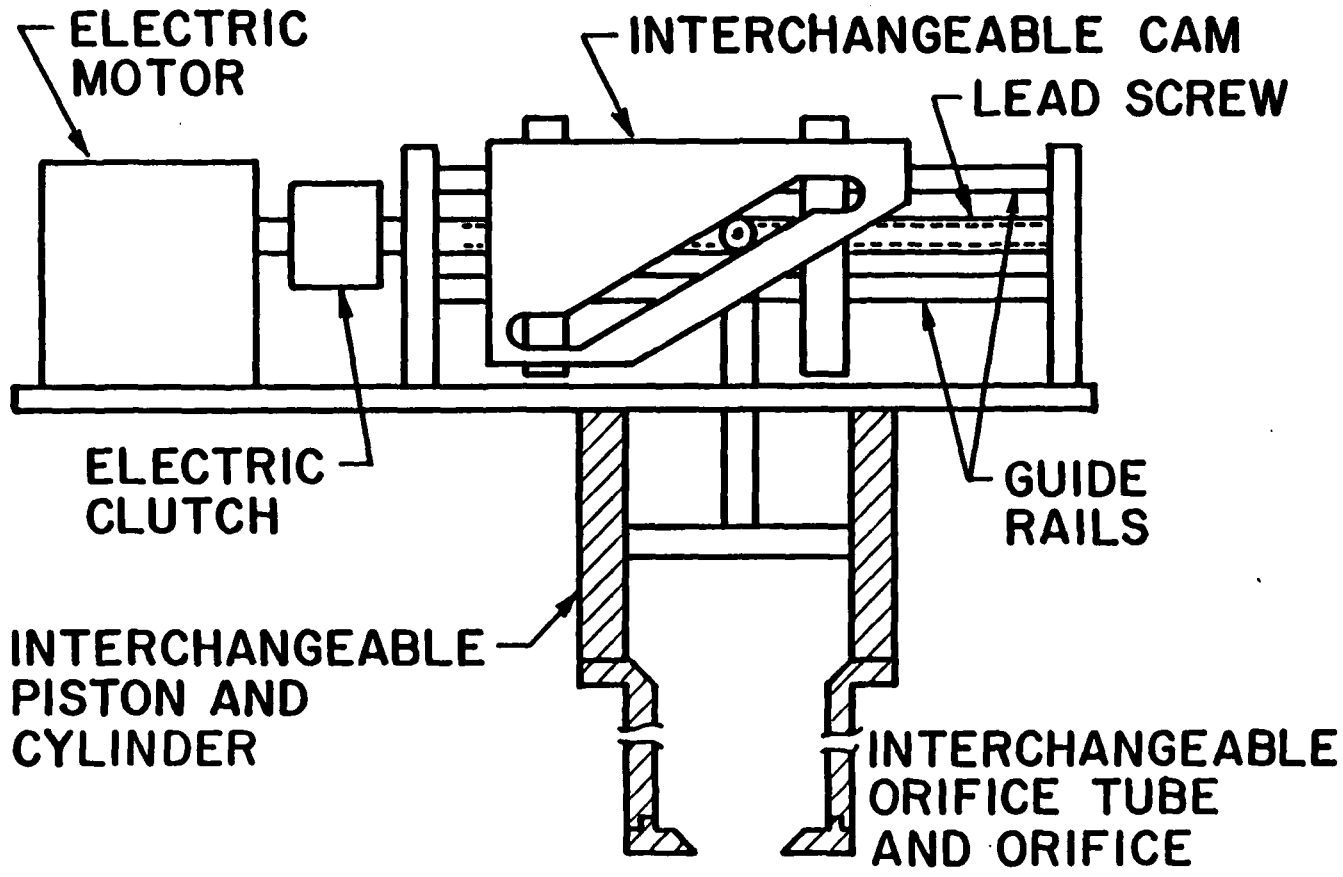

Figure 2.3 Vortex generator apparatus

The quantities which characterize the fully developed vortices are the initial vortex ring diameter, D_o, the initial vortex ring velocity, V_o, and the initial Reynolds number, Re_o. Ring diameters ranged from 1.02 to 3.38 cm and ring velocities from 0.61 to 5.63 cm/sec. The Reynolds number, Re_o, based on these two quantities and the kinematic viscosity of the water, varied from 105 for a very laminar ring to 4943 for a turbulent ring.

Two other characteristics of interest in regard to vortex rings are the stability of the vortex before impact with the surface and the circulation of the vortex as a measure of its strength. All results reported in this study are based on the interaction of laminar vortex rings which were stable prior to impact with the surface. A discussion of vortex ring instability prior to impact is included in section 3.4 of the Results. In addition, several attempts were made to experimentally measure the circulation of the vortex rings directly; however, these studies met with only limited success. The results of these studies and results of other researchers are discussed in Appendix A.

To evaluate all the characteristics of interest for a particular vortex ring, it was necessary to perform multiple observations for each set of ring parameters, which required a vortex generator capable of producing a series of vortex rings with identical characteristics. The repeatability of the generator was tested by configuring the generator to produce a vortex with a particular set of characteristics at two different times during the course of the experimental program, between which the generator was reconfigured to produce other vortex rings. The characteristics of the fully developed vortex ring, i.e., Reynolds number, ring diameter, and translational velocity, were evaluated for each case and were found to be repeatable to within $\pm$4%, $\pm$4.5%, and +1%, respectively. These values fall well within the experimental measurement errors, which are recorded in the uncertainty analysis section of appendix B. The interaction of the vortex ring with the fluid adjacent to a solid boundary was also qualitatively observed for each case and found to be very similar, if not identical. For each type of vortex ring studied, a number of realizations were required to perform

all of the necessary observations. The flow behavior appeared to be essentially identical for each realization of a particular type of vortex ring. From these sets of observations, it was concluded that the generator is capable of repeatedly producing vortex rings with identical characteristics.

2.5 FLOW VISUALIZATION TECHNIQUES

Two flow visualization techniques, dye and the hydrogen-bubble method, were employed in this study. The dye technique proved most useful for qualitative visualization of the complex, three-dimensional nature of the flow interactions. The hydrogen-bubble technique was most useful in determining quantitative information such as ring diameter and velocity of propagation.

2.5.1 Dye Visualization

One method of dye visualization utilized the injection of dye from a hypodermic syringe into the fluid within the vortex generator orifice tube just prior to the generation of a vortex ring. Figure 2.4 shows a vortex ring visualized by this method. The dye used was a 1:10 mixture of blue food coloring and water; the blue color was determined to provide a better contrast than other available colors such as red and green. One injection of dye proved to be sufficient for the visualization of four or five vortex rings.

The placement of dye in the primary vortex ring (PVR) is an effective means for visualizing the three-dimensional flow interactions of the PVR with the fluid adjacent to the surface. Because the secondary vortex ring (SVR) partially consists of dyed fluid from the PVR, it too is visualized by the initial placement of dye in the orifice. However, as the interaction of the two vortices progresses, the dye becomes more diffuse which makes the motions of the individual vortex ring elements more difficult to distinguish. To alleviate this difficulty a second dye technique was used.

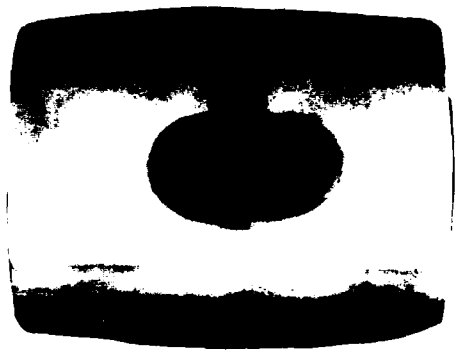

Figure 2.4 Vortex ring approaching a solid plane surface (side view, dye placed in vortex ring). Vortex propagating from the top to the bottom of the picture. Vortex I.D. #51.120, Re_o = 560.

This second technique employed a layer of dye adjacent to the solid surface created by slowly injecting dye over a region of the surface using an elongated needle and hypodermic syringe; with this technique no dye was placed in the orifice tube. Using this method, one could clearly observe the formation of the secondary vortex from fluid adjacent to the surface and follow the subsequent interaction of the secondary vortex through most of the interaction process. Because it contained no dye, the interior of the primary vortex ring was not visible, only the outline of and the effects of the primary vortex could be observed.

These two dye techniques do have some drawbacks. Because the dyed fluid is slightly heavier than water, the dye placed in the orifice tube had a tendency to seep out of the orifice and into the experimental field of view, creating obvious viewing difficulties. Although the density difference could be used to advantage in the second dye technique, it too had its associated difficulties. It was difficult to place a uniform sheet of dye adjacent to the surface using a syringe; additionally, this sheet had to be replaced for each ring generated. Both dye methods tended to introduce a large amount of dye into the test section, especially when visualizing the larger-sized vortices. After every few runs, it was necessary to briefly start the water channel in order to move the dyed water out of the experimental region. An appropriate period was then required to allow the water in the test section to settle back into a quiescent state. Although the relatively large fluid capacity of the channel system allowed a large amount of dye to be absorbed without significant loss of clarity, it frequently became necessary to drain and refill the system when the dye build-up in the water prevented good picture contrast.

When using dye to visualize vortex flows, one should also be away of a problem noted by Maxworthy (51): the entire region of developing vortical fluid is not shown by the dye in a vortex ring because the diffusion coefficient of the dye particles is very much smaller than the diffusion coefficient for the vorticity, i.e., the kinematic viscosity.

2.5.2 Hydrogen Bubble Visualization

A second method of flow visualization employed was the hydrogen-bubble method as described by Clutter et al. (9) and Schraub et al. (86). A fine platinum wire (.025 mm diameter) is used as the cathode of a DC circuit and placed in the flow. A carbon rod, serving as an anode, is placed nearby. A square wave voltage pulse generator supplies the current for the electrolysis process which forms a sheet of hydrogen bubble lines at the wire. Construction of the probes used and the voltage generator are described in Metzler (54).

For the experiments in which the vortex ring impacted a developing boundary layer, a special hydrogen-bubble probe was constructed which allowed the orifice of the vortex generator to pass over the probe which was mounted stationary relative to the surface. In these experiments, to generate a vortex ring which convected with the flow, it was necessary to move the vortex generator downstream with the flow. A "U" shaped hydrogen-bubble wire support was mounted in a plane parallel to the surface, across which a bubble wire was attached in the spanwise direction of the channel. One end of a vertical support was attached to the "U" shaped support in an offset, cantilevered manner; the vertical support angled up out of the plane of the "U" in such a manner as to allow the vortex generator orifice to pass over the "U" without interfering with the vertical support as it convected downstream. The other end of the vertical support was attached to the side wall of the channel by means of a traversing mount which allowed the probe to be raised or lowered. The probe was constructed of telescoping square brass tubing, insulated with plastic heat shring tubing, with the smallest cross sections of brass tubing located near the bubble wire so that the flow disturbance near the wire was minimized.

Because the hydrogen bubble method only visualizes the flow which occurs in the plane of the sheet of bubbles, it is not as useful as the dye techniques for visualizing three-dimensional vortex interactions. The bubble method is more useful, however, for obtaining quantitative information such as ring diameter, core size, and core rotational velocities. If a photograph of a ring visualized by dye (figure 2.4) is used

to establish the diameter of the ring, (i.e., the distance between the centers of the two cores) it is difficult to identify the exact positions of the core centers because of the diffuse characteristics of the dye. This task of core identification is performed more easily with the hydrogen-bubble method because the bubbles will be driven toward the center of minimum pressure at the core, creating a bright region which makes the identification of the center of the vortex core particularly easy. In general, the hydrogen-bubble method is one of the better flow visualization methods available for obtaining quantitative information because of the production of discrete markers in the flow.

2.5.3 Water Quality

To insure good quality photographic data, clean water, free from particulates and algae was necessary. The system was filled with water filtered by 1 micron (μm) cotton wound filters. To control the growth of algae and bacteria, copper sulfate ($CuSO_4 \cdot 5H_2O$) in granular form was added to the water in concentrations of 5 to 20 g/m^3 as recommended by the Degremont Water Treatment Handbook (12). Plexiglass covers for the channel and end tanks and a continuous 1.1 m^3/hr filtering system were used to prevent the accumulation of particulate matter.

When the hydrogen bubble method was used, an electrolyte, sodium sulfate ($Na_2 SO_4$) was used in concentrations of 0.15 g/liter to facilitate the electrolysis process.

2.6 VIDEO EQUIPMENT

Once the flows were visualized, they were viewed and recorded using a two-camera INSTAR high-speed video system manufactured by the Video Logic Corporation. Framing at a rate of 120 frames/second, the cameras are synchronized with strobe lights to achieve an effective shutter exposure time of 10^{-5} sec. With conventional zoom and close-up lenses, the cameras can provide fields of view as small as 6mm x 6mm at a distance of 0.5m. The viewing screen is a 250 line direct overlay

raster display with a sweep frequency of 25.2 KHz. Using two cameras, the system has a split-screen capability which allows the simultaneous viewing of two different fields-of-view. Photographic data, recorded on a 1 inch magnetic tape recording unit, can be played back at real-time forward speeds and in flicker-free forward and reverse slow-motion. Slow-motion forward playback can be done at speeds continuously variable from 0 to 15 percent of real-time speed. Frame-by-frame and stop-action capability allows further detailed analysis of the recorded data. Individual pictures can be obtained using either 1) a videographic copier (a latent image process using heat developed dry silver paper) which interfaces directly with the video recorder or 2) conventional photographic methods. The majority of photographs presented in this work were obtained using Type 57 Polaroid film and a Polaroid back for a 4x5 Graflex camera. The video system is described in greater detail by Smith (89).

Figure 2.5 shows the viewing angles employed for the two cameras. Since the vortex generator obscured conventional plan-views of the vortex impact, oblique plan-views were taken with the camera offset to the side of the vortex generator as shown. To obtain a sharp oblique plan-view, a plexiglass viewing box was used to prevent the distortion caused by diffraction of the light rays at the surface of the water. Lighting equipment consisted of two 90 watt and one 1000 watt strobe lights (synchronized with the cameras) and two auxiliary quartz studio lamps employed for difficult lighting situations. For the dye visualizations, white plastic backgrounds were used with backlighting techniques. The strobe lights were mounted as shown in figure 2.2. For hydrogen-bubble visualization, a black background was used with the strobe lights directed at an oblique angle ($\sim$35°) to the line-of-sight of the cameras.

2.7 SCOPE OF EXPERIMENTS

The experiments examined the interaction of stable laminar vortex rings with three types of surfaces: a smooth solid surface, a free surface, and a smooth surface with a developing laminar boundary layer.

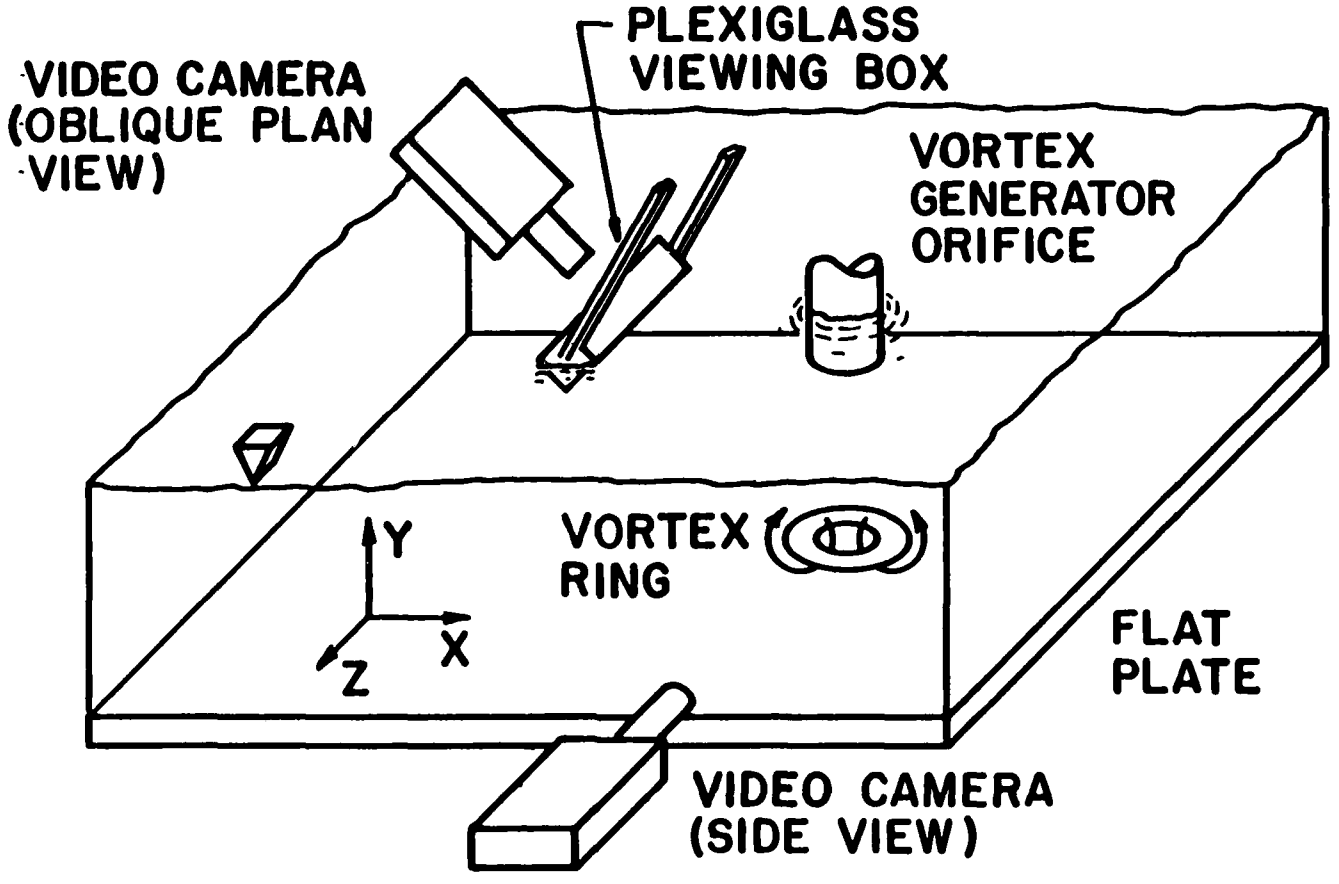

Figure 2.5 Perspective view of camera viewing angles and coordinate system orientation.

The visual data included video sequences taken for both qualitative observation of behavior and for quantitative evaluation. Six hours of video tape were recorded, consisting of 2530 separate vortex sequences, or approximately 2,127,000 individual picture frames. The 2530 recordings represent about one half the number of times the vortex generator was actually operated, a period over which the repeatability of the generator was very good. The generator was used to generate 93 different types of vortex rings and interactions with approximately 25 separate video sequences recorded for each type.

2.7.1 Solid Surface Condition

Of the three surface conditions, the solid surface was the condition most comprehensively studied, representing 83 of the 93 types of vortex interactions examined. Of these 83 cases, 19 cases (23 percent) were unacceptable for inclusion in the results presented here because they were either unstable at impact, turbulent, or improperly formed. Although not included in these results, these unacceptable cases often provided some insight into the interaction process.

Because the primary objective of this work was an understanding of the three-dimensional flow interactions, the dye visualization methods were used for most of the solid surrace cases. The hydrogen bubble method was used for a limited number of cases to obtain data for circulation calculations which are presented in Appendix A.

2.7.2 Free Surface Condition

To perform the free surface experiments, a "U" tube attachment to the vortex generator, shown in figure 2.6, was used to generate vortices which would propagate towards the surface of the water channel. Only one type of vortex ring, visualized with dye techniques, was generated with the free surface boundary condition. The free surface results were compared directly with solid surface interaction by impacting the vortex ring with a flat plexiglass plate device floated on the water surface.

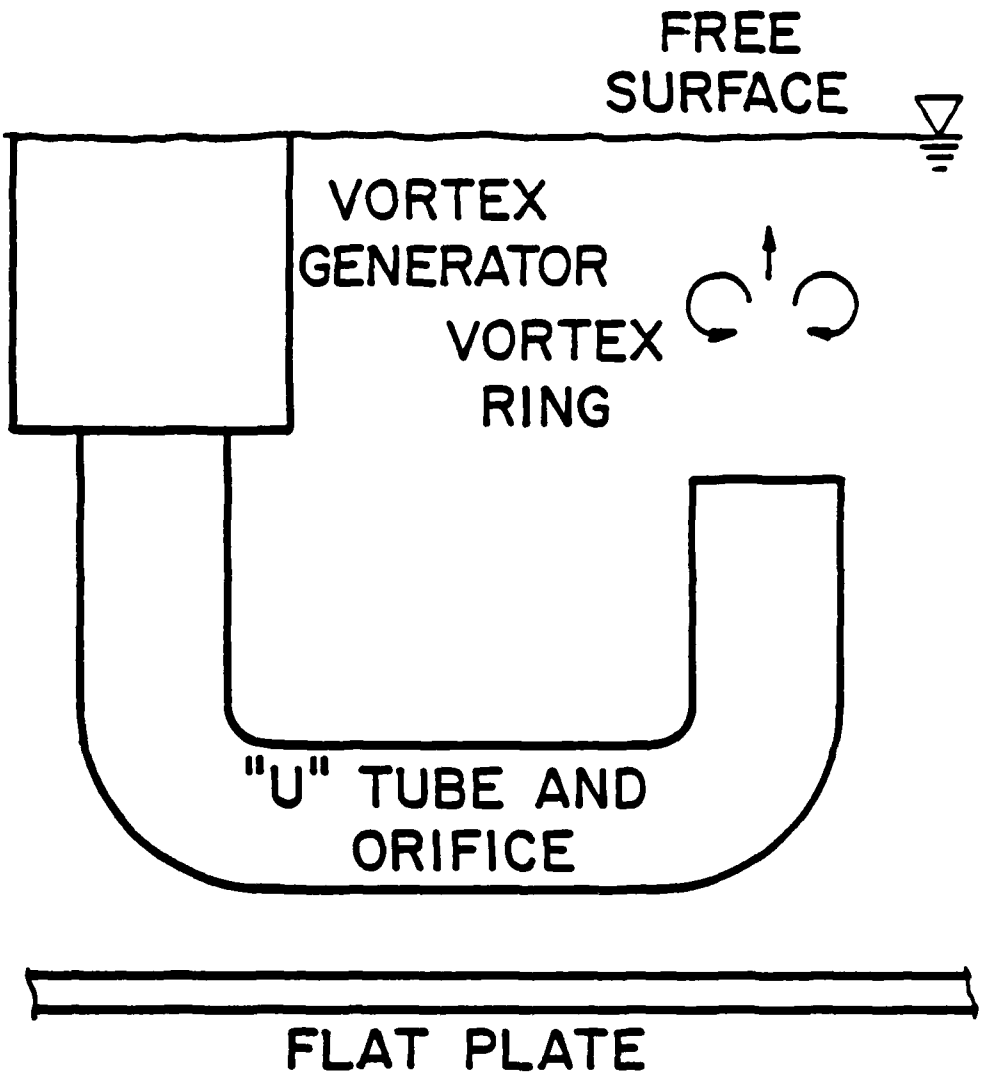

Figure 2.6 Diagrammatic side view of a vortex ring approaching a free plane surface.

2.7.3 Boundary Layer Surface Conditions

A schematic diagram of a vortex ring approaching a laminar boundary layer is shown in figure 2.7. The traversing platform, convecting at the freestream velocity, allowed the generation of a vortex ring with a convection velocity equal to the freestream velocity; thus the vortex ring behaved in a manner consistent with generation in a quiescent environment until it penetrated the developing boundary layer prior to impact with the plate surface. Nine types of vortices were examined, of which two were studied in detail. The flow interactions were visualized using dye and hydrogen-bubble methods. The bubble methods were particularly useful in visualizing the boundary layer and evaluating boundary layer characteristics.

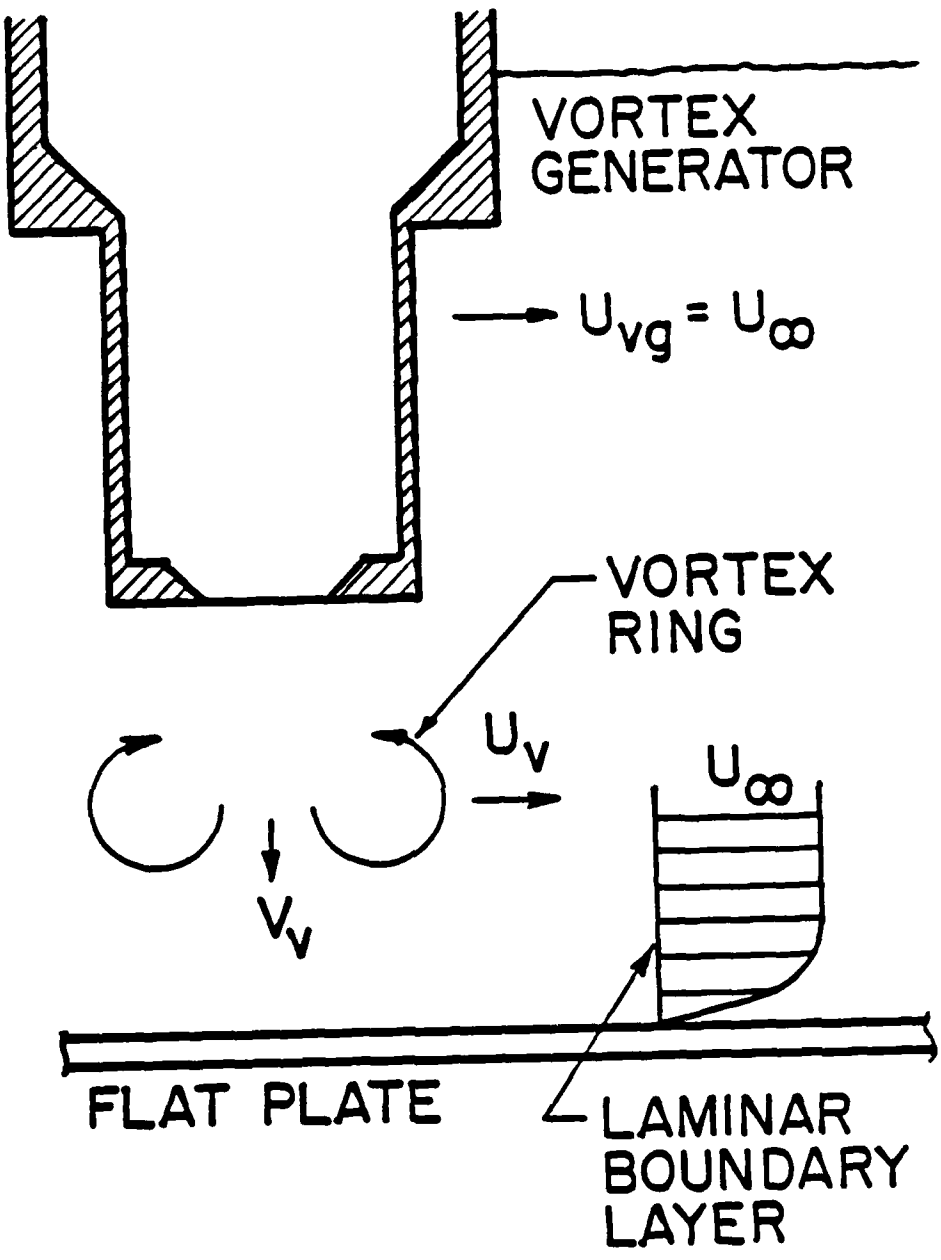

Figure 2.7 Diagrammatic side view of a vortex ring approaching a laminar boundary layer above a solid plane surface.

CHAPTER 3: RESULTS AND DISCUSSION

3.1 IMPACT OF A VORTEX RING WITH A SOLID SURFACE: QUIESCENT FLOW

3.1.1 Introduction

The trajectory of a vortex ring approaching a solid surface through a real fluid is not the same as that predicted by classical inviscid theory. The diameter of the ring remains finite, and the core of the vortex may rebound away from the surface. Presently there is disagreement over why the actual trajectory of the vortex core deviates from that predicted by classical theory. Some feel that the deviation is the result of an inviscid instability mechanism, while others feel that a viscid-inviscid explanation is more appropriate. The authors agree with the latter viewpoint and will attempt to provide evidence which supports this viewpoint.

Another common conception is that the impact of a vortex ring with a solid surface results in the rapid transformation of the flow from one with a very orderly structure to one with a chaotic structure associated with turbulence. Although the transformation to turbulence appears to take place very chaotically (87), this transformation is actually a very organized process in which the vorticity of the vortex ring is rapidly dispersed into a larger volume of fluid through decreasing scales of fluid motion created by a series of complex, but symmetric vortex interactions. The present work will illustrate the flow phenomena which are responsible for this degeneration of the vortex ring into an apparently "turbulent" state.

The flow phenomenon which appears to be responsible for both the deviation in the trajectory from that predicted by classical theory and the rapid dispersal of the vortex ring is the generation of secondary vorticity by viscous effects as the vortex ring approaches a solid surface. The resulting secondary vorticity interacts with the original vortex ring in a somewhat inviscid manner, causing substantial divergence from the classical image trajectory.

By replaying flow visualization video tape sequences in slow motion, one can readily observe the effect of the secondary vorticity on both the trajectory of the original ring and the dispersal of its vorticity. The reader should realize that the sequences presented are only a

sample of the many video sequences which were used to draw the conclusions presented here. Each selected sequence contains photographs taken from a particular video sequence, but unfortunately cannot transmit the same degree of physical appreciation as experienced when viewing the original video sequence in slow-motion replay.

3.1.2 Generation of Secondary Vorticity

When a vortex ring approaching a solid surface reaches a height above the surface on the order of the ring radius, it begins to induce a flow between itself and the solid surface. As the vortex continues to approach the surface, a boundary layer flow is formed adjacent to the surface as a result of viscous effects (15).

When the ring approaches very near the surface, a pressure minimum develops directly beneath the center of the core of the vortex ring with the imposed surface pressure increasing radially outward from this minimum. The resultant adverse radial pressure gradient causes the boundary layer flow beneath the ring to separate from the surface along a circular line which is below the vortex core and outboard of the perimeter of the vortex ring. (See Figure 3.1a.) The separated fluid forms an axially symmetric vortex sheet of opposite vorticity, which, if of sufficient strength, will develop into another vortex ring of opposite rotation to the original. (See Figure 3.1b.) To distinguish between these two vortex rings, the original vortex ring shall be referred to as the primary vortex ring (PVR) and the ring generated from the induced boundary layer flow shall be referred to as the secondary vortex ring (SVR). The formation of the SVR from the separated boundary layer has been predicted in a numerical boundary layer analysis by Doligalski (15) and observed experimentally by Boldes and Ferreri (5) and Cerra and Smith (7).

After formation, the primary and secondary vortex rings interact with each other in an apparent Biot-Savart fashion. The secondary vortex orbits from the outside perimeter of the primary vortex over the top of the core and towards the inside perimeter of the primary ring.

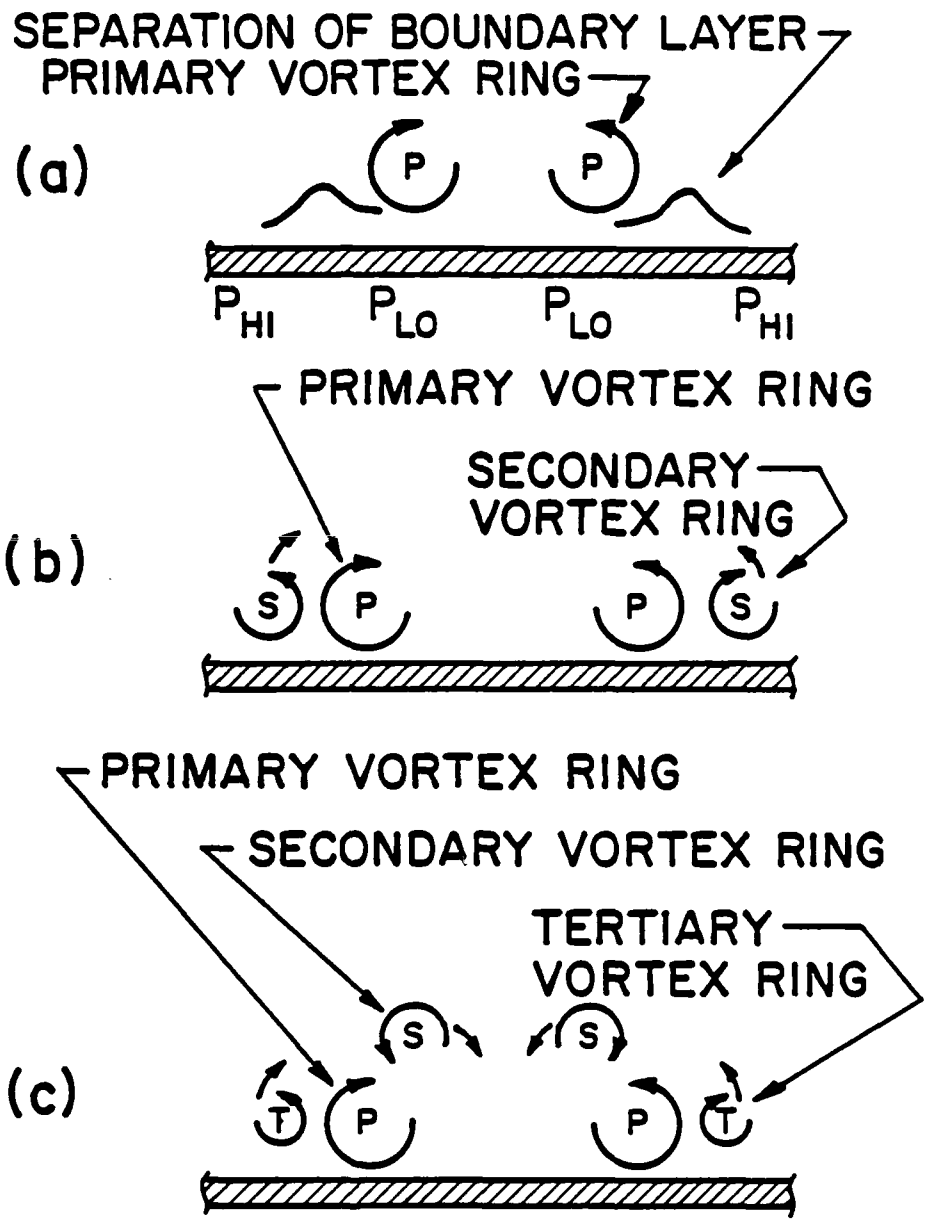

Figure 3.1 Schematic diagram of primary, secondary and tertiary vortex rings. (a) Primary vortex ring approaching solid surface. (b) Generation of secondary vortex ring. (c) Generation of tertiary vortex ring.

If the primary vortex ring has sufficient strength after formation of the secondary vortex ring, another vortex ring of vorticity opposite to that of the primary ring may form due to further boundary layer development beneath the ring. This vortex ring will be referred to as the tertiary vortex ring (TVR). A side view showing the proximity of these three rings is shown schematically in Figure 3.1c.

Figure 3.2 is a sequence of photographs showing the right half of a dyed vortex ring as it impacts a solid surface. Note the finite increase in diameter of the ring. The formation of the secondary vortex can be observed in the latter half of the first row and into the second row of photographs in the sequence. The rotation of the end of the dye spiral in the secondary vortex gives an indication of its vorticity as it orbits above the primary vortex. In the third row one can observe the formation of a relatively weak tertiary vortex ring and the disappearance of the secondary vortex as it orbits into the interior of the primary ring. Although not shown here, the tertiary vortex ring will also behave in a manner similar to the secondary vortex. The interaction of the three vortices does not stop at this point, but rather becomes much more complicated. However, before the complete interaction process with all its complexity is described, a relatively simpler discussion of the trajectories of the vortex rings will be presented. This latter discussion should aid in understanding the details of the total interaction process.

3.1.3 Vortex Ring Trajectories

The vortex ring trajectories presented here were traced onto clear plastic sheets from either the video monitor screen or video-graphic prints, which were obtained from a videographic printer which uses a latent image process with heat developing silver paper and interfaces directly with the video recorder. In both cases, it was necessary to observe the recordings in slow motion to assist in the identification of the centers of the vortex cores from the relative motions of the fluid particles.

Figure 3.2 Close view of right half of vortex ring impacting solid plane surface (side view, dye placed in vortex ring). Vortex ID. #52.218, Re_o=564. Pictures are 0.25 seconds apart.

As stated earlier, inviscid theory predicts a trajectory for which the diameter of the ring increases to an infinite value as the ring asymptotically approaches the surface. Because the theory ignores effects of fluid viscosity, the formation of secondary vorticity nor its subsequent effects will not be predicted.

Although the laws of inviscid dynamics reasonably model the trajectory of a real vortex ring far from a solid surface, they fail when the ring is in the vicinity of the plate. Figure 3.3 is an example of the trajectories of the primary, secondary, and tertiary vortex rings resulting from the interaction of a ring with a low initial Reynolds number (Re_0) based on initial ring diameter, propagation velocity, and kinematic viscosity. Note that the formation of the secondary and tertiary vortices occurs near points in the primary trajectory when the primary vortex is closest to the surface. At these points the adverse radial pressure gradient is greatest, apparently creating discrete boundary layer separations which form the secondary and tertiary vortices.

Figure 3.3 clearly shows the finite limit of the growth in the primary ring diameter and a definite "rebound" of the primary ring away from the surface in two locations. As will be discussed, this rebound phenomenon appears to be caused by an inviscid interaction between the primary vortex ring and the secondary and tertiary vortex rings.

Figure 3.4 shows another set of trajectories for a set of primary, secondary, and tertiary vortex rings obtained for a primary vortex ring with a much higher Reynolds number. This figure indicates that the primary ring not only rebounds, but also experiences a reversal in radial velocity which shrinks the ring diameter. The primary vortex in this case is much stronger, as indicated by the larger Reynolds number, thus the secondary and tertiary vortices are consequently stronger. It was generally observed that vortices with a Re_0 less than 600 only displayed a rebound behavior. For vortices with an Re_0 between 600 and 1300, rebound was always observed,with a reversal behavior

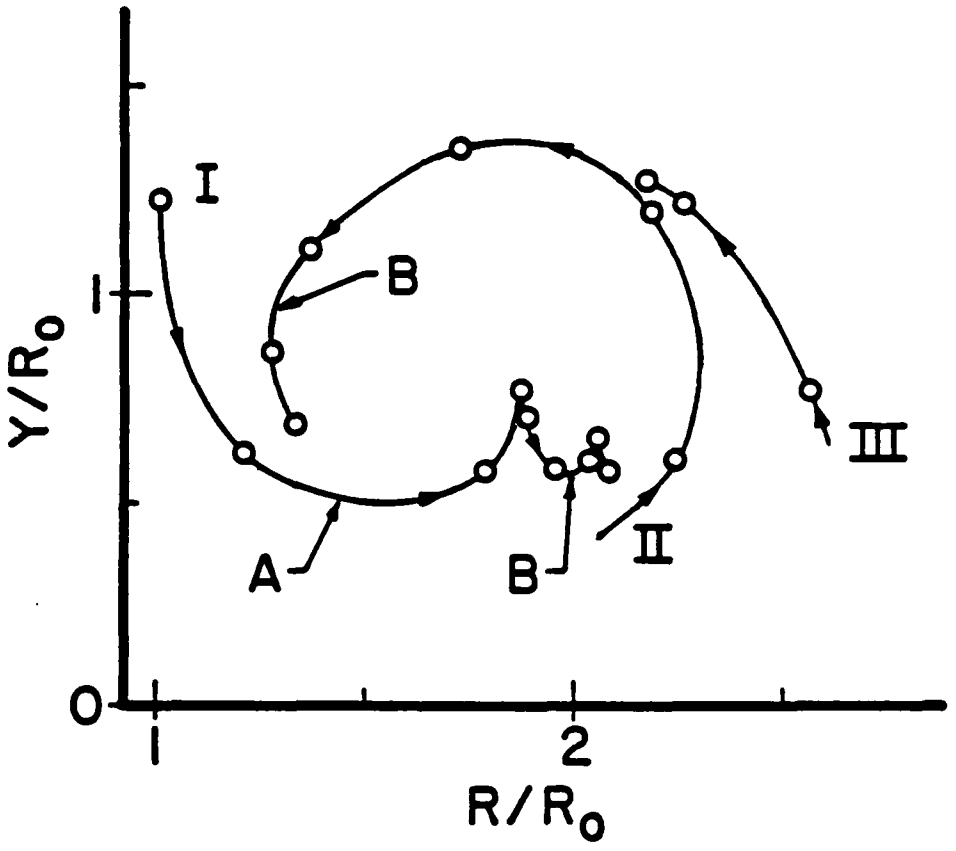

Figure 3.3 Trajectories of the right cores of the primary, secondary, and tertiary vortex rings. Curve I: Trajectory of the primary vortex ring. Curve II; Trajectory of the secondary vortex ring. Point A on curve I coincides in time with the origin of curve II. Point B on curves I and II coincides in time with the origin of curve III. ○ Marks time intervals of 0.5 seconds. Vortex ID.#52.218, Re_0=564. Observe rebound in the trajectory of the primary vortex.

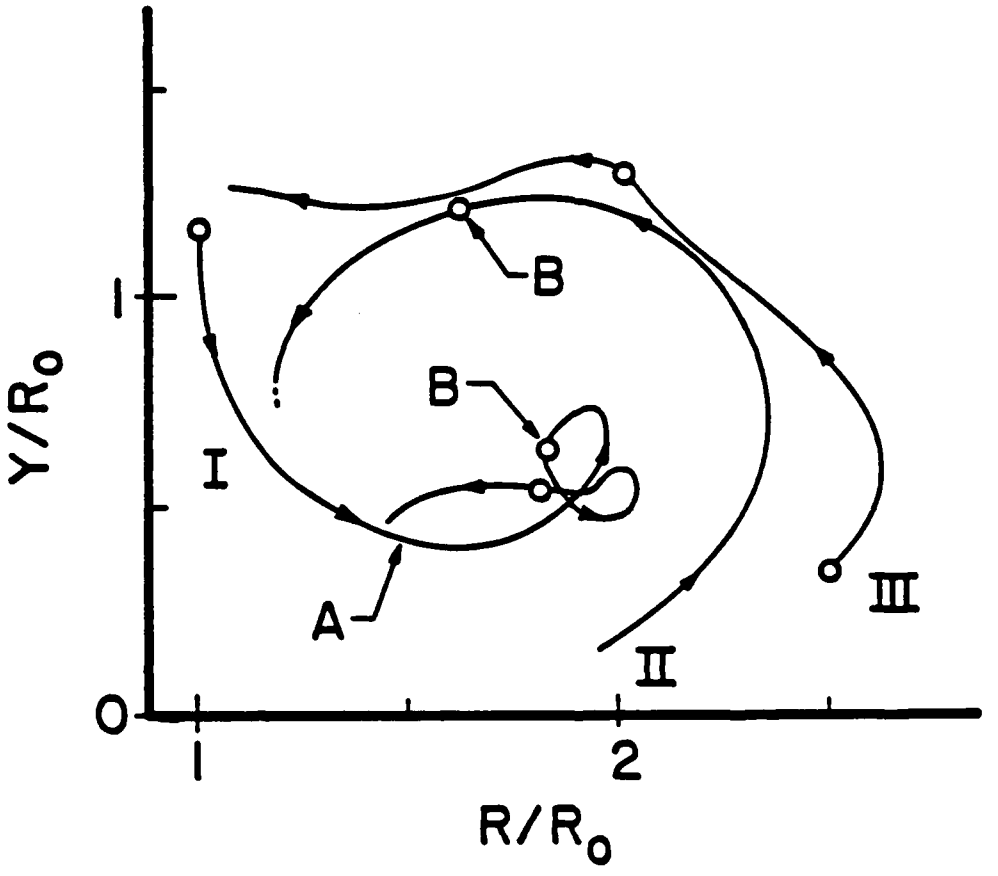

Figure 3.4 Trajectories of the right cores of the primary, secondary, and tertiary vortex rings. Curve I: Trajectory of the primary vortex ring. Curve II; Trajectory of the secondary vortex ring. Curve III: Trajectory of the tertiary vortex ring. Point A on curve I coincides in time with the origin of curve II. Point B on curves I and II coincides in time with the origin of curve III. O Marks time intervals of 0.5 seconds. Vortex ID.#52.250, Re_0=2550. Observe rebound and reversal of primary vortex.

developing as Re_o increased. When Re_o exceeded 1300 both rebound and reversal were always observed.

Figure 3.5 illustrates the trajectories of 4 different primary vortex rings with Re_o ranging from 564 up to 2840. In the first trajectory (Figure 3.4a), only rebound occurs. The PVR is rather weak as is indicated by its Re_o of 564. Each of the next three trajectories (Figures 3.5b-d) are for vortex rings which have a Re_o greater than 1300 such that both rebound and reversal occur. Note that the strength of the reversal, and complexity of the trajectory appears to increase with the initial Reynolds number.

The explanation for rebound, reversal, and other variations observed in the trajectories of primary vortex rings appears to lie in the velocities induced by the presence of the secondary and tertiary vortices. In the vicinity of the solid surface the primary vortex experiences a self-induced axial propagation velocity and a radial velocity due to an image vortex effect created by the surface. However, the formation of a secondary vortex by viscous effects creates a situation such that the primary and secondary vortices will mutually induce a velocity upon each other due to Biot-Savart effects. The velocity which the secondary vortex induces on the primary vortex is responsible for the rebound and reversal observed in the primary vortex trajectory. Likewise the velocity which the primary vortex induces on the secondary vortex causes the secondary vortex to orbit around the primary vortex. As the secondary vortex orbits the primary vortex, the direction of the mutually induced velocities continually changes. As illustrated in Figure 3.6, when this induced velocity due to the secondary vortex is vectorally added to the self and image induced axial and radial velocity components of the primary vortex ring, the result is a primary vortex core velocity which can experience drastic changes in both magnitude and direction, yielding the observed rebound and reversal behavior.

The presence of the tertiary vortex has an effect on the primary vortex very similar to that of the secondary vortex. The tertiary vortex induces a velocity on the primary vortex just as the secondary vortex

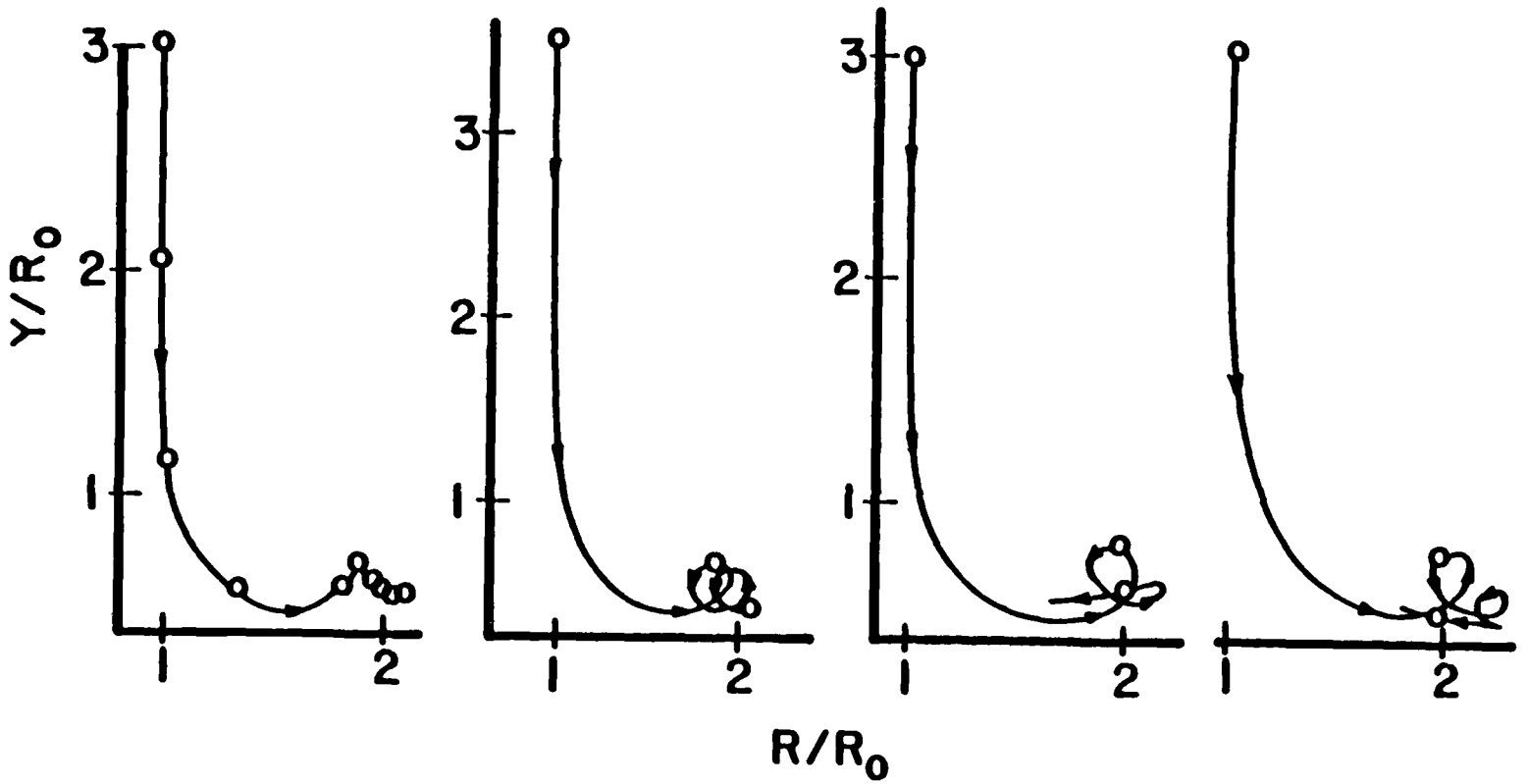

Figure 3.5 Trajectories of the right cores of primary vortex rings. (a) Vortex ID #52.218, Re_o = 564; (b) Vortex ID #51.160, Re_o = 1680; (c) Vortex ID #52.250, Re_o = 2550; (d) Vortex ID #52.265, Re_o = 2840; ○ Marks time intervals of 0.75 seconds.

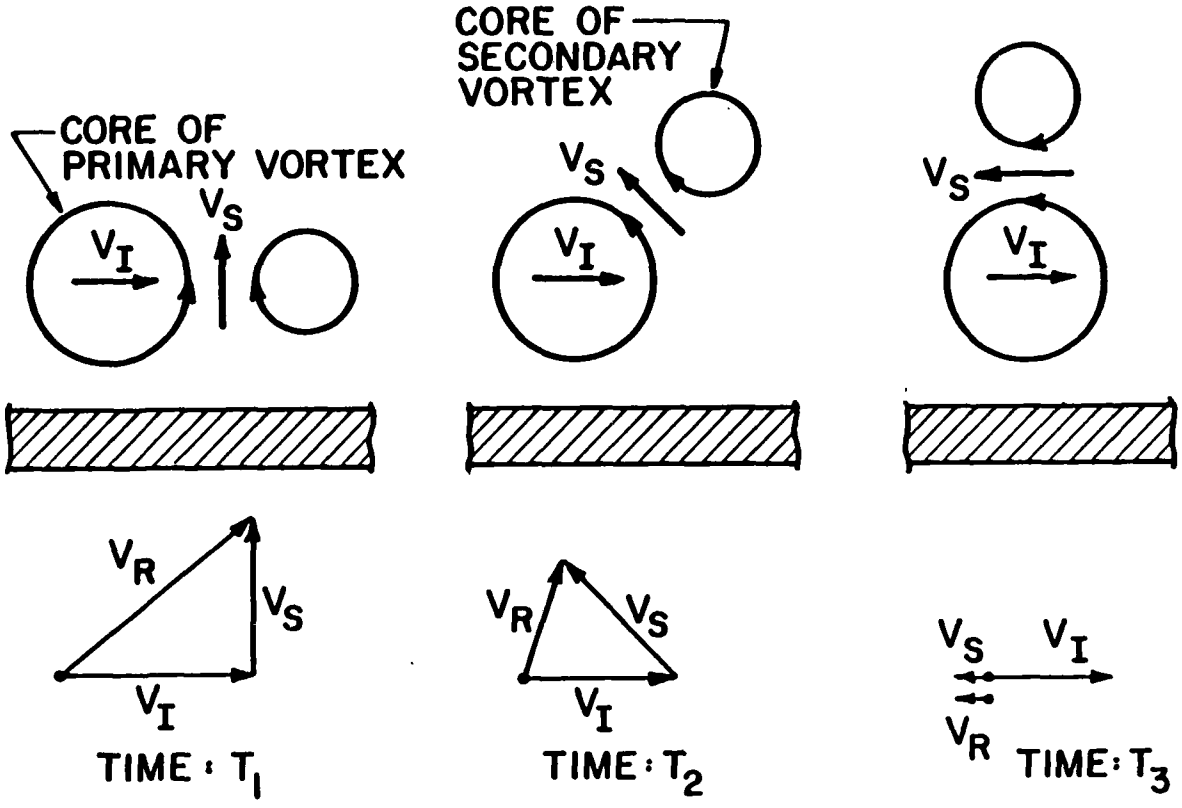

Figure 3.6 Effect of the secondary vortex on the velocity of the primary vortex. V_I: the velocity component of the primary vortex induced by its image vortex. V_S: the velocity component of the primary vortex induced by the secondary vortex. V_R: the velocity of the primary vortex resulting from the addition of V_I and V_S.

does; however, the interaction process becomes much more complicated by the presence of three interacting vortices. Not only do the primary and tertiary vortices mutually induce velocities on each other, but induced velocities are also experienced between the secondary and tertiary vortices as well. In addition to the mutually induced velocities, there are also self-induced propagation velocities acting on each of all three vortices. Figure 3.7 attempts to illustrate the self and mutually induced velocities and the progressive increase in complexity of the interaction process.

The relative strengths of the vortices is an important determinant of the nature of the interaction process. The initial Reynolds number of the fully developed primary vortex ring, which can be used to indicate the strength of the primary and to a much lesser extent that of the secondary and tertiary vortex rings, is given by,

$$Re_o = \frac{DoUo}{\nu} \tag{3-1}$$

where

Do = the initial diameter of the fully developed primary vortex ring

Uo = the initial translational or axial velocity

ν = the kinematic viscosity.

The strength as measured by the circulation Γ of an inviscid vortex ring is given by (64),

$$\Gamma = \frac{4\pi\ RU}{\ln(8R/a)\ -\ C} \tag{3-2}$$

where

a = the core radius of the vortex ring

c = a constant dependent on the vorticity distribution across the core

R = initial vortex ring radius

U = initial propagation velocity of the vortex.

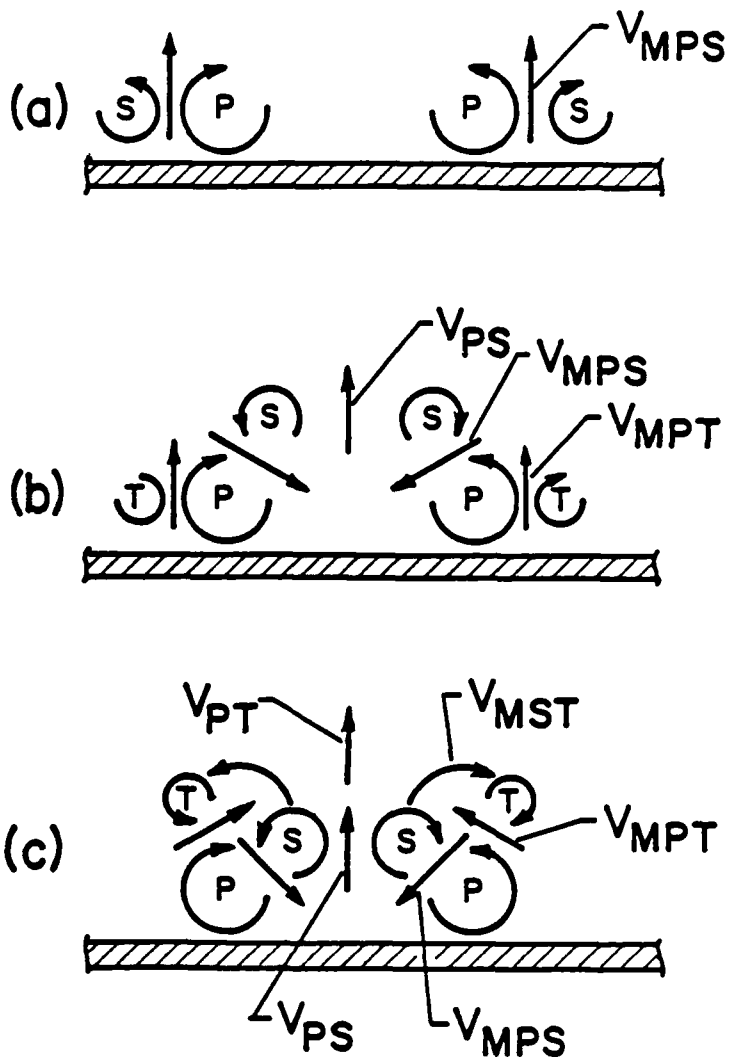

Figure 3.7 Velocities resulting from vortex interactions. (a) Generation of secondary vortex ring. (b) Generation of tertiary vortex ring. (c) Subsequent interaction of primary, secondary, and tertiary vortex rings. V_{MPS}: The velocity which the primary and secondary vortices mutually induce on each other. V_{MPT}: The velocity which the primary and tertiary vortices mutually induce on each other. V_{PS}: The self-induced propagation velocity of the secondary vortex. V_{PT}: The self-induced propagation velocity of the tertiary vortex. V_{MST}: The rotational velocity which the secondary and tertiary vortices mutually induce on each other.

For a constant fluid viscosity, as the Reynolds number increases the circulation will also increase subject to the change in the ratio of ring radius to core radius. The strength of the secondary and primary vortices should also increase as the strength of the primary vortex increases. Visual observation of the vortices seemed to support the hypothesis that the strength of all three vortices increase as the Re_o of the primary ring is increased. Appendix A discusses various attempts to quantitatively determine the strength of the primary vortex. Because the attempts met with limited success, the Reynolds number, Re_o, based on initial ring geometry and propagation characteristics was used to indicate the strength of the vortices examined in this study.

Figure 3.5 will now be reexamined to illustrate how the strength of the interacting vortices, as indicated by the Reynolds number, can influence the trajectory of the primary vortex ring (PVR). As was discussed earlier, for Re_o less than 600 only rebound was observed in the trajectory of the primary vortex, which is illustrated in Figure 3.5a. Here the velocity induced by the SVR causes a relatively weak PVR to momentarily rebound away from the surface, after which the PVR's self and image induced velocities cause the PVR to continue to increase in diameter and reapproach the surface. The next three vortices have Reynolds numbers of 1680, 2550, and 2840, all of which are above the 1300 Re_o level for which both rebound and reversal are observed. For reversal to occur, the secondary and usually the tertiary vortex rings must be sufficiently strong to cause at least a momentary inversion of the primary vortex ring's radial velocity. In Figure 3.5b, the first reversal in the trajectory, caused by the SVR, is only momentary and creates a loop in the trajectory. The second reversal, caused by the TVR, is also momentary, resulting in a second loop in the trajectory following which the PVR continues to increase in diameter, influenced predominantly by its image velocity at this point. In the next two Figures, 3.5c and d, the trajectories end in a state of permanent reversal. The vortices here are much stronger as indicated by their Reynolds

numbers of 2550 and 2840. The TVR apparently has sufficient strength to cause a permanent reversal in the trajectory of the PVR; the PVR moves back toward its center axis and ceases its radial expansion. The reader should note one difference between these two trajectories. In Figure 3.5d, the PVR is able to close the loop formed during its second reversal before it permanently reverses. This is due to the influence of its induced image vortex velocity and the complicated interaction which is taking place between all three vortices. This complicated interaction will be discussed more fully in a later section of this chapter.

The dynamics of the rebound and reversal process can be summarized as follows. As a primary vortex ring of Re_0 greater than 1300 approaches the wall, its radial velocity and diameter increase because of the image vortex effect caused by the wall. At some point when the primary vortex is very close to the wall, the boundary layer flow induced by the vortex separates due to the adverse radial pressure gradient. This separated boundary layer flow rolls up into a secondary vortex ring of opposite sign to the primary ring. A process of mutual interaction between the secondary and primary vortex rings then ensues. This process causes the secondary vortex to orbit toward the center of the primary vortex ring which is influenced by the velocity induced by the orbiting secondary vortex. At some later point, as the secondary vortex ring orbits around the primary vortex ring, the velocity induced by the secondary ring becomes of sufficient strength and direction to overcome the radial velocity due to the image vortex effect, which results in the reversal of the primary vortex ring. As the secondary vortex continues to orbit the primary vortex, the direction of the induced velocity continues to change until the velocity due to the image vortex effect again becomes radially dominant, causing the primary ring to again grow in the radial direction. As the primary ring approaches the wall again (due to both self induction and the induced secondary vortex velocity), the boundary layer flow again separates and rolls up into a tertiary vortex ring. Throughout this process the strength of the

primary vortex ring is continually decreased as energy is transferred to the secondary and tertiary rings or is dispersed into surrounding fluid. Thus, as the primary vortex weakens the velocity due to the image vortex effects is likewise decreased. The tertiary vortex also orbits above the primary ring and induces a velocity on it. The velocity inversion of the primary vortex caused by the tertiary vortex may be either momentary or permanent as shown in Figure 3.5, depending on the relative strengths and positions of the three vortex rings and their degree of interaction.

The preceding discussion of the trajectory of the PVR has been done at a global level, with the evaluation of the interaction of the PVR with the SVR and TVR and the subsequent effects on the PVR trajectory performed in a two-dimensional sense; it was not necessary to consider any three-dimensionality in the interaction process. However, to properly discuss the mechanisms responsible for dispersal of the initial vorticity of the PVR, the interaction process must be examined on a local level. In the following discussions of the dispersal of vorticity, the three-dimensionality of the interaction process will be illustrated and discussed in detail.

3.1.4 Dispersal of Vorticity

Perhaps the most important effect of the secondary vortex is to precipitate the breakdown of the structure of the PVR, resulting in the rapid dispersal of vorticity of the primary vortex. Some investigators (81) have observed that the organized flow of a vortex ring upon impact with a solid surface develops very rapidly into a "cloud" of turbulent fluid. Figure 3.8 shows the development of the primary ring into such a turbulent mass of fluid at two points in time. Figure 3.8a shows the side and plan views of vortices at a point where the tertiary vortex ring is in the process of formation. One can observe that the primary vortex ring is still rather coherent and radially symmetric. On the other hand, figure 3.8b shows the "turbulent", apparently chaotic mass of fluid following the dispersal of the vorticity

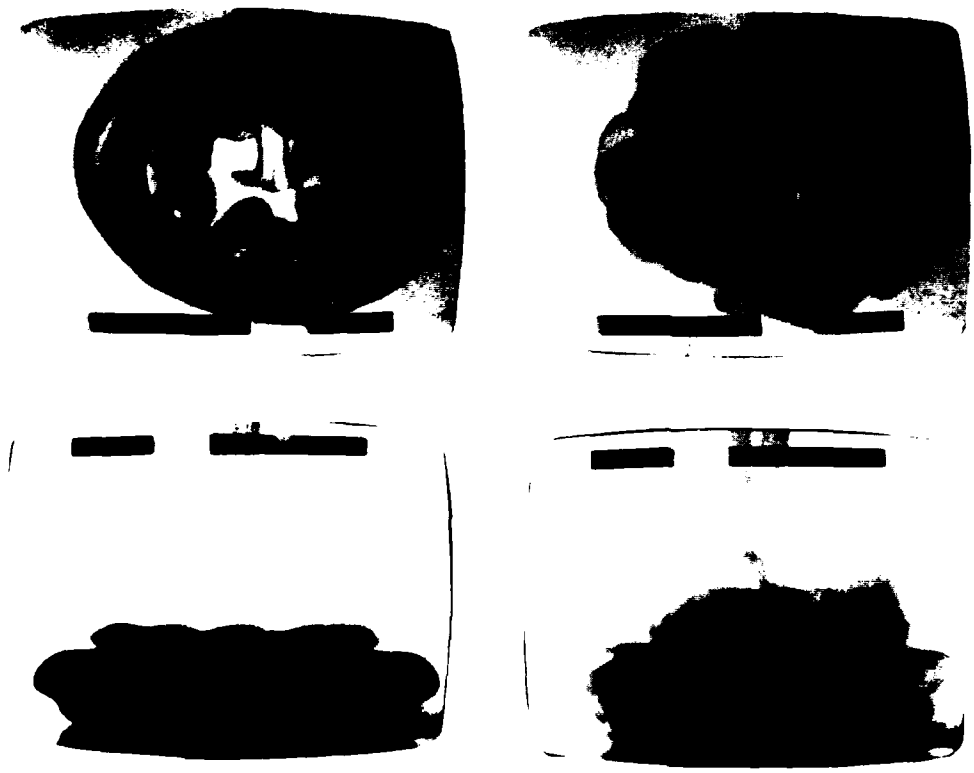

Figure 3.8 Breakdown of primary vortex (side and oblique plan views, dye placed in vortex). (a) Before breakdown, (b) after breakdown. Side views: Vortex ID #41.830, Re_o=1250. Plan view: Vortex ID. #51.145, Re_o=1000.

of the primary vortex by the subsequent interaction of the primary ring with its secondary and tertiary rings. The following figures and discussion will attempt to illustrate the very organized nature of the interaction which results in this dispersal of ring vorticity.

3.1.4a Laminar Diffusion

The simplest mechanism by which the vorticity of the primary vortex ring can be dispersed is laminar diffusion. For Reynolds numbers below 350, laminar diffusion of vorticity was the only mechanism observed; no secondary or tertiary vortices were observed to form. Figure 3.9 is a sequence of side and plan-views illustrating a diffusion dominated vortex ring impact with a solid surface. The vorticity of the ring very slowly diffuses, as evidenced by the five second time span of the sequence, while the vortex ring never loses its coherent, azimuthally symmetric shape. When viewing these photographs, it is important to realize that the dye visualization can be somewhat misleading because the dye diffuses more slowly than the vorticity into the surrounding fluid (51). In this sequence, the vortex is sufficiently weak such that laminar diffusion suffices to cause dispersion of the vorticity without the generation of the secondary and tertiary vortices which, as will be shown for stronger initial vortices, accelerate the dispersion of vorticity by convection effects.

3.1.4b Primary-Secondary Vortex Interaction

Vortices with Reynolds numbers greater than approximately 350 generate secondary vorticity at the solid surface which, as previously explained, rolls up into secondary and tertiary vortex rings with vorticity of opposite sign to that of the primary vortex ring. During this process the vorticity of the primary ring is rapidly dispersed into previously irrotational fluid through the discrete generation of these secondary and tertiary vortex rings. The primary, secondary, and tertiary vortex rings then interact in a very organized manner to further disperse the vorticity of the primary vortex into the surrounding

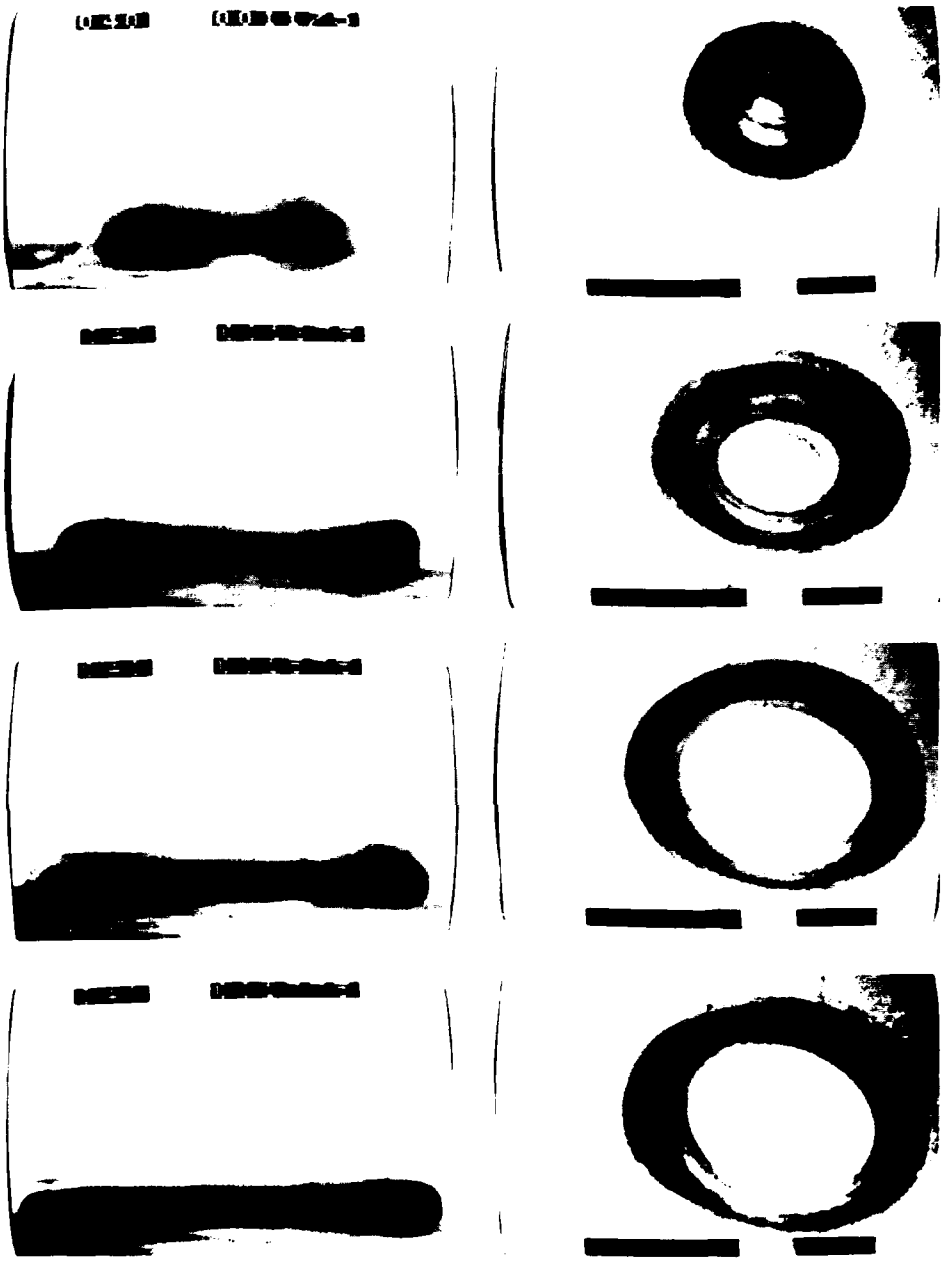

(a) (b)

Figure 3.9 Vortex ring impacting solid plane surface ((a) side and (b) oblique plan views, dye placed in vortex ring). Vortex ID #50.625, Re_0=126. Pictures are 1.67 seconds apart.

fluid. The eventual disintegration of these organized vortex flows results from a very complex three-dimensional viscid-inviscid interaction process during which the scales of fluid motion continually decrease.

The primary vortex ring is initially axially symmetric when it impacts the solid surface, as is the initial secondary vortex ring generated from the vortex sheet created during this impact. Following its formation, the secondary vortex ring orbits from the outside perimeter of the primary vortex ring around the top of the core towards the inside perimeter of the primary ring. As it orbits, the diameter of the secondary ring is compressed. This compression causes the ring to become unstable (76) which leads to the development of an azimuthal waviness in the secondary vortex ring. Figure 3.10 is a sequence of photographs illustrating the interaction process, beginning with the impact of the primary vortex ring and continuing through the development of the azimuthal waviness in the secondary vortex. In the last two frames the formation of the tertiary vortex ring can be observed. Figure 3.11 is a sequence for a primary vortex ring generated in an identical manner to that shown in Figure 3.10 with the interaction visualized by placing a sheet of dye adjacent to the solid surface, rather than in the fluid from which the primary ring was generated, as was done for Figure 3.10. Placing dye on the surface allows one to visualize the behavior of the fluid originally adjacent to the surface. From Figures 3.10 and 3.11 one can clearly see that the secondary vortex ring is comprised of fluid not only from the primary vortex, but also from originally quiescent fluid at the surface of the plate.

The development of azimuthal waviness is shown in an oblique plan view in Figure 3.12. Note that during the initial phases of the interaction process the primary vortex ring does not develop the azimuthal waviness characteristic of the secondary vortex. Although the original vorticity of the primary vortex has been dispersed throughout a larger volume of fluid by the formation of the secondary vortex ring, the primary vortex ring is still very coherent and has not yet begun to

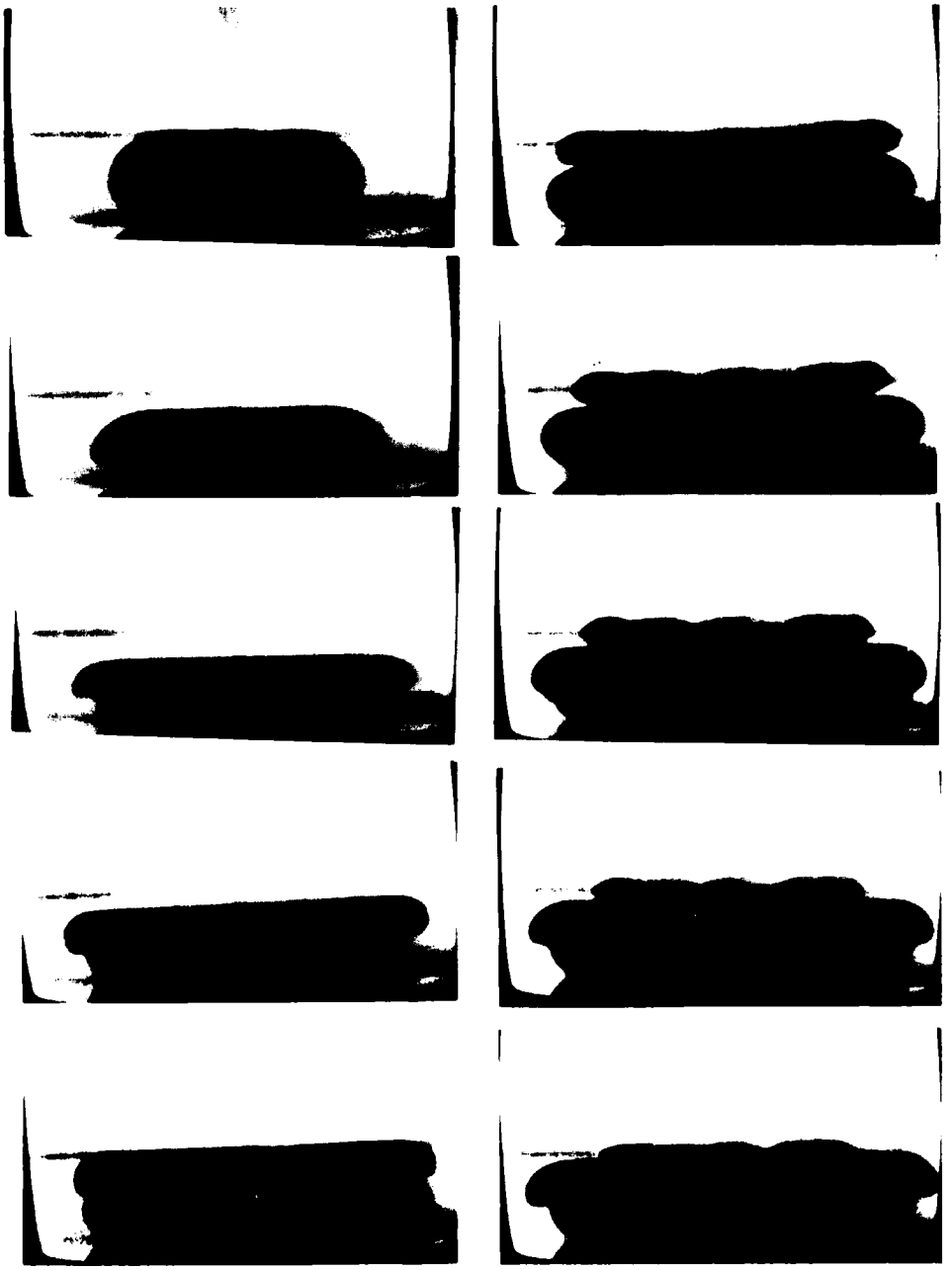

Figure 3.10 Vortex ring impacting solid plane surface (side view). Illustrates development of azimuthal waviness in secondary vortex, visualized by placing dye in vortex ring. Vortex ID.=41.830, Re_0=1250. Pictures are 0.083 seconds apart.

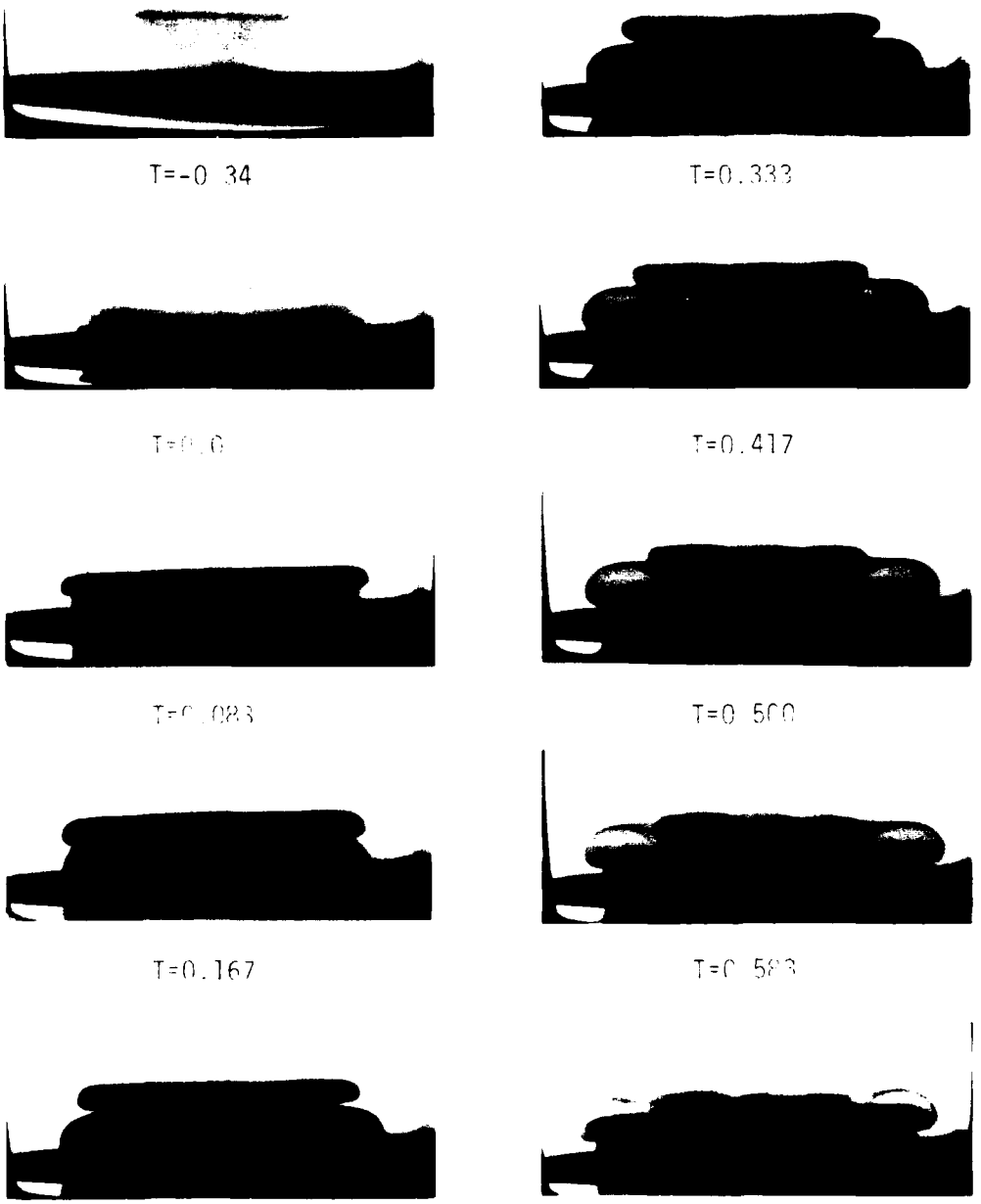

Figure 3.11 Vortex ring impacting solid plane surface (side view). Illustrates development of azimuthal waviness in secondary vortex, visualized by placing dye on the surface. Vortex ID. #41.830, Re_0=1250. Picture time units are seconds.

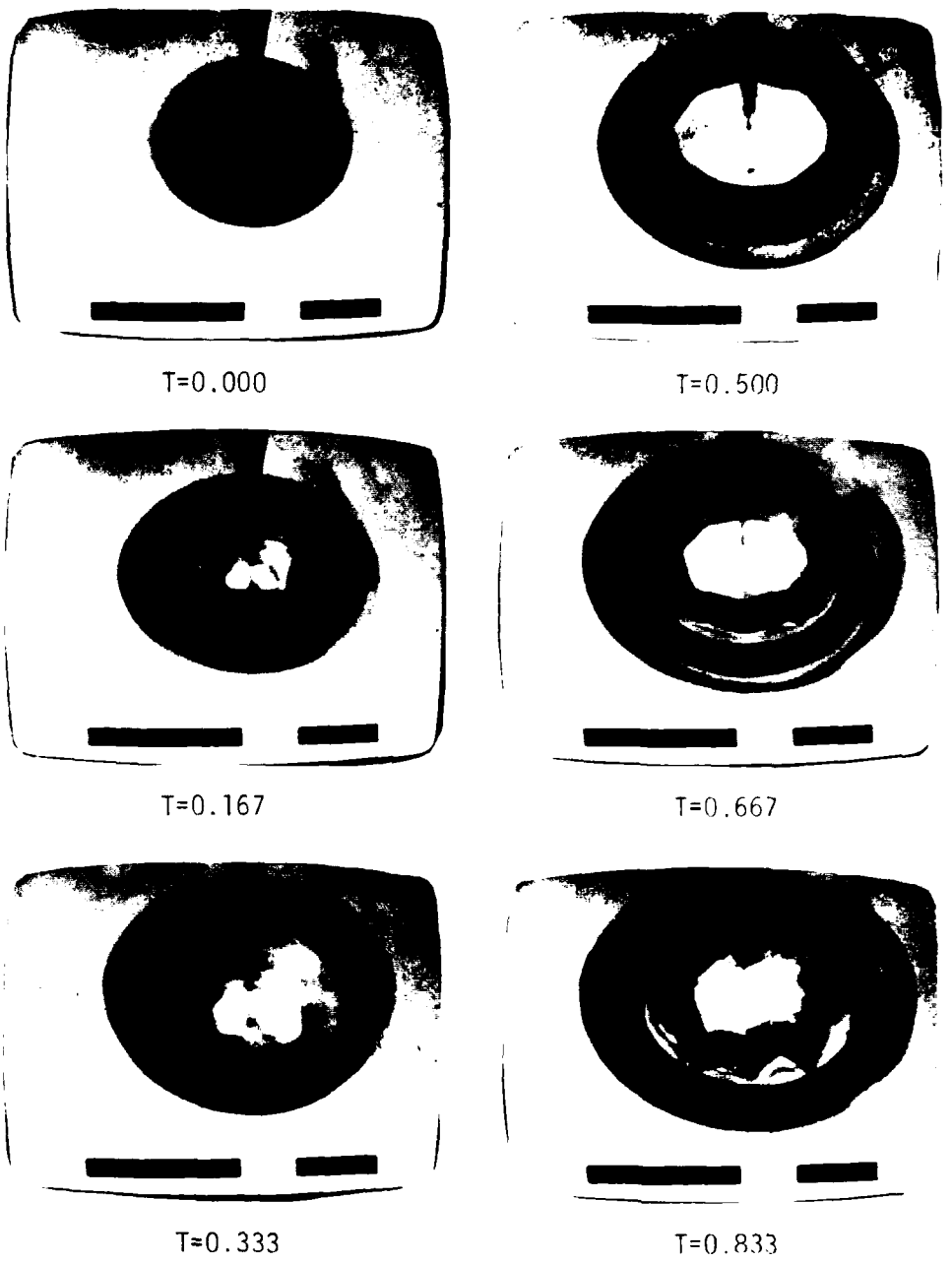

Figure 3.12 Vortex ring impacting solid plane surface (oblique plan view, dye placed in vortex). Illustrates development of azimuthal waviness in secondary vortex. Vortex ID.=41.830, Re_o=1250. Picture time units are seconds.

degenerate to the chaotic mass of fluid we commonly associate with turbulence.

The azimuthal waviness which develops in the secondary vortex ring is speculated to arise from either an instability present in the primary vortex or more probably from an instability caused by the compression of the secondary vortex ring. It has been observed by Widnall (100) that a vortex ring propagating through a quiescent fluid may develop an instability which leads to an azimuthal waviness in the ring. The development of this Widnall instability has been shown to be primarily a function of distance travelled. The present experiments were configured such that the fully developed vortex rings remained stable prior to impact with the surface. Of the many different types of vortices generated, a few became unstable before impact, displaying the development of an azimuthal waviness in the primary vortex ring. In just about all of these cases, the secondary vortex ring which formed at the surface displayed an immediate azimuthal waviness which appeared to be induced by the waviness in the primary vortex.

However, the vast majority of the vortices examined in this study appeared to be stable and azimuthally symmetric before impact. As can be observed in Figures 3.10 and 3.12, these initially stable primary vortex rings display no azimuthal distortion even after the secondary vortex has developed an extreme azimuthal waviness. Since all observations of stable vortex impacts displayed the same universal pattern (i.e. wavy secondary vortex ring, but non-wavy primary vortex ring) it is felt that the instability giving rise to the azimuthal waviness in the SVR probably develops due to the vortex compression effects and is not a result of an initial instability present in the PVR.

The azimuthal waviness of the secondary vortex ring will eventually create a waviness of the primary vortex ring structure through a complex viscid-inviscid interaction. The subsequent result of this interaction is a three-dimensional breakdown of the original flow field. The waviness of the secondary vortex ring will cause some sections of the secondary vortex to migrate closer to the primary vortex than other sections.

Variations in the proximity of the two vortices causes variations in the mutually induced velocities of these two rings. The variations in the velocities results in three-dimensional stretching of the vortices and relocations of fluid, which through viscous action disperses the vorticity of the rings into a larger volume of fluid and in many different directions. As the vortices are progressively stretched and entangled, the scales of motion continually decrease until an apparently chaotic "turbulent" state results.

3.1.5 Development of Secondary Vortex Ring Structure

After a secondary vortex ring develops an azimuthal waviness, it is observed to develop either a looped or a kinked structure; the difference in these structures is the extent to which the azimuthal perturbations of the loop are deformed or stretched. The loop-structured secondary vortex has a wavy structure which becomes highly deformed or stretched, while the kink-structured secondary vortex displays a waviness which is of smaller amplitude, often just barely detectable. These two variations in vortex structures and development will be discussed and illustrated in more detail in the following sections.

As the Reynolds number of the PVR is increased, the structure of the SVR gradually evolves from a loop to a kink structure. When the SVR structure is in the transition region between these two structures, one section of the SVR will often display the characteristics of the looped structure while the remainder of the SVR displays a kinked structure. As the Reynolds number is increased beyond the transition region, the section of the SVR displaying a looped structure will decrease until the entire SVR displays a kinked structure. As was mentioned previously, below an Re_o of 350 no secondary vortex formation is observed. Loop-structured secondary vortices were generally observed for vortices within a Reynolds number range of 470 to 1600. Between 1600 and 2500 the structure appeared to be in transition between a looped and a kinked structure. Kink-structured secondary vortices were observed for a

Reynolds number range from 2500 to 3000. Above an Re_o of 3000, the present apparatus could not generate primary vortices which would remain stable prior to impact.

3.1.5a Loop-Structured Secondary Vortex Ring

The loop-structured secondary vortex ring develops from a ring with azimuthal waviness of relatively small amplitude into a three-dimensional vortex loop with azimuthally symmetric loops of large amplitude. A schematic diagram of such a loop structure is sketched in Figure 3.13. Each loop has one end which migrates very close to and orbits around the core of the primary ring while the other end of each loop migrates toward the center axis and away from the plane of the primary ring. The ends of the loops closer to the primary ring interact most strongly; their proximity to the ring results in much greater induced velocities causing the ends to orbit in a tighter arc about the core of the primary vortex. As shown in Figure 3.13b, if the strength of the primary vortex ring is sufficient, the lower ends of the loops will pass beneath and around the core of the primary ring. This behavior has been observed (using dye placed on the plate) for the majority of the secondary vortices displaying loop behavior. Those for which loops do not rotate under the PVR still seem to be deformed or stretched by the PVR in such a way that a layer of dye is pulled away from the secondary vortex and under the PVR. The cause of this variation is uncertain; further study and analysis would be required to resolve this variation in behavior.

Because they migrate farther from the PVR, the upper ends of loops in the secondary vortex ring do not interact with the PVR as strongly as the lower ends. As they orbit over the top of the core of the PVR, they stay above the plane of the PVR and propagate toward the center of the ring. Since the upper loops are farther from the PVR, the mutually induced velocities are less than those induced between the PVR and the lower ends of the loops. The vorticity of the upper loops is such

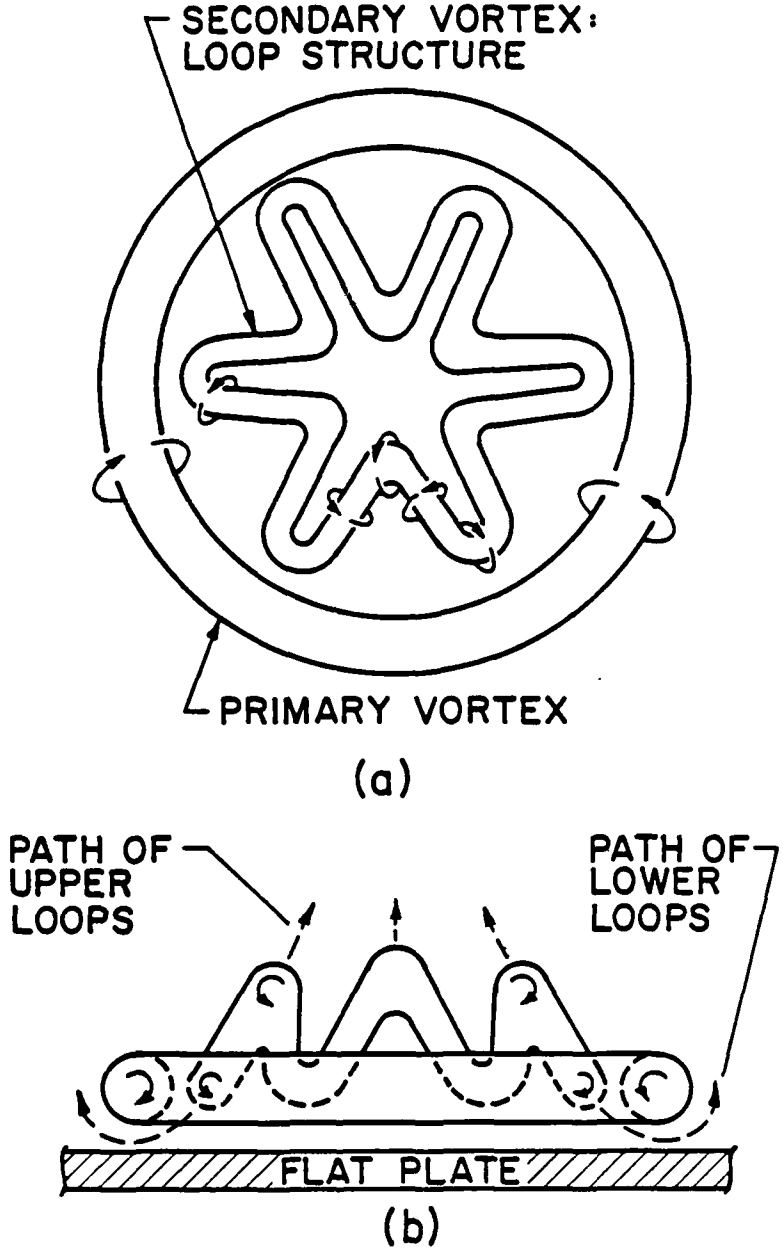

Figure 3.13 (a) Diagrammatic plan view and (b) diagrammatic side view of loop structured secondary vortex.

that their proximity to each other causes a self-induced propagation velocity in the vertical direction away from the PVR. Thus in most observations of loop-structured secondary vortices, the upper ends of the loops move toward the center axis of the PVR and upward away from the surface. Generally as the Re_o of the PVR increases, the strength of the SVR increases and the upper ends of loops move vertically upward with a greater self-induced velocity.

Figures 3.14 and 3.15 show the development of a loop-structured secondary vortex in side view; Figure 3.14 was visualized by placing dye in the PVR and Figure 3.15 was visualized by placing dye on the surface of the plate. One can observe the evolution of the SVR from a ring with azimuthal waviness to a structure consisting of highly deformed loops. Although the loops do not appear to be pulled beneath the core of the PVR, one can observe at the arrow in the last photograph of Figure 3.14 the aforementioned behavior in which a dye layer from the SVR is pulled beneath the core of the PVR. Figure 3.15 reveals how the upper ends of the loops slowly propagate toward the center axis of the PVR. Because this is a relatively weak PVR (Re_o = 440), the upper ends of the loops do not propagate as far toward the center nor as far vertically as was observed in other cases of loop-structured secondary vortex rings.

Figure 3.16 is an oblique plan-view, obtained with a sheet of dye on the surface, illustrating the development of a loop-structured secondary vortex for which the lower loops pass beneath the PVR. The first row of photographs in this figure clearly shows the development of the periodic loops from the aximuthal waviness of the secondary vortex. The edge of the clear region is essentially the location of the outer perimeter of the PVR. The last photograph in the first row and the photographs comprising the second row show the formation of the tertiary ring, the very dark ring of dye that appears at the beginning of the second row. At this same point in time, the lower loops of the secondary vortex can be observed to pass beneath the PVR with a consequential stretching taking place. As they stretch, the core diameters

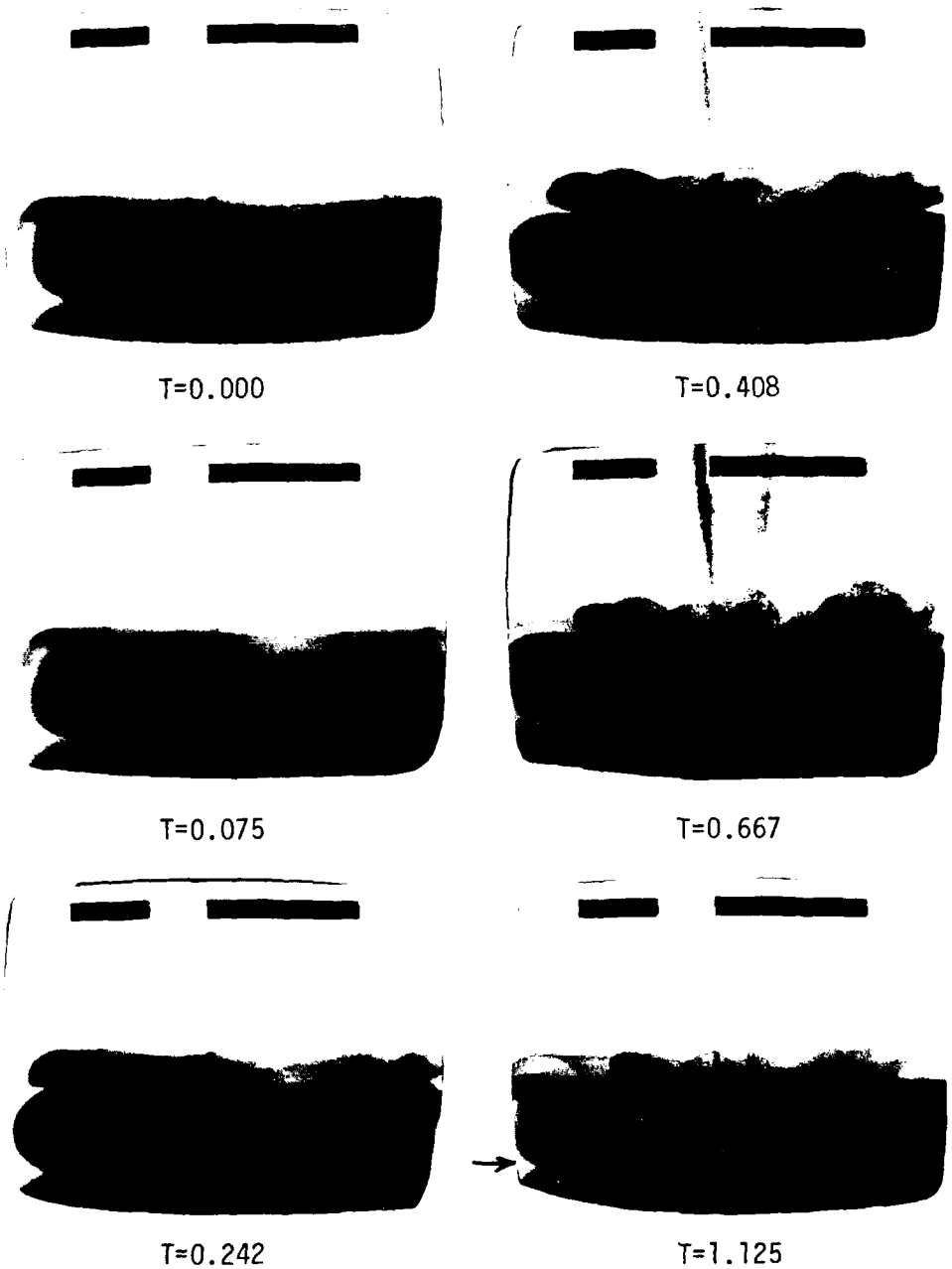

Figure 3.14 Development of loop structured secondary vortex, visualized by placing dye in the vortex (side view). Right edge of primary vortex is not in view. Vortex ID.#40.860, Re_o=440. Picture time units are seconds.

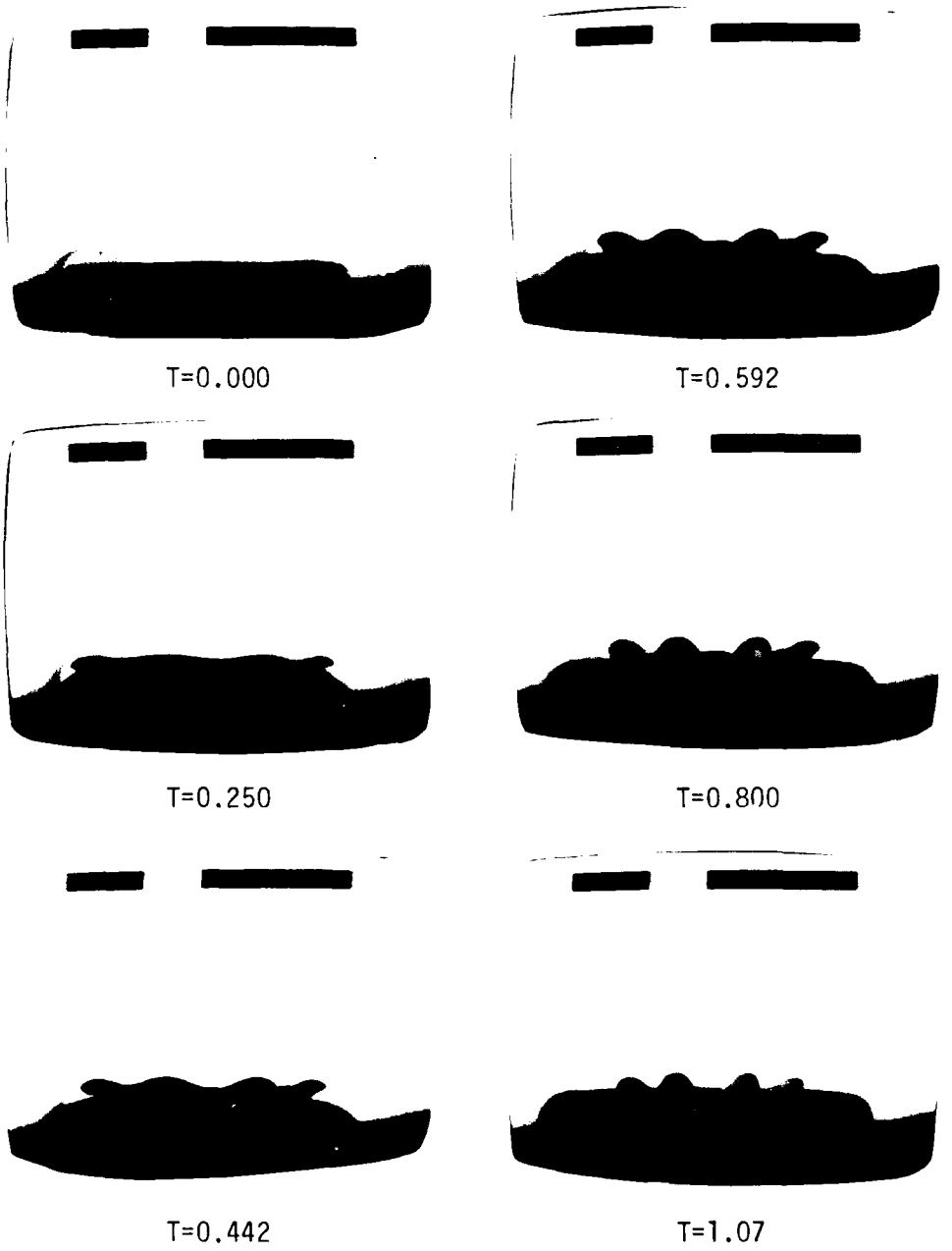

Figure 3.15 Development of loop structured secondary vortex, visualized by placing dye on surface (side view). Vortex ID. #40.860, Re_o=440. Picture time units are seconds.

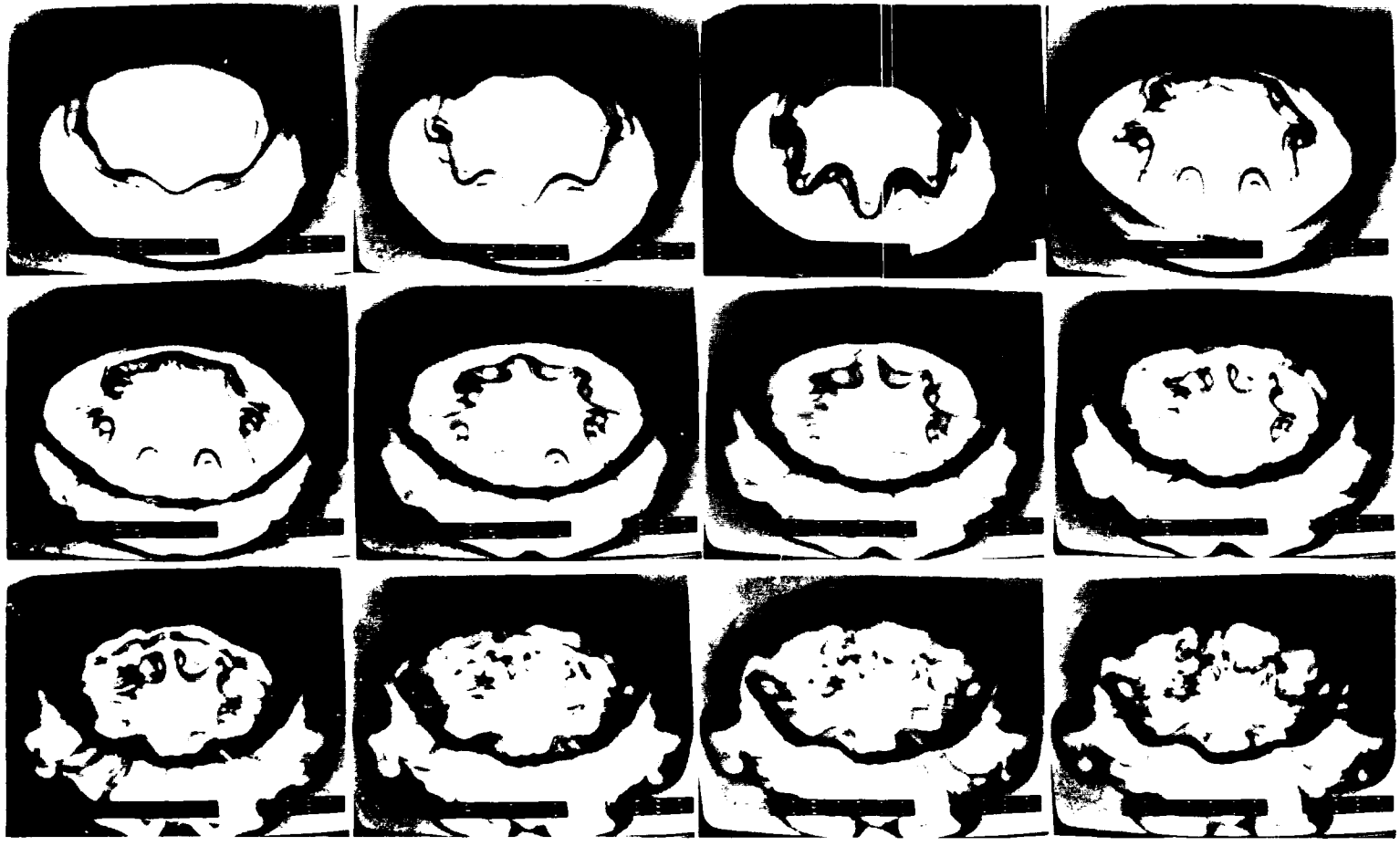

Figure 3.16 Development of loop structured secondary vortex (oblique plan view, dye placed on surface). Vortex ID.#51.130, Re_0=811. Pictures are 0.167 seconds apart.

of these loops decrease and presumably their vorticity increases. As the ends of the loops are pulled under the core of the PVR, the sides of each loop trail behind somewhat parallel to each other, forming pairs of counter-rotating vortices. These counter-rotating vortex pairs wrap around the core of the primary ring very quickly. Starting with the sixth photograph in the sequence, the formation of "mushroom" shapes caused by these counter-rotating "legs" of the loops can be clearly observed in the lower section of each photograph. With the appearance of these mushroom shapes, both the primary vortex (observed in other sequences with dye in the vortex) and the tertiary vortex begin to deform three-dimensionally.

Once a three-dimensionality is imposed on the structure of the vortex ring, all subsequent motion, stretching, and entanglement of the vortices acts to increase the three-dimensionality. As the three-dimensionality increases, the scales of the motion decrease and the structure of the vortices becomes increasingly complex. The symmetry of this process continually degenerates due to an amplification of initial irregularities, until what some researchers describe as a turbulent state results. In actuality what has happened is that the vorticity of the original vortex is dispersed through a larger volume of fluid in many different directions, but by a very organized and structured process.

3.1.5b Kink-Structured Secondary Vortex and Ejection Process

Although both loop-structured and kink-structured secondary vortices cause the PVR to breakdown three-dimensionally and disperse its vorticity, there are significant differences as well as similarities in how each accomplishes this. Vortex loops or filaments which wrap around the core of the primary vortex ring are responsible in each case for the breakdown of the primary ring. As shown above, the loop-structured secondary vortex is substantially deformed into periodic loops which wrap around the PVR core. On the other hand, the kink-structured secondary vortex ring deforms very little, but apparently induces other vortex

filaments which wrap around the PVR core and lead to its three-dimensional breakdown.

A second significant difference between these two types of secondary vortex rings is the final trajectory of each after it has orbited above the PVR into the center of the ring. The loop-structured secondary vortex forms loops, of which some ends are wrapped around the primary core and the other ends migrate to the center axis. The kink-structured secondary vortex undergoes a process which will be called secondary vortex ejection, because the entire secondary vortex (which remains in the shape of a ring) migrates vertically away from the PVR and the solid surface. This ejection process takes place with varying degrees of secondary vortex coherence over the Re_o range reported. Although other researchers, notably MaGarvey and LacLatchy (49), have observed the loop-structured secondary vortex (although they did not identify it as such), to the author's knowledge, no one has reported observing the secondary vortex ejection phenomenon associated with the kink-structured secondary vortex.

Figures 3.17a and 3.17b are a sequence of side-view photographs obtained using dye on the surface which show the formation of the kink-structured secondary vortex ring and the subsequent ejection of that ring away from the surface. The kink-structured secondary vortex ring initially forms in the same manner as the loop-structured secondary vortex. As shown by the plan view of Figure 3.18, the SVR orbits around and into the center of the primary ring, developing a weak azimuthal waviness in the process. However, upon reaching the center of the PVR, the waviness does not develop any further, with the SVR residing in the center of the primary ring for some time. The behavior is apparently a result of a balance between 1) the velocity induced on the SVR by the PVR and 2) the self-induced velocity of the SVR (see Figure 3.7). The result is an extended pause of the SVR inside the PVR. The SVR remains in the center of the PVR until the tertiary vortex ring develops and orbits to a position above the primary ring. At this point, the velocity induced by the tertiary ring on the SVR is in the same direction

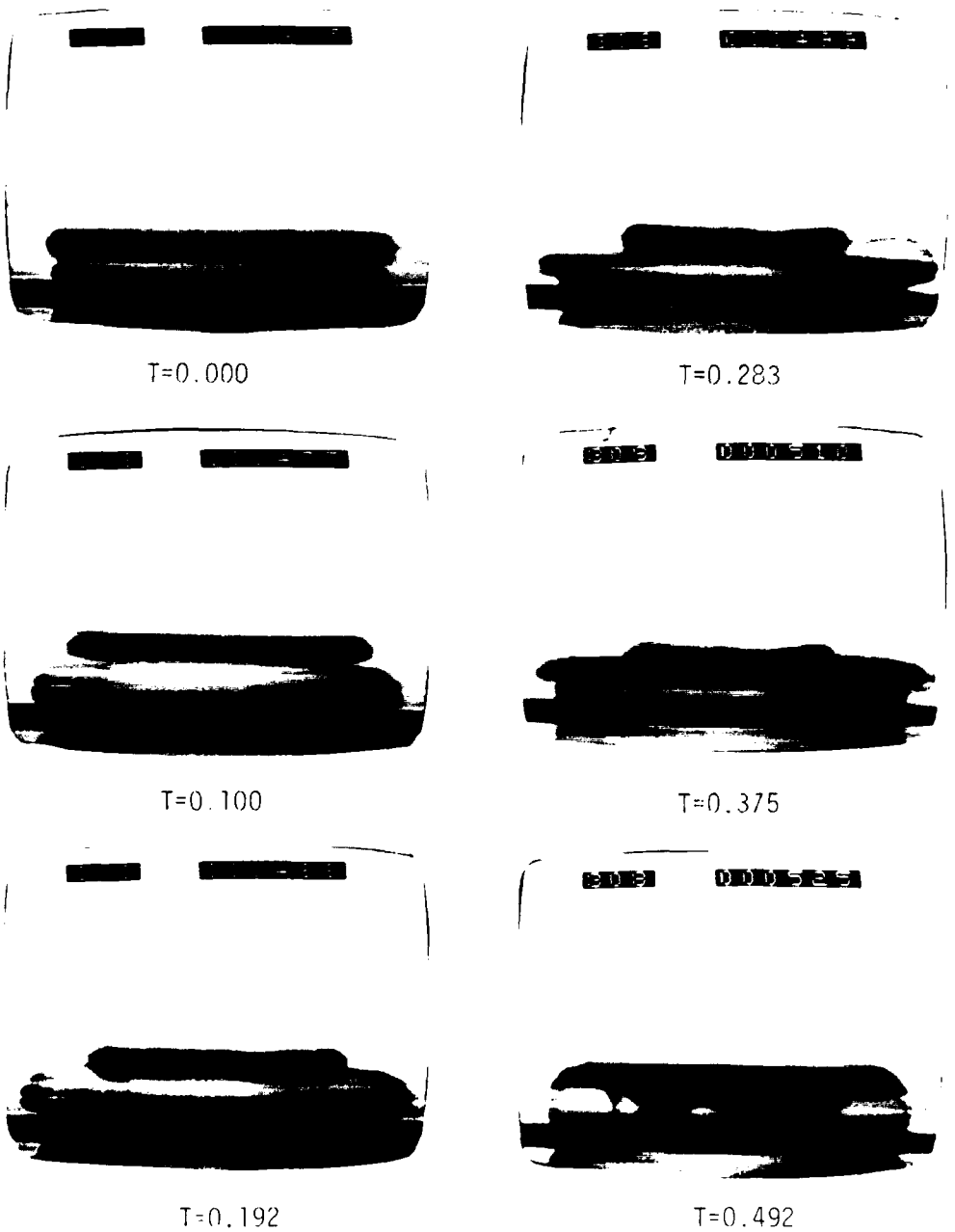

Figure 3.17a Development of kink structured secondary vortex with secondary vortex ejection (side-view, dye placed on surface). Vortex ID. #52.265, Re_o=3000. Sequence continued on next page.

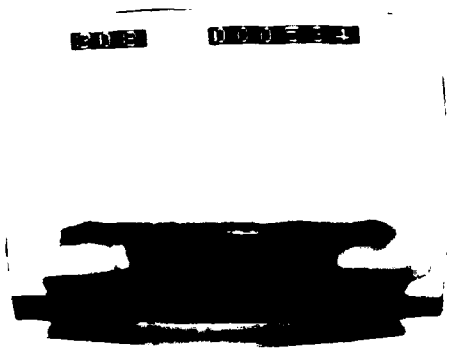

T=0.575

T=0.933

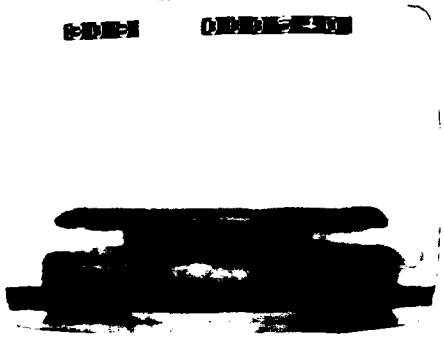

T=0.625

T=1.07

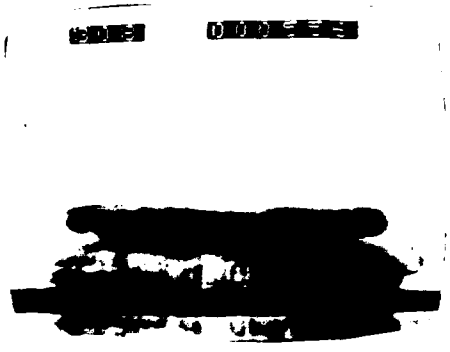

T=0.758

T=1.46

Figure 3.17b (continued)

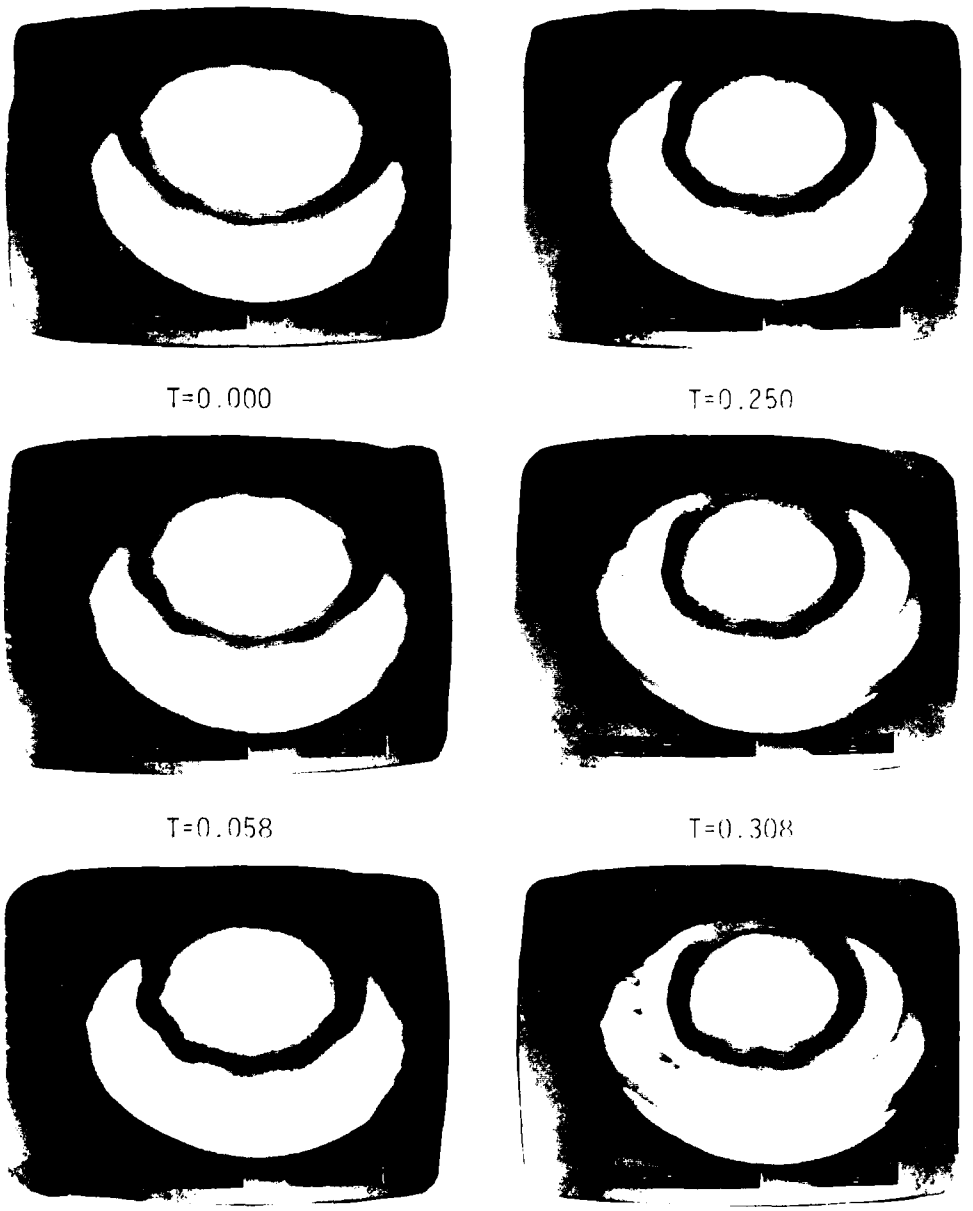

Figure 3.18a Development of kink structured secondary vortex with secondary vortex ejection . Visualized by placing dye on the surface (oblique plan view). Vortex ID #52.250, Re_0=2550. Sequence is continued on next page.

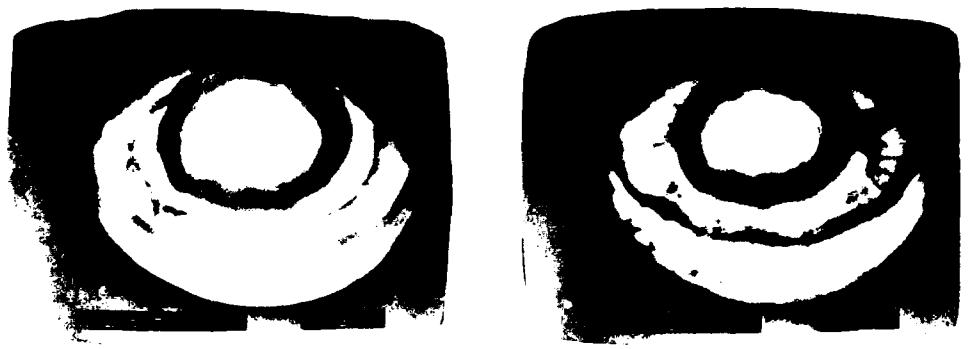

T=0.392 T=0.525

T=0.442 T=0.592

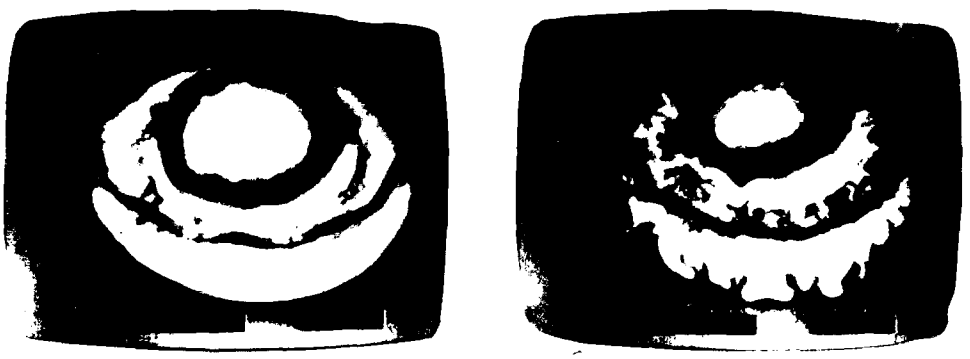

T=0.475 T=0.742

Figure 3.18b (Continued)

as the secondary ring's self-induced propagation velocity. This creates an imbalance in the resultant induced velocity such that the SVR propagates (is ejected) away from the plate, subsequently dragging the tertiary vortex ring along with it. The result is the formation of what appears as a "mushroom" cloud, which is shown rather vividly in Figure 3.17b. Figures 3.18a and 3.18b show an oblique plan view of the same development of the kink-structured SVR and its subequent ejection.

Figure 3.19 illustrates the trajectories (as observed in side-view) of the primary, secondary and tertiary vortex rings for a typical ejection type impact. One can observe two occurrences of rebound and reversal in the trajectory of the primary vortex ring. The secondary vortex ejection phenomenon is clearly displayed by the SVR's trajectory.

Far from the surface the PVR propagates downward because of its self-induced propagation velocity as shown in the initial portion of curve I in Figure 3.19. As it nears the surface, its diameter increases because of the image vortex effect caused by the surface. At point A, a secondary vortex ring is generated through viscous effects. Between this point and point B, the PVR rebounds away from the surface and experiences a reversal in its radial velocity. This is caused by the mutual interaction with the SVR which is orbiting over the PVR. As the SVR orbits toward the inside of the PVR, the primary vortex begins to again migrate toward the surface. During this downward movement, viscous effects create a tertiary vortex ring which is formed at point B. As the PVR continues to approach the surface, its diameter again begins to increase because of image vortex effects. During the time from point B to the last timing mark, the SVR, influenced primarily by the PVR, continues its orbit over and into the center of the PVR. The PVR then undergoes a second rebound and reversal caused by the orbit of the tertiary vortex ring over the PVR.

When the TVR reaches a position above the PVR coincident with the last timing mark on the trajectory curves, it is close enough to exert a significant influence on the motion of the SVR. At this point in time,

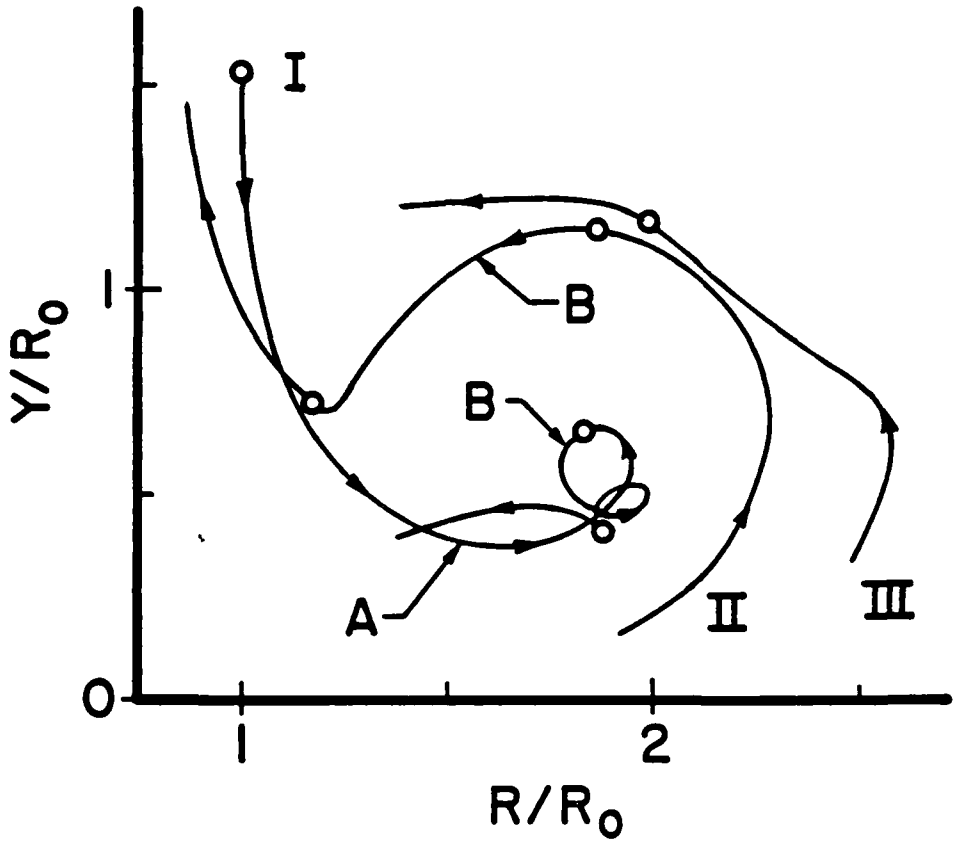

Figure 3.19 Trajectories of the right cores of the primary, secondary, and tertiary vortex rings. Curve I: Trajectory of the primary vortex ring. Curve II: Trajectory of the secondary vortex ring, Curve III: Trajectory of the tertiary vortex ring. Point A on curve I coincides in time with the origin of curve II. Point B on curves I and II coincides in time with the origin of curve III. O Marks time intervals of 0.5 seconds. Vortex ID.#52.265, Re_o=2840. Observe the rebound and reversal of the primary vortex and ejection of the secondary vortex.

the SVR begins to propagate away from the surface rather dramatically. As pointed out earlier, the addition of the velocity induced by the TVR to the self-induced propagation velocity of the SVR causes the SVR to propagate away from the PVR and the surface. Over the period following the last timing mark until its complete dispersal, the diameter of the PVR is permanently decreased both in response to the influence of the secondary and tertiary vortex rings, and as a result of the diminished strength of the image vortex effect due to the dispersal of much of the initial vorticity of the PVR.

The secondary vortex ejection as described above was observed to occur with varying degrees of coherency over the range of Reynolds numbers examined. In some cases, as in the sequences shown here, the secondary vortex would appear very ring-like and well structured, i.e. the SVR was not significantly deformed by any three-dimensional interaction with the PVR and TVR. In other cases, the secondary vortex would appear as a very turbulent vortex ring or even degenerate to a turbulent mass of fluid during the ejection process. The coherency of the secondary vortex ring, as it propagated away from the PVR seemed to depend upon the extent to which the SVR interacted with the PVR and the TVR. More experimental investigation and analysis would be necessary to more closely establish the cause for this behavior.

As complex as the interaction of the primary, secondary, and tertiary vortices already appears to be, it becomes even more complicated when one attempts to explain how the vorticity of the primary vortex is dispersed. As in the loop-structured case, the initial dispersal of vorticity occurs with the generation of the SVR and TVR. However, as already stated, the vorticity of the primary vortex ring is further dispersed by filaments of vorticity which wrap around it. Figure 3.20 is an oblique plan-view sequence of one half of the vortex ring which illustrates the development of these vortex filaments.

The first two photographs in the sequence (obtained using dye on the surface) show the secondary vortex ring just after formation and after it has orbited into the center of the PVR and developed a kinked-structure. The third picture reveals a sheet of dye passing over the

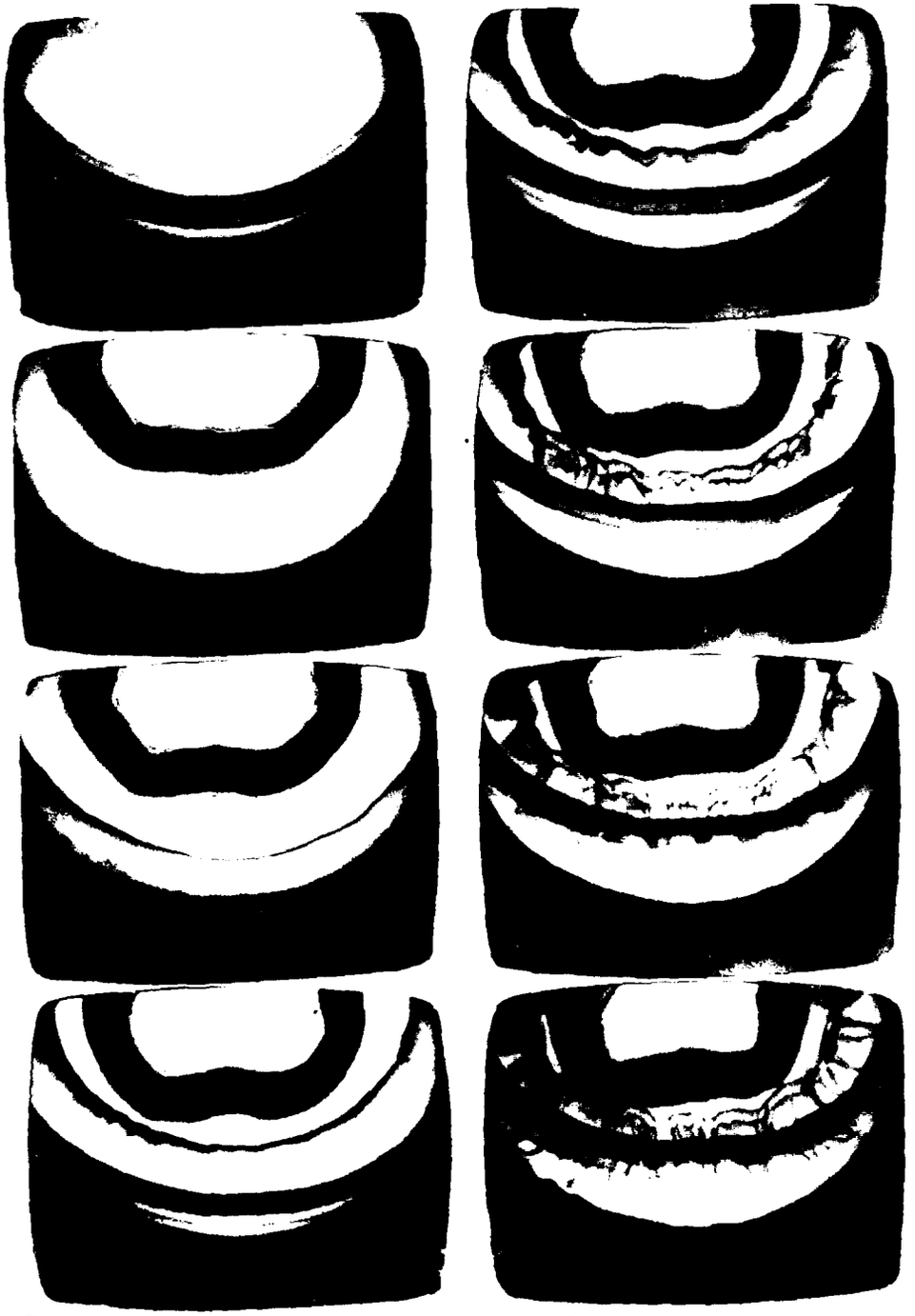

Figure 3.20a Detailed interaction of primary, secondary, and tertiary vortices during secondary vortex ejection (oblique plan view of half of vortex ring, dye on surface). Vortex ID.#52.265, Re_0=3000 Times of pictures are 0 0, 0.275, 0.367, 0.433, 0.467, 0.500, 0.533, 0.558 sec. Sequence continued on next page.

Figure 3.20b Detailed interaction of primary, secondary, and tertiary vortices during secondary vortex ejection (oblique plan view of half of vortex ring, dye placed on surface). Times of pictures are 0.583, 0.625, 0.667, 0.717, 0.733, 0.775, 0.925, 1.21 sec. Sequence is continued from previous page.

top of the core of the PVR following the path of the SVR. Note that the edge of the dye sheet is somewhat smooth and continuous, indicating that the sheet is travelling at a relatively uniform velocity around the circumference of the PVR. In the fourth photograph of the first column, the tertiary vortex ring has formed and the dye sheet has reached a position directly above the core of the PVR. In the first picture of the second column, the dye passes between the cores of the primary and secondary vortex rings and is accelerated by the velocity field of the SVR. At this point, one can begin to see undulations in the leading edge of the dye sheet. These undulations, which are apparently caused by the variations in proximity of the secondary vortex ring to the primary vortex ring due to the kinked-structure of the SVR, result in circumferential variations in the velocity of the dye sheet. The faster moving regions occur where the PVR and SVR are in closest proximity, likewise the slower regions will develop where the two vortices are farther apart.

The last three photographs in the second column of Figure 3.20a show both the growth in the undulations of the leading edge of the dye and the continued orbit of the tertiary vortex ring around the core of the PVR. In these photographs, the thinly dyed regions become difficult to see because of the brightness of the back lighted background.

The undulations in the dye sheet indicate the presence of three-dimensional velocity gradients and thus vorticity. As this vorticity is stretched under and around the core of the PVR, small pockets can be seen to form in the edge of dye on the surface beneath the PVR. These pockets subsequently develop into the mushroom shapes associated with pairs of counter-rotating vortices. This pocket-mushroom shape development can be seen beginning with the last photograph of the first column of Figure 3.20b and continuing through the next two pictures of the second column. These mushroom shapes are indicative that the stretching of the vorticity in the undulating dye sheet (as it is wrapped around the core of the PVR) results in the formation of very coherent pairs of vortices. Throughout this process of formation of

AD-A138 999 EXPERIMENTAL OBSERVATIONS OF VORTEX RING INTERACTION WITH THE FLUID ADJAC..(U) LEHIGH UNIV BETHLEHEM PA DEPT OF MECHANICAL ENGINEERING AND M.. A W CERRA ET AL. 2/2

UNCLASSIFIED OCT 83 FM-4 AFOSR-TR-84-0130 F/G 20/4 NL

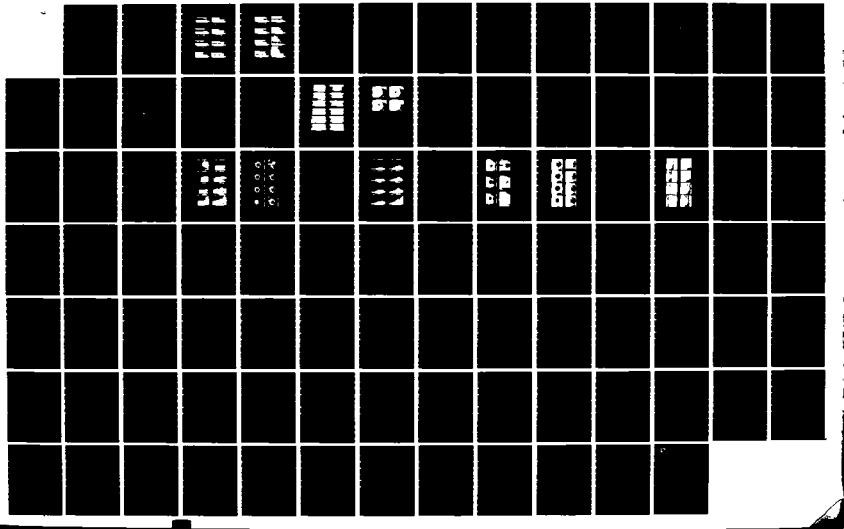

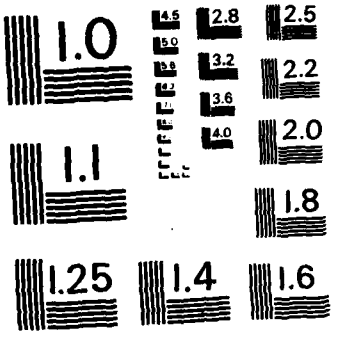

vortex filaments, the SVR has remained essentially in the center of the PVR, and the TVR has been slowly orbiting over the PVR. In the second and third pictures of the second column of Figure 3.20b the SVR is beginning to move upward from the surface, out of the view of the camera. As it moves upward, it causes a very intense stretching of the vortex filaments, which interact very strongly with the PVR resulting in a rapid, almost explosive dispersion of the remaining organized vorticity in the PVR. As shown in the last picture of Figure 3.20b, the scale of the residual vorticity and coherent motions have been drastically reduced yielding a dispersed mass of apparently turbulent fluid.

A side-view of the vorticity dispersion process during a secondary vortex ejection is shown in Figure 3.21. In the first two photographs of Figure 3.21a, the SVR has formed and is orbiting over the top and toward the center of the PVR. The following four photographs show the separation and roll-up of fluid into the tertiary vortex ring. In the last two photographs of the second column, one can just barely see the leading edge of the dyed sheet referred to in the plan-view of Figure 3.20. The fluid in the dye sheet appears to be part of a continuous sheet or layer of the fluid which separates from the boundary layer (created by the viscous interaction of the PVR with the surface) and rolls up into the tertiary vortex. For some reason, not all of the fluid is rolled up into the tertiary vortex ring. This fluid is then pumped or accelerated between the primary and tertiary vortex rings because of the velocity fields induced by these vortex rings. The arrows in the last two photographs of column two of Figure 3.21a point to the leading edge of this dyed fluid as it travels over the top of the PVR. In the first photograph of Figure 3.21b, the leading edge of the dyed fluid is now between the cores of the primary and secondary vortices. One can see the undulations just beginning to form in this fluid. In the second photograph striations begin to form in the sheet as a result of the variations in velocity caused by the kinked secondary vortex, as explained earlier. One can also see what appears to be a

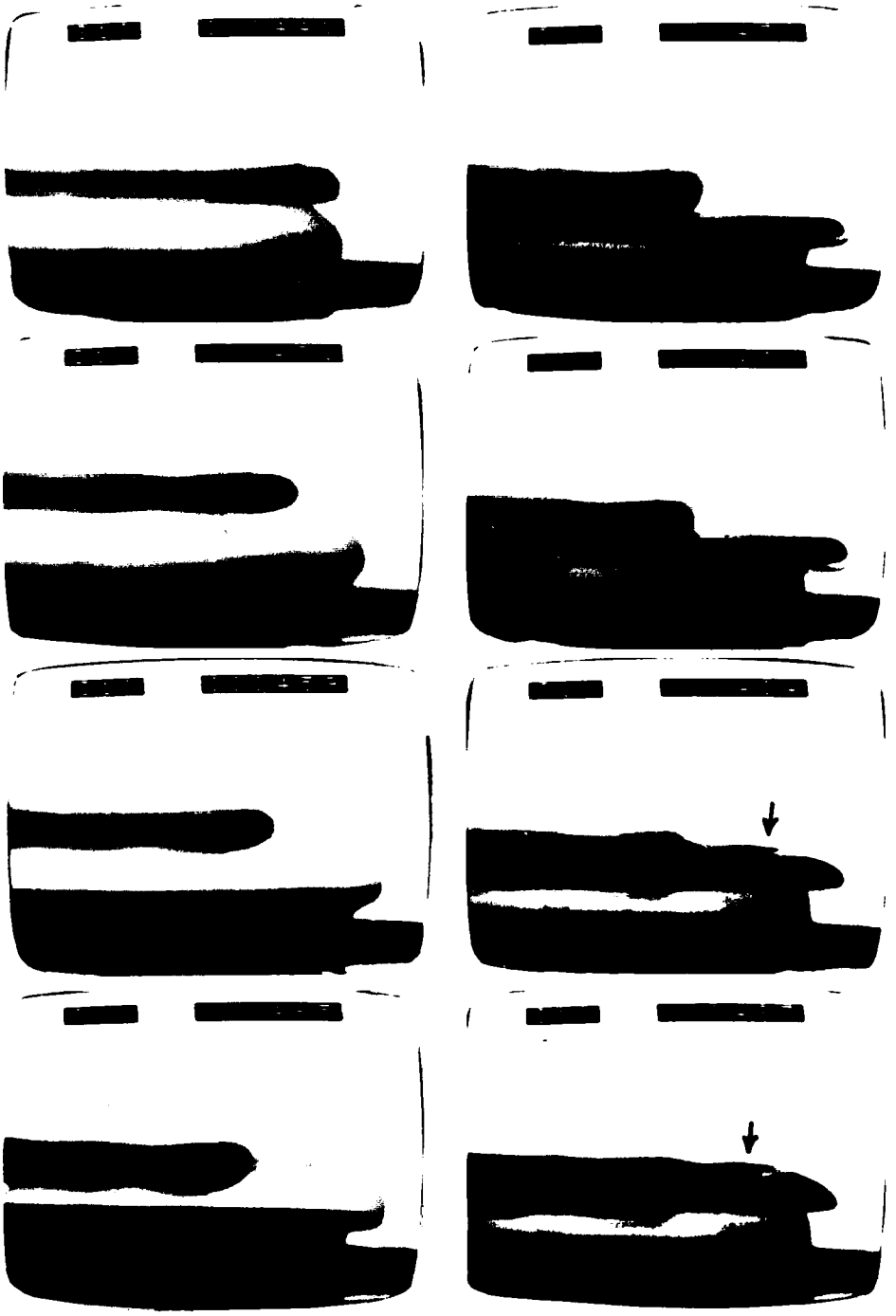

Figure 3.21a Detailed interaction of primary, secondary, and tertiary vortices during secondary vortex ejection (side view of right halves of vortices, dye placed on surface). Vortex ID. #52.265, Re_0=3000. Times of pictures are 0.0, 0.092, 0.150, 0.200, 0.258, 0.308, 0.358, 0.383 sec. Sequence continued on next page.

Figure 3.21b Detailed interaction of primary, secondary, and tertiary vortices during secondary vortex ejection (side view of right halves of vortices, dye placed on surface). Times of pictures are 0.458, 0.525, 0.592, 0.633, 0.675, 0.783, 0.942, 1.1 sec. Sequence is continued from previous page.

fourth vortex attempting to form near the outer edge of the PVR. This is indicative of additional fluid separating from the boundary layer as the primary vortex again travels down toward the surface after the second reversal (caused by the tertiary vortex ring). Apparently this additional separation of fluid does not have sufficient vorticity to roll up into an additional vortex ring. Note that at this point the dyed sheet of fluid previously referred to has not yet reached this newly separated fluid. In the third photograph, the dyed sheet has caught up with the newly separated fluid. The third and fourth photographs of Figure 3.21b now clearly show striations developing in the dyed sheet. Starting with the fourth photograph, the dyed fluid passes over the top of the PVR again. At this point the dyed sheet will take either one of two directions. Some will travel up between the secondary and tertiary vortex rings, and some will continue around the PVR, again passing down between the primary and secondary vortices. This splitting of the dye sheet is observed through the second photograph of column two. By this point, the SVR has already begun to move vertically away from the surface, initiating the intense stretching of the vortex filaments (indicated by the striations in the dye sheet) which causes the final dispersion of the PVR. This rapid dispersion is observed in the last two photographs, as the entire PVR flow pattern degenerates into small scale motions due to the rapid stretching and twisting of the vortex filaments. As the secondary vortex, and to some extent the tertiary vortex, move upward from the surface, they also become less coherent through an apparent interaction with the stretched vortex filaments (this is more clearly seen in Figure 3.17b).

The process by which the vorticity of the PVR is dispersed for the kink-structured SVR case as just described is very complicated. Vorticity is incrementally dispersed at first in the production of the SVR and the TVR. Azimuthal waviness in the SVR further induces vorticity filaments which then wrap around the PVR. The stretching of these filaments during the ejection of the SVR subsequently causes three-dimensional relocation of fluid in the PVR, which results in the breakdown

of the PVR. As the PVR, SVR, TVR, and these vortex filaments interact in an increasingly complicated manner in accord with the laws of vortex dynamics, the scales of fluid motion continuously decrease until the vorticity of the PVR becomes fully dispersed throughout the fluid, subsequently decaying due to viscous effects.

3.1.5c Summary of SVR Structure

Upon impact with a surface, vortex rings of Reynolds number greater than 350 will form a secondary vortex ring of opposite vorticity as a result of a viscous boundary layer separation process. The formation of the SVR and later the TVR represent a segmentation process by which a portion of the vorticity of the PVR is initially dispersed into originally quiescent fluid. The remaining vorticity in the PVR is dispersed via the inviscid interaction of the PVR, SVR, and TVR. As these vortices interact, vortex filaments wrap around the PVR causing the three-dimensional breakdown of the PVR.

The SVR develops from the separation and rollup of the boundary layer induced by the PVR when it nears the surface. After formation, the SVR develops an azimuthal waviness as it orbits above and into the center of the PVR. At this point the SVR will evolve into either a loop-structured or a kink-structured vortex ring depending on the Re_o of the PVR as already explained.

For a loop-structured SVR, the azimuthal waves increase in amplitude to a point where the SVR develops into a three-dimensional vortex loop with azimuthal loops of large amplitude as illustrated by Figure 3.13. As the PVR and SVR interact in Biot-Savart manner, the ends of the loops in the center tend to propagate vertically due to self-induced velocity effects, whereas the ends closer to the PVR become wrapped around the core of the PVR. As loops of the SVR wrap around the PVR, the vorticity of the PVR is dispersed by the three-dimensional interaction of the vortices.

The kink-structured SVR is differentiated from the loop-structured SVR by the small amplitude of its azimuthal waves and its ejection away from the surface. Although the SVR itself does not appear to develop loops which wrap around the PVR, it does induce apparent vortex filaments

which wrap around the PVR, causing a dispersal of the vorticity of the PVR. Because the SVR remains somewhat coherent throughout the interaction process, it retains a significant self-induced propagation velocity which, when added to the velocity induced by the TVR, causes an ejection of the SVR away from the surface.

The process by which the vorticity of the PVR is dispersed changes as the Re_0 of the PVR changes. The physical mechanism responsible for this change in behavior appears to be the change in strength and stability of the SVR. At low Re_0 (below 350), no SVR forms and vorticity dispersal occurs by laminar diffusion. In the Re_0 range over which an SVR forms, vorticity dispersal occurs as a result of interacting vortex filaments which wrap around the SVR. Very early in this Re_0 range, the SVR develops a loop structure from an instability which causes an azimuthal waviness in the SVR. As the Re_0 increases, the number of waves or loops increase. As the Re_0 increases further, fewer of the loops wrap around the PVR and the wave or loop amplitude decreases as the strength of the SVR appears to increase, the structure of the SVR is changing from a loop to a kink structure. As the Re_0 increases through the range investigated, the SVR seems to be less influenced by mutual induction with the PVR (i.e. the wrapping of the SVR loops around the PVR) and is more influenced by its own self induction and mutual induction with the TVR (i.e. the ejection of the SVR away from the PVR and the surface). However, as described in detail earlier, the vorticity of the PVR is ultimately dispersed by the interaction of vortex filaments wrapping around the PVR for both the loop and the kink-structured SVR.

3.1.6 Quantitative Results

3.1.6a Nondimensional Time to Formation of the Secondary Vortex

The time to formation of the SVR was measured in reference to the point in the trajectory of the PVR when it was one diameter away from the surface. As stated earlier, the SVR has its origin from both originally quiescent fluid and fluid from the PVR. For this measurement

the formation of the SVR was defined as the point in time when the boundary layer had separated and begun to roll up and form the SVR. Since the trajectory of the PVR and the boundary layer flow were not visualized simultaneously, the point of boundary layer separation and rollup was arbitrarily designated as the point when the core of the dyed PVR was deformed such that a noticeable concavity appeared in its outer surface. This measurement is very sensitive to the subjective interpretation of the observer. As an example of the degree of core deformation required to indicate the formation of the SVR, in Figure 3.2 the point of formation of the SVR was determined to occur between the second and third photographs of the first row.

The normalized time to formation of the SVR was defined as:

$$T_s = \frac{t_s V_0}{D_0} \tag{3-3}$$

where

T_s = normalized time for formation of the SVR

t_s = actual elapsed time from the point at which the PVR is one diameter from the surface to the point of formation of the SVR

V_0 = initial velocity of the PVR

D_0 = initial diameter of the PVR.

A plot of T_s versus Re_o compiled for 72 separate cases is shown in Figure 3.22. Note that T_s appears to change very slightly if at all with Re_o. At lower Reynolds numbers there is a larger variation in T_s which is felt to be the result of uncertainty of the data measurements, and the subjectivity in establishing the formation of the SVR. A lower Reynolds number is indicative of a weaker PVR and a correspondingly weaker SVR. The weak SVR results in a smaller deformation of the core of the PVR which makes the determination of T_s more uncertain. To indicate the high uncertainty of these lower Reynolds number measurements, the corresponding data symbols have been filled in. A best fit average value of all the T_s measurements is 1.3 with a standard deviation of 0.3.

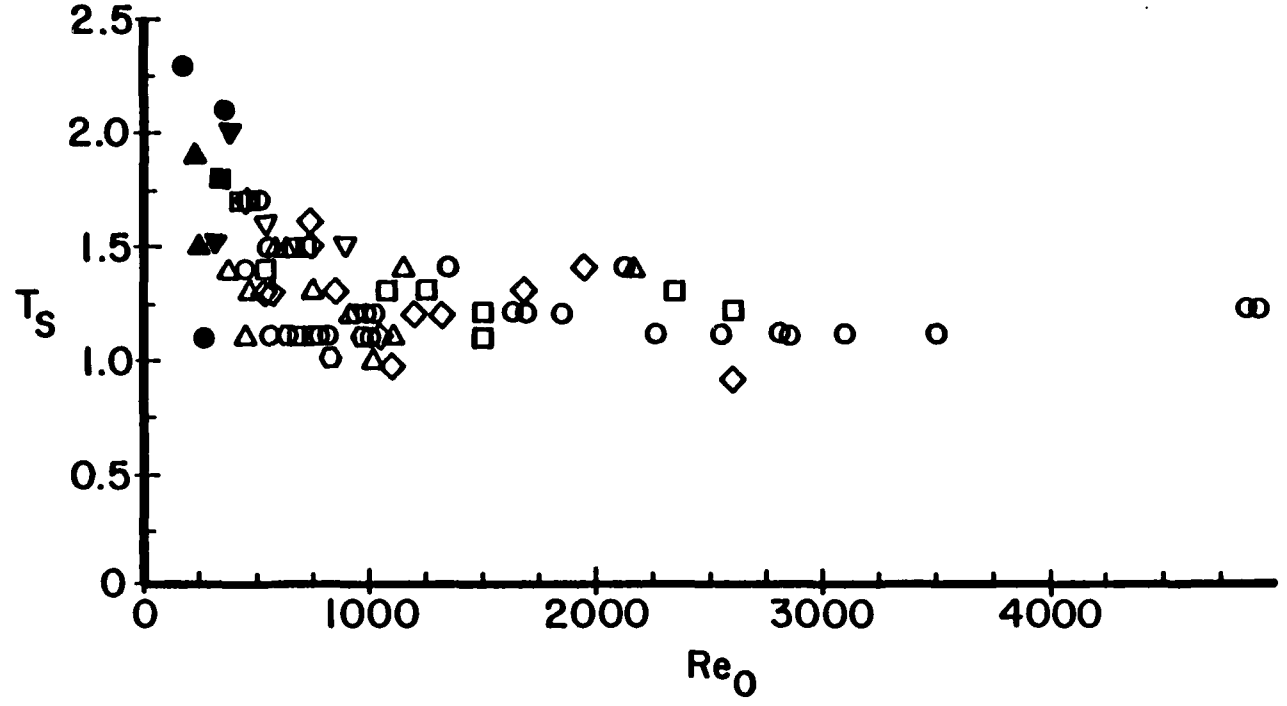

Figure 3.22 Nondimensional time of observation of the secondary vortex, $T_S=t_S V_O/D_O$ vs. Re_O. ▽, D_M=0.95 cm., △, D_M=1.4 cm.; ◇, D_M=1.9 cm.; □, D_M=2.2 cm.; ○, D_M=2.5 cm.; ⬡, D_M=3.2 cm. Solid symbols represent very weak vortices and indicate data based on very subjective observations.

Comparison of the experimental results was done with the numerical analysis by Doligalski (15) [described in Chapter 1] of the growth of a boundary layer on a flat plate caused by the approach of a circular vortex ring. His analysis confirms that the boundary layer will separate and form an eddy which will develop into a secondary vortex ring of vorticity opposite that of the PVR. His analysis predicts a T_s value of 0.92, established by the point where he could first detect a secondary eddy formation (with closed circular streamlines) within the developing boundary layer. This value agrees favorably with a value of 1.25 determined experimentally for the same set of vortex parameters as evaluated numerically by Doligalski. It is not surprising that the numerical value is less than the experimental value because the method of definition of the numerical and experimental time differed slightly. Whereas Doligalski could directly determine the point of initial eddy formation in the boundary lyaer, the experimental values are based on the point where the effect of the eddy formation on the visualized PVR could be clearly detected. Thus, one would expect a lag in time between the initial eddy formation and when it has grown to sufficient strength and size to have the required observable effect on the PVR.

3.1.6b Instability of the SVR: Number of Azimuthal Waves

As already indicated, after formation the SVR develops azimuthal waves as it orbits above and into the center of the PVR. The number of waves formed, N, were determined for a number of vortex rings with L_M/D_M of 1.6 and 2.2. The results of these determinations are presented as a function of Re_o in Figure 3.23, which indicates that an apparent relationship exists between the number of waves observed and the initial Re_o of the PVR. The line on the plot is a least squares linear regression curve fit of the data.

The number of waves is obviously a result of the complicated flow interaction occurring between the SVR and the PVR. As discussed in section 3.1.4b, the compression of the diameter of the SVR as it orbits

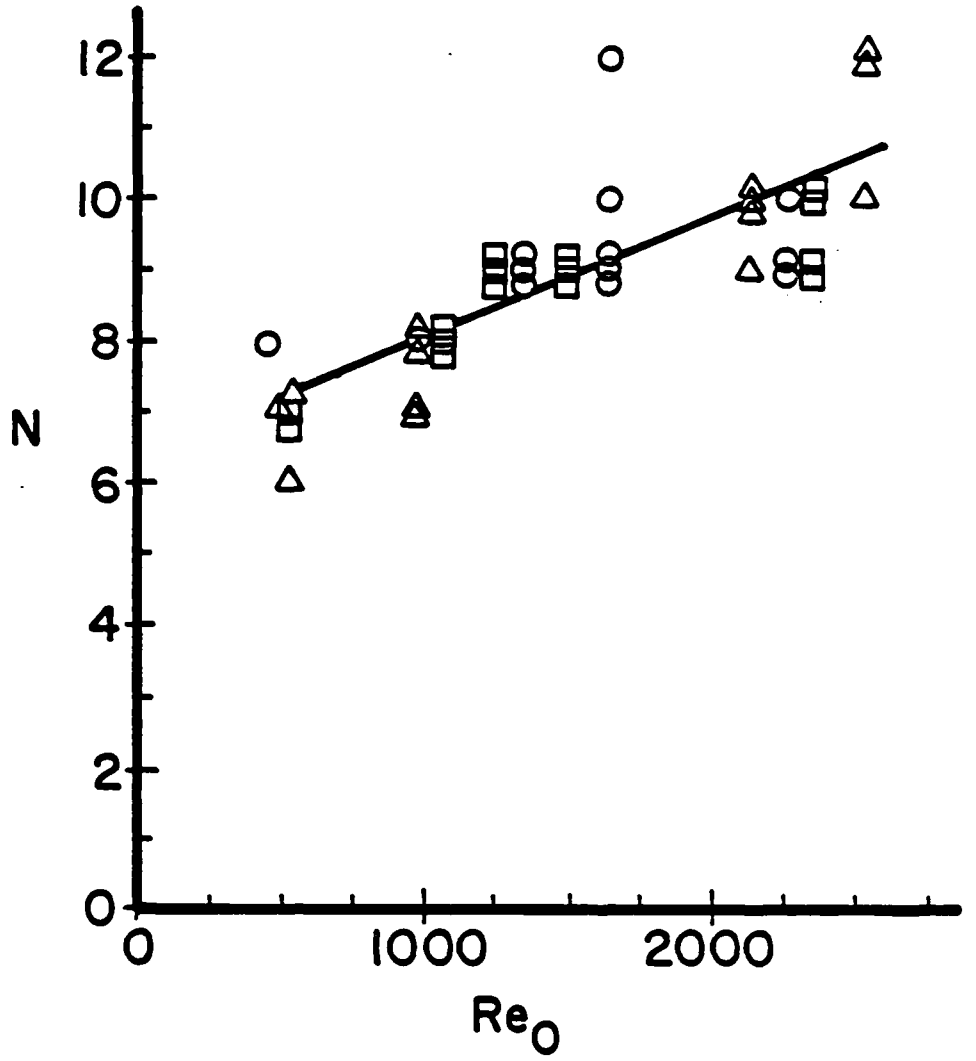

Figure 3.23 Number of waves in secondary vortex ring, N vs. Re_0 for constant L_M/D_M and D_M. □ , L_M/D_M=1.6, D_M=2.2 cm.; ○ , L_M/D_M=1.6, D_M=2.5 cm.; △ , L_M/D_M=2.2, D_M=2.5 cm.

above the PVR would seem to be the major cause of the instability. The flow interaction with the PVR and the velocities induced by each vortex then determine how much the waves deform. If much deformation takes place, a loop-structured SVR is formed; if little growth occurs, a kink-structured SVR is formed.

The possibility also exists that the number of waves may be related to an initial instability of the PVR. Many investigators, including Krutzsch (39), Maxworthy (51-53), Widnall et al. (100,101) and Didden (13), have observed the instability of a vortex ring in free fluid far from any boundaries. The instability for such a ring at manifests itself as an azimuthal waviness which grows in amplitude at 45 degrees to the direction of propagation. The waviness neither grows nor rotates around the vortex core. The waves grow to finite amplitude and then apparently break, transforming the laminar ring into a turbulent ring (53).

Widnall et al. (100,101) performed a number of analytical and experimental studies of a vortex ring in a free fluid. This analysis shows that a vortex ring of small but finite core size in an inviscid fluid is unstable to small sinusoidal displacements of its centerline. The number of waves depends on the core size; as the core size decreases, the number of waves increases.

In their experimental study they used flow visualization and laser-doppler-velocimetry techniques to determine the number of waves and vortex ring characteristics such as circulation, Γ, translational velocity, V_o, and core size, a. Their results take the form of a plot of the number of waves, N, versus a nondimensional velocity, $\bar{V}$,

$$\bar{V} = \frac{V_o}{\Gamma/4\pi R} = \ln(8R/a) + A - \tfrac{1}{2} \qquad \text{where}$$

V_o = translational velocity

Γ = ring circulation

R = ring radius

a = core size

A = a constant which is a function of the vorticity distribution

Basically, their experimental results indicate a reasonable agreement with their theory.

Maxworthy conducted several experimental studies of vortex rings during which he observed the aforementioned instability of the initial ring. From his observations, he proposed the unproven theory that the instability is caused by secondary vorticity of opposite rotation, created at the outside wall of the orifice, which is swept into the main vortex ring. This secondary vorticity creates a layer on the outside of the ring which is unstable by Rayleigh's criterion because the square of the circulation decreases rapidly outwards (51).

In a study using laser-doppler-velocimetry and flow visualization techniques Maxworthy determined that both the number of waves observed in the vortex ring and the reciprocal of the core diameter increase monotonically with Re_M, the Reynolds number of the fluid slug ejected from the nozzle. Furthermore, he determined that

$$\lambda/a = \text{constant}$$

where

$\lambda = \pi D/N$ (λ is the wave length of the waves)

N = the number of azimuthal waves

D = vortex ring diameter

a = vortex core diameter.

His results take the form of a plot of the number of waves at instability versus Re_M.

Didden (13) performed several experiments similar to those of Maxworthy in which he investigated laminar, unstable vortex rings by means of laser-doppler-velocimetry techniques. His study provides the most extensive quantitative information on vortex rings formed by expelling fluid from tubes (76). Because his report was written in the German language, the authors are only able to discuss his graphical results, particularly a plot of N versus Re_o, the initial Reynolds number of the vortex ring.

3.1.6c Comparison of the Instability of a Vortex Ring in a Free Fluid with that of the SVR

To examine the possibility that the wave behavior observed for the SVR is the direct consequence of an existing instability of the PVR prior to impact, the wave number results for a vortex ring in a free fluid as previously reported in the three studies of Widnall et al. (11), Maxworthy (53), and Didden (13) are compared to the wave number results for the SVR as determined by the present study.

Experimental data for the number of waves observed in an SVR from this study are compared in Table 3.1 to the data reported by Widnall et al. (100) for the number of waves in a vortex ring in a free fluid. The number of waves, N, is shown as a function of $\bar{V}$ as previously defined.

Table 3.1

Comparison of the Number of Waves Observed in this Study for an Unstable SVR with Those Observed by Widnall et al. (100) for an Unstable Vortex Ring in a Free Fluid

Waves in SVR	$\bar{V}$	Waves in Vortex Ring in Free Fluid	$\bar{V}$
7	2.31	6	2.52
7	4.57	7	2.46
8	4.41	8	2.77
8	4.61	12	3.16
9	5.65		
9	4.40		
10	4.92		

There appears to be little correlation between the two sets of data. This is most likely due to the different methods of determining the circulation used in the two studies. Widnall et al. (100) used a laser-doppler-velocimeter to experimentally determine the circulation of the vortex ring at a station downstream of the generating orifice. In the present study, because such equipment was not available, an estimate of the initial circulation at the orifice was used. This

estimate of the circulation was determined from the measured piston displacement curve and a simple "slug" model of the amount of vorticity formed at the orifice (53). This technique of estimating the circulation will be discussed further in appendix A. Because of the poor correlation of results, no conclusions regarding the influence of a possible instability in the PVR can be drawn from this comparison.

To properly compare Maxworthy's data, his Re_M data had to be converted to Re_o data. In his paper (53), he provides a table of L_M/D_M, Re_M, and Re_o for 20 data points covering a L_M/D_M range of 0.66 to 1.51 and an Re_o range of 18,000 to 30,000. This data was curve fitted using a least squares linear regression analysis and plotted in Figure 3.24. At an L_M/D_M equal to 1.5, which was used to generate Maxworthy's N versus Re_M data, Re_o/Re_M equals 0.386. This value was then used to determine the Re_o corresponding to Re_M values reported by Maxworthy. For comparison, Re_o/Re_M versus L_M/D_M data from Didden (13) and the present work are also plotted in Figure 3.24. The data from the present work and Didden's work appear to correspond reasonably well, considering the scatter of the present data. Maxworthy's data indicates that Re_o/Re_M changed less with L_M/D_M than is indicated by the present data and Didden's work. The difference in trends may be due to differences in the Reynolds number ranges over which the ratio was evaluated. Maxworthy's data ranged from an Re_o of 18,000 to 30,000, whereas the data of Didden ranged from 725 to 3300 and from 125 to 5000 for the present study.

Table 3.2 compares the curve fit of N vs. Re_o for the SVR shown in Figure 3.23 to the curve fit of Maxworthy's (53) N versus Re_M (converted to Re_o) data and Didden's (13) N versus Re_o data for PVR instability.

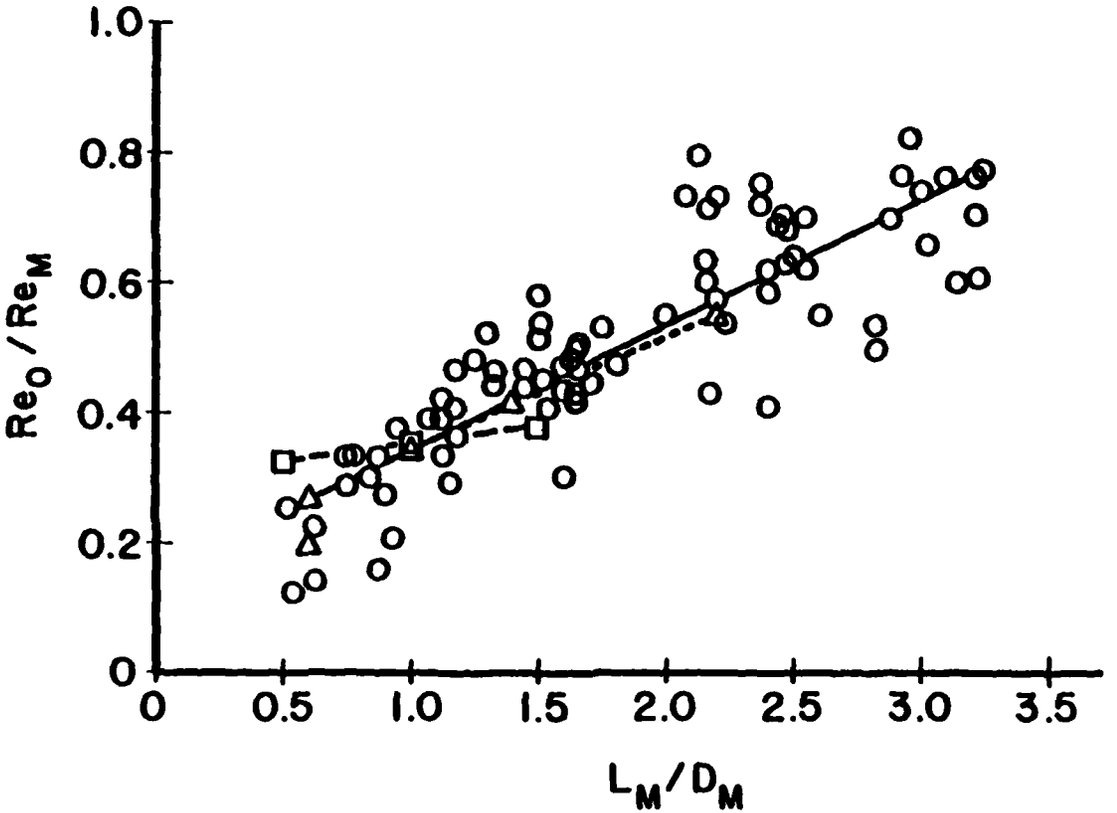

Figure 3.24 Plot of Re_o/Re_M vs L_M/D_M. O——O Experimental data from the present study. Δ-----Δ Data from Didden (13). □--□ Data from Maxworthy (53).

Table 3.2

Comparison of the Number of Waves Observed in this Study for an Unstable SVR With Those Observed by Didden (13) and Maxworthy (53) for an Unstable Vortex Ring in Free Fluid

Re_o	Waves in SVR	Waves in Vortex Ring in Free Fluid Didden (13)	Waves in Vortex Ring in Free Fluid Maxworthy (53)
500	7.2	5	5
1000	8.0	6	6
1500	8.8	7.1	7.1
2000	9.7	7.9	8
2500	10.5	8.6	8.7

The data of Didden and Maxworthy agree very well for the number of waves of an unstable vortex ring in a free fluid. However, the number of waves observed for a secondary vortex ring appears to be approximately two wave numbers higher than the number observed for a comparable vortex ring in a free fluid.

The conclusion to be drawn from this comparison is that it does not appear that an instability in the PVR before impact imposes its wave number on the secondary vortex ring. Rather, the instability and hence the wave number of the SVR probably results from the complex interaction of the PVR and SVR which occurs as the SVR orbits the PVR and decreases in diameter. In this interaction the mutual and self-induced velocities would seem to play an important role.

3.2 IMPACT OF A VORTEX RING WITH A FREE SURFACE

To investigate the effect of surface condition, several experiments were perfor ed in which vortex rings of identical initial conditions impacted n oth solid and free surfaces. The vortex ring generator was con shown in Figure 2.6 such that the vortex ring would propagate ov the free surface. To perform the solid surface case, a flat bottomed plexiglass boat was floated on the surface.

One vortex ring, ID #51.825, was generated with an orifice 2.54 cm in diameter located 3.5 ring diameters from the surface. The vortex ring, formed from an ejected slug 1.8 diameters in length, had a moderate Re_0 of 1200.

In this experiment the impacting vortex rings behaved very similarly, if not identically, for the two different surfaces. Figure 3.25 shows side-by-side views of a vortex ring impacting both a free and a solid surface. The only significant difference in the two sets of photographs is the initial concentration of the dye in the PVR. Note that secondary and tertiary vortices form for both surface conditions. An azimuthal waviness in the SVR, which can be seen in the second last photograph of Figure 3.25 and in Figure 3.26, develops into a loop-structured SVR for both interactions. Rebound and reversal are also observed to occur. The times to formation of the secondary vortices are within 5% of each other, which is well within the experimental uncertainty for this determination. All visual aspects of the behavior appear to be essentially identical.

These results are in agreement with the work done by Krauch (38) who observed similar phenomena and found that vortex rings impacting free and solid surfaces behaved very similarly as long as the free surface was not deformed by the vortex ring. Barker and Crow (2) also found that the approach of a two-dimensional vortex pair to a free surface was very similar to that for a solid surface case. However, Barker and Crow did not observe the formation of secondary vortices for either case. Presumably, this is due to a deficiency in their flow visualization and photographic methods, or to the nature of turbulent, very high Reynolds number (25,000 and 75,000) vortices.

As Saffman (75) stated, one would expect a boundary layer at a free-surface to be much weaker than one at a solid-surface because of the difference in slip conditions; in a sense the free-surface boundary layer should experience continuous separation. Secondary vortices should, therefore, not form, or at least be very weak. Since these expectations were not realized, the actual condition of the

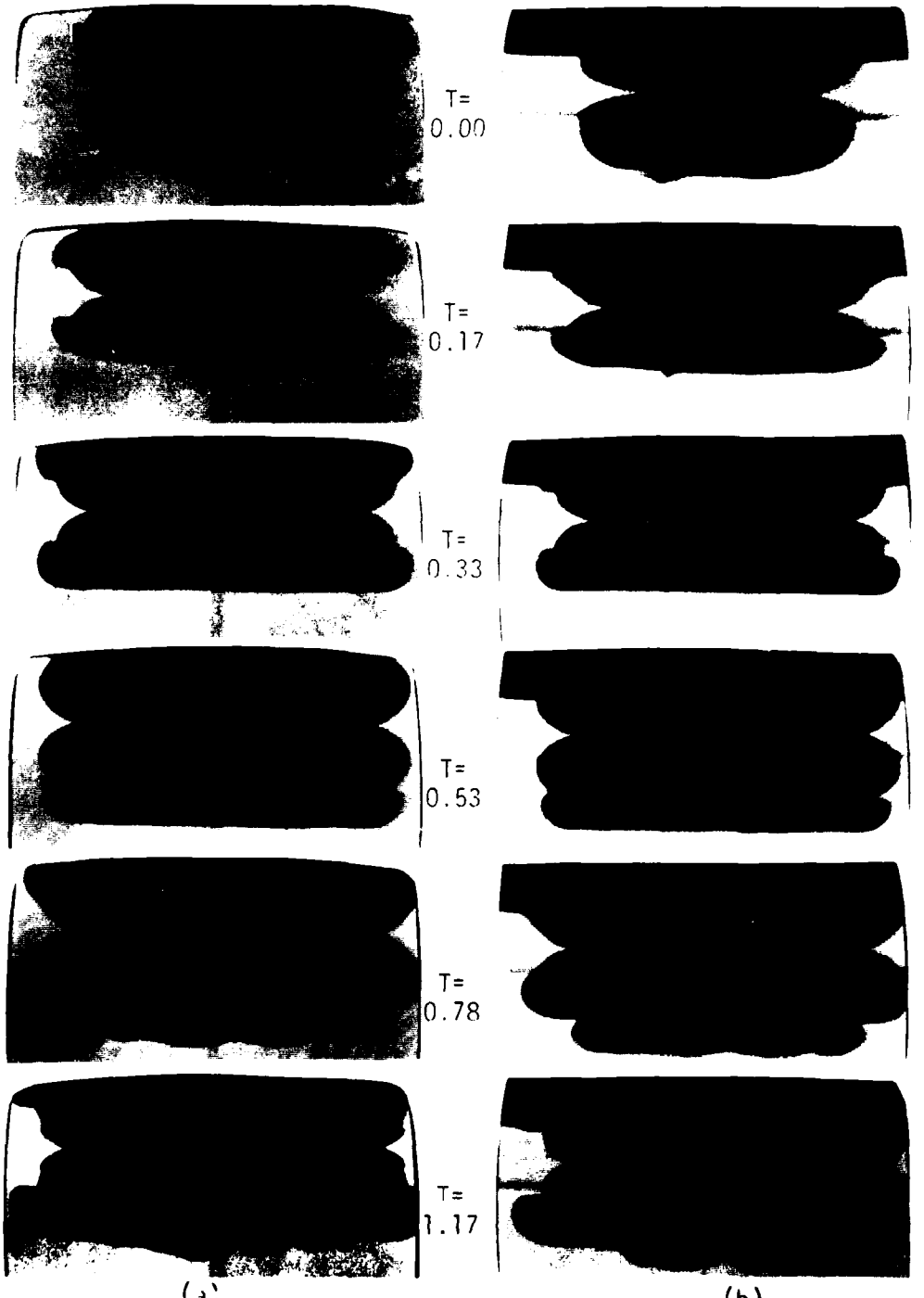

Figure 3.25 Comparison of vortices impacting different surfaces: (a) free plane surface, (b) solid plane surface (side view, dye placed in vortex). Vortex ring travels from bottom to top of picture. Vortex ID.#51.825, Re_0=1200.

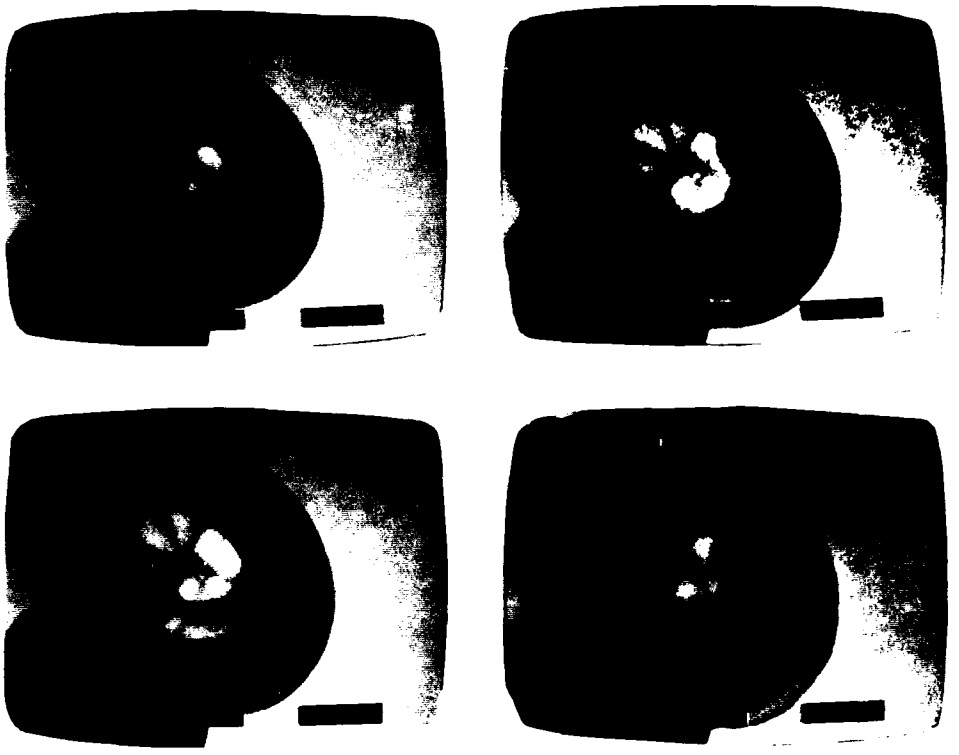

Figure 3.26 Vortex impacting free plane surface (oblique plan view, dye placed in vortex). Vortex ID.#51.825, Re_0=1200. Time between pictures is 0.439 sec.

free-surface was questioned. No surface contamination seemed to be present which would make the free-surface behave like a solid-surface with respect to slip. The possibility that surface tension was responsible for the behavior was then considered.

To test the hypothesis that surface tension effects may (for low Reynolds number vortices) cause the free surface to behave similarly to a rigid surface with respect to slip, a few attempts were made to decrease the surface tension by placing a surfactant (a solution of liquid hand soap and water) on the surface. When a few drops of surfactant were placed on the surface, the surface layer of fluid and contaminants could be observed to break down in a somewhat irregularly shaped region, which fluctuated rapidly in size and shape, eventually reconverging as the effects of the surfactant dissipated. The movement of this layer imposed a velocity condition on the surface as the vortex ring impacted it and grossly affected the behavior of the ring. In an attempt to decrease the area over which the surfactant layer could spread and thereby stabilize the layer, a styrofoam ring was placed on the surface of the water such that the area affected by the surfactant could be confined and stabilized. This attempt also failed. The attempts at modifying surface tension effects were unsuccessful because of an inability to obtain a layer of surfactant which would remain in a stationary equilibrium on the surface. No experimental evidence could therefore be obtained to support the contention that surface tension was responsible for making the free-surface behave like a solid-surface with respect to slip.

From this examination it has been determined that the behavior of a vortex ring of moderate Reynolds number impacting a free-surface will be similar to that of a vortex ring impacting a solid-surface. Visual evidence indicates that the behavior for the free-surface case occurs for the same reasons as that for the solid-surface case, i.e. the vortex ring causes the formation and separation of an induced boundary layer which develops into secondary vortex rings, subsequently interacting with the PVR. The unanswered question seems to be why the free-surface

behaves similarly to the solid-surface with respect to slip. The logical explanation appears to be the effect of surface tension, but attempts to show this were unsuccessful because of an inability to reduce the surface tension of the free-surface and obtain a surface in a state of stationary equilibrium.

3.3 INTERACTION OF A VORTEX RING WITH A DEVELOPING BOUNDARY LAYER ABOVE A SOLID SURFACE

3.3.1 Objective

The primary objective of the work presented above was to develop a better understanding of the behavior and interaction of a ring vortex element in the vicinity of a solid boundary. Hopefully, knowledge gained from these experiments can be applied to the understanding of the behavior and interaction of three-dimensional vortex elements within both turbulent boundary layers and other vorticity dominated flows adjacent to surfaces. To bring these experiments a step closer to this goal, the interaction of a convecting vortex ring (i.e. a simple three-dimensional vortex element) with a laminar boundary layer above a solid surface was examined.

3.3.2 Equipment and Experimental Difficulties

To perform such an experiment, the traversing platform on which the vortex generator was mounted was translated in the streamwise direction with a velocity essentially equal to the free-stream velocity. After ring generation, the interaction of the vortex ring with the boundary layer was viewed and recorded using the cameras and lighting equipment mounted on the translating platform. The flow visualization studies performed included:

1) side and plan-views of the interaction of a vortex ring marked with dyed fluid;
2) side and plan-views with a sheet of dye placed in the boundary layer fluid adjacent to the surface;

3) a plan-view with a sheet of hydrogen bubbles generated by a horizontal bubble-wire adjacent to the surface.

The hydrogen-bubble method is commonly used for visualization of turbulent boundary layers; it is used here to allow the flow behavior observed in the present study to be qualitatively compared with the characteristics observed for turbulent boundary layers.

Only a limited number of the experimental parameters, particularly those involving the generation of the vortex ring, were varied during the course of the experiments. Eight different types of vortex rings were generated; two of these were studied and photographed in detail. The changes made in the generation parameters and their ranges included: orifice diameter (D) 0.95 and 1.90 cm., ejected slug length (L/D) 1.2 to 3.1, height of orifice from surface (H/D) 4.75 and 6.85, and the average ejected slug velocity (U_M) 5.03 to 11.04 cm/sec. The initial Reynolds number (Re_o) of the two vortices studied in detail were 567 and 727. The experimental parameters which were not varied throughout the course of the experiments were: the free-stream velocity (U_∞) of 4.1 cm/sec (yielding a Reynolds number (Re_x) based on the location of the developing boundary layer of 1.96×10^5) and a boundary layer height (δ) of 3.8 cm as measured from photographs of hydrogen bubble lines.

Some difficulties encountered during the experiments required several compromises to be made, primarily with respect to the variation of experimental parameters. One of the more difficult problems was the maintenance of a laminar boundary layer with the vortex generator orifice tube and the plexiglass viewing box immersed in the channel flow. When these parts were stationary just prior to the start of an experimental run, a weak laminar wake would be developed near the free-surface of the flow channel which could destabilize the laminar boundary layer. To minimize this problem, the flow velocity was kept low and the distance over which the platform was moved with the flow prior to the generation of a vortex ring was maximized. Employment of these measures resulted in maintenance of an acceptable laminar boundary layer throughout the entire experimental run.

Another problem involved synchronizing the flow speed with that of the traversing platform such that a stable coherent vortex ring, convecting at the same speed as the surrounding fluid, could be generated. After much trial and error, the appropriate speeds were determined. The carriage speed was set at 3.81 cm/sec, 6.7% slower than the free-stream velocity of 4.08 cm/sec. The small difference in these speeds did not significantly affect the laminar boundary layer due to relative motion effects. The difficulty in synchronizing the flow and platform speeds to obtain a laminar boundary layer and stable vortex rings discouraged examination of a range of flow speeds during these experiments.

3.3.3 Experimental Results

The interaction of a vortex ring approaching a solid surface through a boundary layer flow displays many of the characteristics of a vortex ring approaching a surface through a stationary fluid, in addition to some characteristics which are peculiar to the boundary layer flow case. The characteristics which are similar to the stationary flow case are an increase in diameter in the vicinity of the surface, the occurrence of rebound in the trajectory, and the formation of a secondary vortex ring with its subsequent development of an azimuthal waviness. Those characteristics which are peculiar to the boundary layer case show up in the trajectory of the vortex ring and include a pronounced tilting of the ring.

3.3.3a Trajectory Data

Figure 3.27 shows the trajectory of a vortex ring approaching a solid surface through a boundary layer. The frame of reference for this plot is fixed with respect to the solid surface. The pairs of connected circles indicate the relative positions of the two observable cores of the vortex rings at 0.5 second intervals.

The most immediate feature of this trajectory is the apparent angle of the vortex ring. The first set of circles shows the vortex ring angled at 7 degrees with respect to the surface and the last set

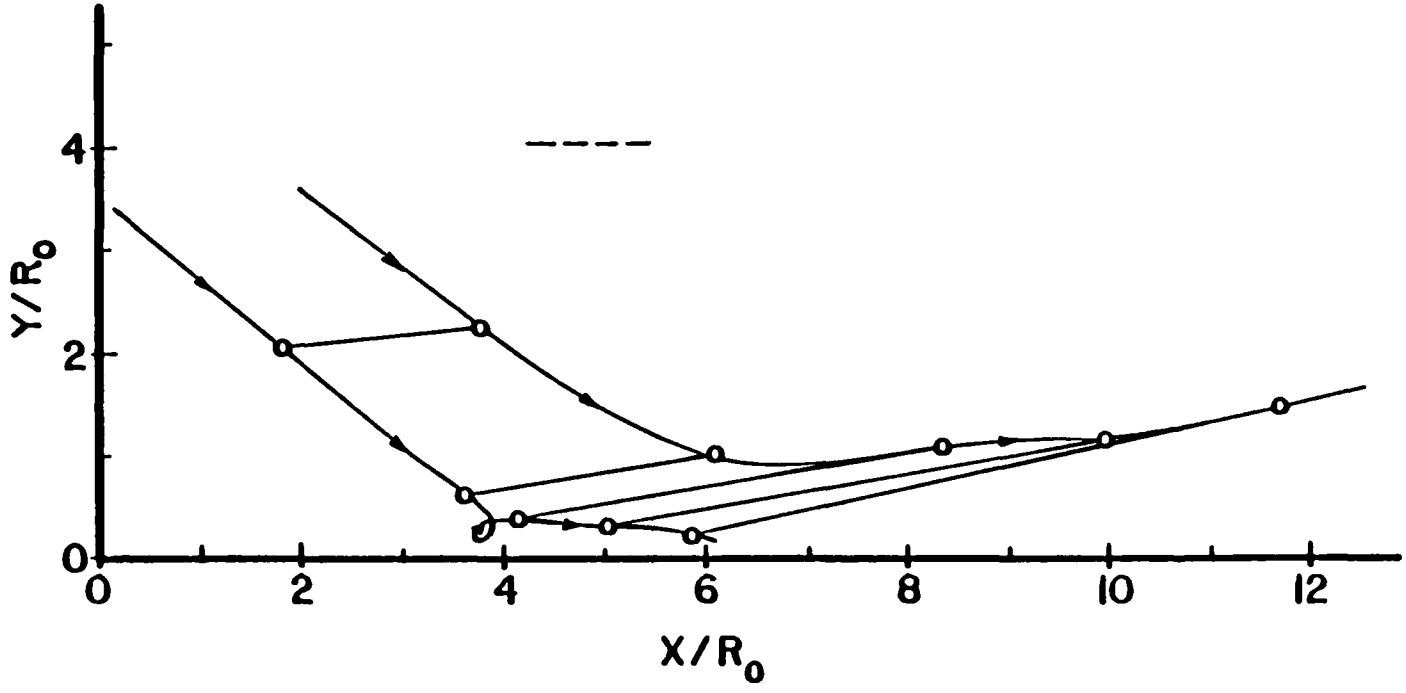

Figure 3.27 Trajectories of the two cores of a vortex ring in a laminar boundary layer above a solid surface. Vortex ID.#31.323, Re_o=727. O——O indicate the relative position of the vortex ring at 0.5 second intervals. Boundary layer thickness δ=3.8 cm. Freestream velocity U_∞=4.1 cm/sec. Vortex ring vertical velocity (Y direction) = 3.53 cm/s. ---- represents edge of boundary layer.

at 12 degrees. In this and several other cases, the vortex ring entered the boundary layer at a slight angle. In the remainder of the observations, the vortex ring initially appeared to be very nearly horizontal with respect to the plate. In all cases, however, the angle of the vortex ring increased as it approached the surface, particularly in the immediate vicinity of the surface. The authors can only speculate on the reason for the inconsistency of the initial angle of the vortex ring. It may possibly be due to flow disturbances occurring near the nozzle and the plexiglass viewing box although, as pointed out above, great lengths were gone to minimize these as much as possible. The increase in angle of the vortex ring as it approaches the plate can plausibly be explained by the interaction of the vorticity of the vortex ring with the vorticity of the boundary layer. The discussion of this interaction will be found below in conjunction with the discussion of the rebound of the vortex away from the surface.

Note that for the case shown, the angle of the initial trajectory of the vortex with respect to the surface has a value of 38 degrees averaged for the trajectory of the two cores. This was essentially consistent for all cases with the same initial conditions.
Another striking feature displayed by Figure 3.27 is the increase in diameter of the ring as it approaches the plate. This increase in diameter occurs in two stages; the first is due to the image effect of the plate, and the second is due to the stretching caused by the boundary layer velocity gradient.

When the vortex approaches the surface, its diameter will increase by image vortex effects (due to the presence of the surface), the same as observed for the stationary case described previously. The small loop occurring in the left trajectory between the second and third circles is caused by the rapid increase in diameter of the ring due to image vortex effects. This increase in diameter is initially greater than the convection velocity of the ring, therefore the trailing or upstream core initially propagates upstream. As this upstream propagation is arrested and overcome by the combined effects of the velocity induced

by the formation of the secondary vortex and a weakening of the PVR due to stretching (as its diameter increases), the convective velocity of the boundary layer becomes dominant causing the vortex ring to turn downstream, thus completing the loop.

The second stage of the diameter increase occurs because of stretching caused by velocity gradients in the boundary layer. For reasons to be explained later, the trailing edge or core of the ring reaches a position which is much lower in the boundary layer and closer to the surface than the position reached by the leading edge or core of the vortex ring. By the very nature of a boundary layer, the convective velocities decrease as one approaches the stationary surface and therefore the trailing core experiences a convective velocity which is less than the velocity of the leading core. This results in the stretching of the vortex ring in the streamwise direction. This stretching due to the boundary layer velocity gradient does not directly affect the spanwise dimensions of the ring.

Another feature of the flow interaction which can be observed in the trajectory is the rebound of the vortex ring away from the surface. The leading edge of the vortex ring rebounds and continues to move away from the surface. As the leading edge rises, the ring continues to stretch due to the difference in the convection velocities for each end of the ring. The trailing edge of the vortex undergoes a momentary rebound as evidenced by the loop in the trajectory and then continues to migrate closer to the surface until it dissipates.

Observation of the video sequences shows that the cause of the initial rebound is the formation of the secondary vortex ring, just as for the stationary flow case. The subsequent motion, which is different for each end of the ring and results in a further tilting of the ring, indicates that there is another type of flow interaction beyond that with the secondary vortex which is responsible for the observed behavior.

Although the following hypothesis is speculative, it seems plausible to believe that the subsequent motion of each core can be

attributed to interaction with the vorticity of the boundary layer. Figure 3.28 is a schematic diagram illustrating the vorticity of the PVR, SVR, and boundary layer vorticity. Let us assume that beyond the initial rebound caused by the SVR, its effect is small or negligible in comparison to the effect of the boundary layer vorticity. The boundary layer all around the outside of the PVR has vorticity of negative sense. The trailing core of the PVR also has vorticity of negative sense. Vortex elements with the same sense of vorticity tent to rotate around each other or "leap frog" until they coalesce. This type of behavior may be responsible for the approach of the trailing core of the PVR to the surface.

The leading core of the PVR has vorticity of positive sense, opposite to that of the boundary layer vorticity. In this case the interaction will be similar to the interaction between the PVR and SVR; each vortex element will induce a velocity upon the other. The boundary layer vorticity is of the proper sense to potentially induce a vertical velocity on the leading core of the PVR and thus cause this core to continue to rise.

Of course the preceding discussion is much too simple to adequately explain the interaction occurring between the PVR and the boundary layer vorticity. The boundary layer vorticity is properly considered only as a field or distributed vorticity and one must consider the strength of this field above, below, and on all sides of the PVR to accurately explain the interaction process. The effects of the SVR and image vortex effects caused by the surface must also be included in any explanation. Such a discussion is beyond the scope of this work and is left to further study of boundary layer flows and vortex interactions.

For the present discussion it is sufficient for the reader to realize that the lifting of the leading core away from and the approach of the trailing core to the surface are caused by the interaction of the PVR with boundary layer vorticity and result in the streamwise stretching and tilting of the primary vortex ring.

type of behavior may be responsible for the approach of the trailing core of the PVR to the surface.

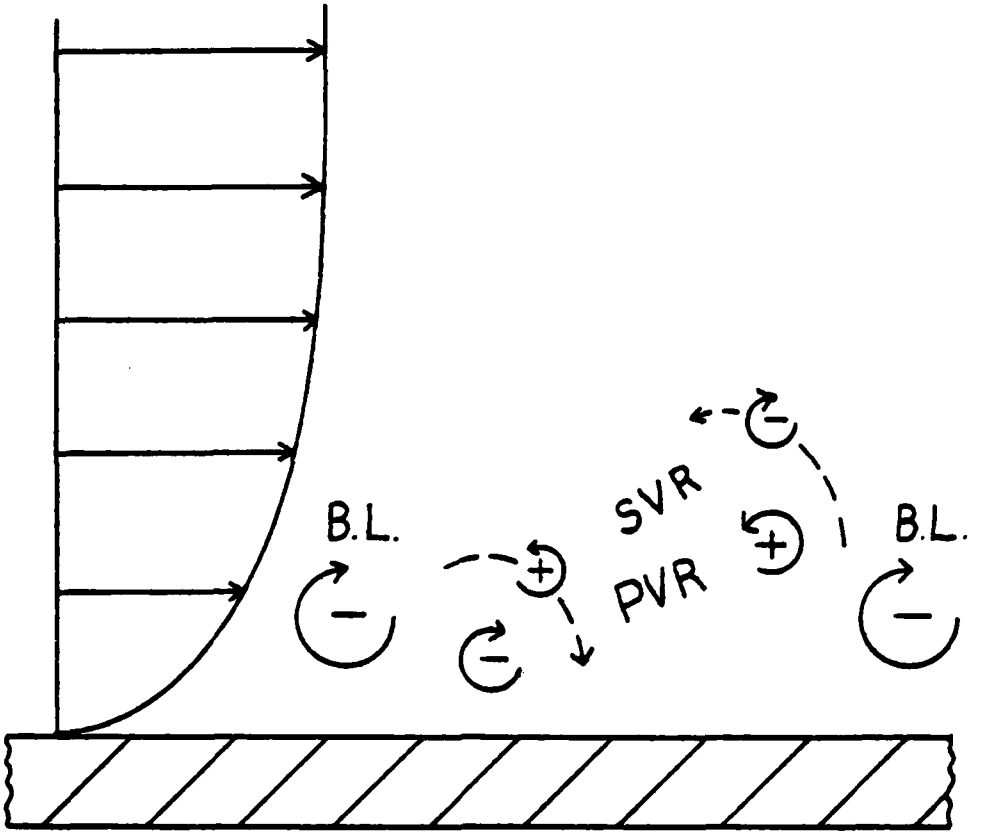

Figure 3.28 Interaction of PVR, SVR, and boundary layer vorticity

3.3.3b Flow Visualization Data

The following photographs illustrate some of the points of the preceding discussion and provide a visual description of the flow interaction phenomena.

Figure 3.29 is a side-view of a vortex ring, marked with dye, as it approaches a solid surface through a boundary layer. In the first photograph the vortex is approaching the surface at a slight angle; the edge of the surface can be seen as a faint white line in the lower fourth of the frame. Examining the sequence, one can observe a behavior with respect to the tilting of the vortex which is similar to that presented in the trajectory. The magnitude of the angle is less than that for the trajectory shown in Figure 3.27, which may be due to the difference in initial ring strength (as indicated by the Reynolds numbers) from Figure 3.27 to 3.29.

In the third photograph of the sequence, the formation of the secondary vortex ring along the trailing edge of the PVR can be observed. The SVR does not appear clearly at the front edge until two photographs later. In the sixth photograph, the SVR develops a strong azimuthal waviness, which quickly evolves into a loop structure. The ends of the loops near the rear and sides quickly orbit above the core of the PVR and into the center of the ring. The upper ends of the loops which develop near the leading edge of the PVR remain above the plane of the PVR and do not propagate into the center of the ring, probably because of the boundary layer-velocity gradient effect discussed previously. In the last three photographs, one can observe the initial formation of a tertiary vortex at the trailing edge of the PVR.

Figure 3.30 shows an oblique plan-view (looking obliquely downstream from above the surface) of an impacint vortex ring identical to that shown in Figure 3.29; again the visualization is with dye in the vortex. Initially, the diameter of the PVR increases uniformly because of the image vortex effect of the surface. (Note that vertical distances in the photographs are slightly foreshortened by the camera viewing angle.) The streamwise stretching of the vortex ring can be clearly seen in the last two photographs of the sequence.

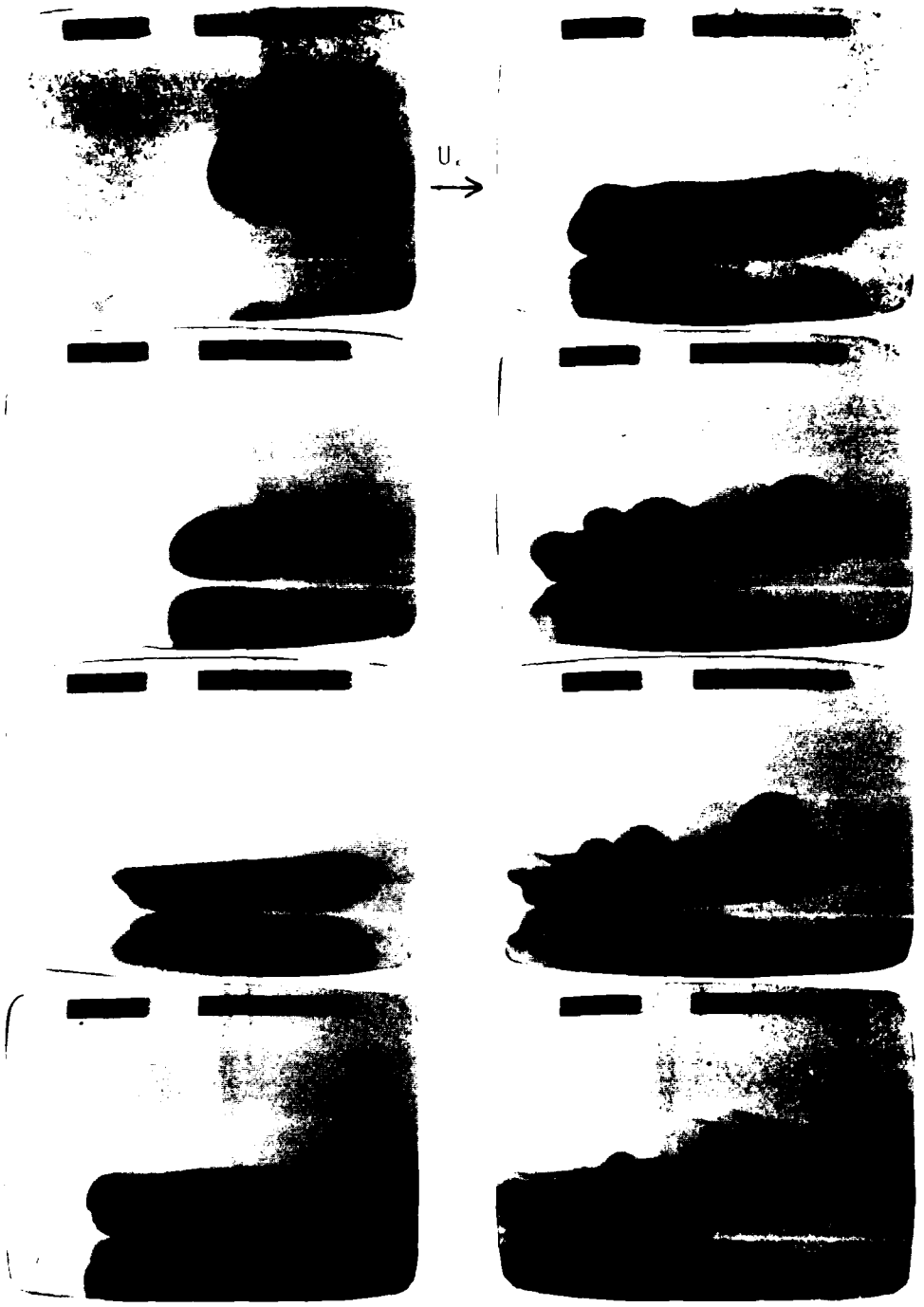

Figure 3.29 Vortex impacting a boundary layer above a solid surface (side view, dye placed in vortex). Boundary layer flow is from left to right. Frame of reference is moving at the free-stream velocity. Vortex ID.#11.728, Re_0=567. Times of pictures are 0.0, 0.1, 0.175, 0.233, 0.283, 0.367, 0.425, 0.492 sec. U_∞ = 4.1 cm/s; δ = 3.8 cm.

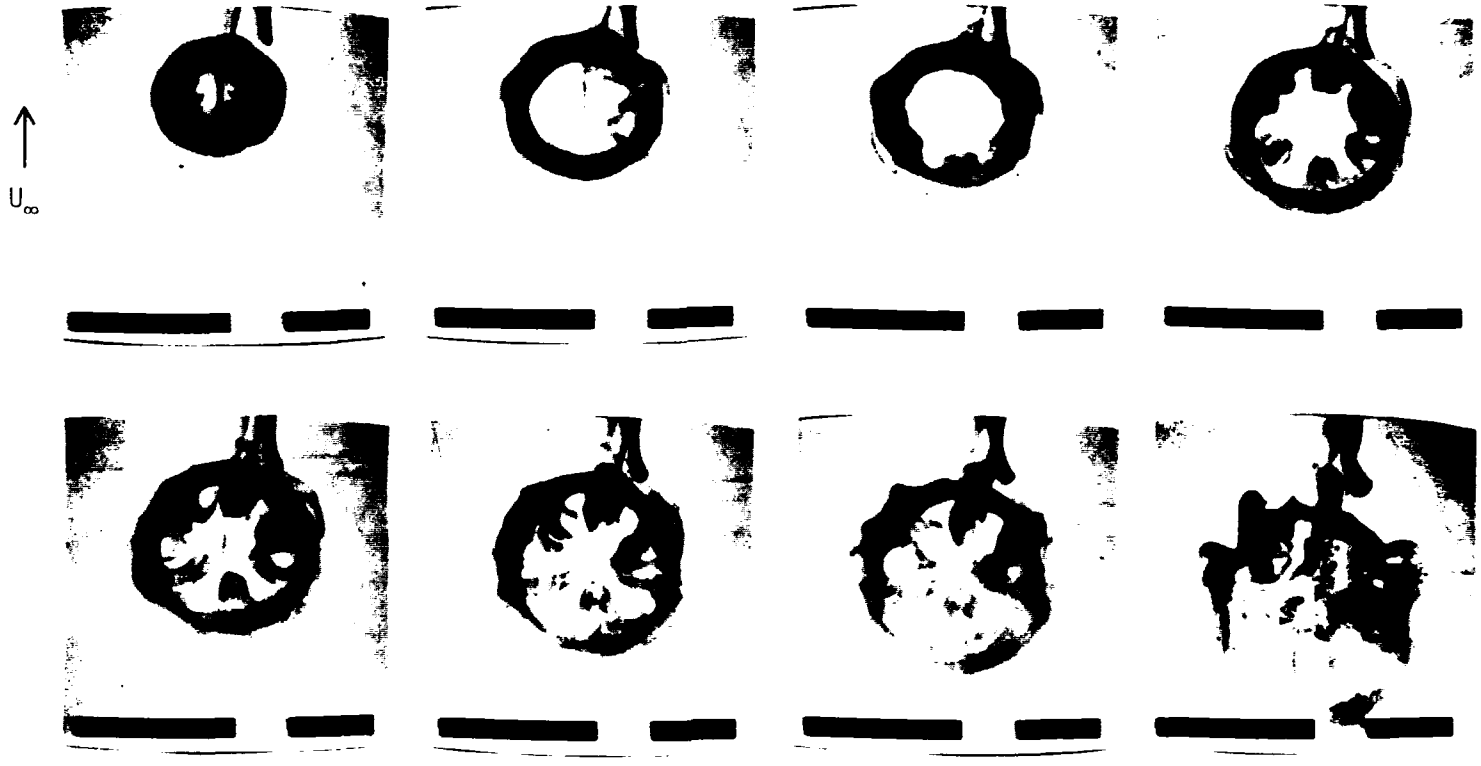

Figure 3.30 Vortex impacting a boundary layer above a solid surface (oblique plan view, dye placed in vortex). Boundary layer flow is from bottom to top in each picture. Frame of reference is moving at the freestream velocity. U_∞ = 4.1 cm./sec., δ = 3.8 cm., Vortex ID.#11.728, Re_0= 567. Times of pictures are 0.0, 0.1, 0.2, 0.308, 0.408, 0.508, 0.625, 0.933 sec.

In the fourth photograph, the SVR has developed a pronounced loop structure. The inner or lower ends of the loops are not visible in any of the photographs and presumably remain very close to the PVR or wrap around its core. The outer or upper ends of the loops propagate toward the center of the PVR; the ends of the loops from the leading edge of the ring do so to a lesser degree.

Figure 3.31 is another side-view of the interaction of a vortex ring with the boundary layer, with the interaction in this sequence visualized by placing dye in the fluid adjacent to the surface. Note that the fluid beneath the trailing edge of the PVR separates from the surface first, because 1) this end approaches the surface first due to the vortex tilting effect discussed previously and 2) the cumulative effects of boundary layer and ring vorticity are stronger at the trailing edge. The vorticity of the trailing core of the PVR has the same sign as the boundary layer flow, thus the additive effect will promote a more rapid growth and formation of a SVR. In contrast, the vorticity of the leading core of the PVR has the opposite sign of the boundary layer flow, thus the additive effect here will slow the growth of the boundary layer and retard the formation and strength of the SVR. This effect is clearly shown by the analytical work of Doligalski (15).

As the separated fluid rolls up into the SVR, one can observe in the third and fourth photographs of Figure 3.31 that the SVR orbits over the trailing core of the PVR much more quickly that it does over the leading core. This occurs not only because of the angle of the PVR (the trailing core is noticeably lower than the leading core of the PVR), but also because of the direction of the orbits with respect to the direction of the mean vorticity and velocity gradient imposed by the laminar boundary layer. Clearly, the boundary layer velocity gradient augments the orbiting of the SVR at the trailing edge of the PVR and impedes the orbiting at the leading edge of the PVR. The retardation effect at the leading edge is clearly illustrated in the fourth through seventh photographs of this sequence, where the SVR is observed to essentially stagnate in its orbit around the PVR, reaching an equilibrium

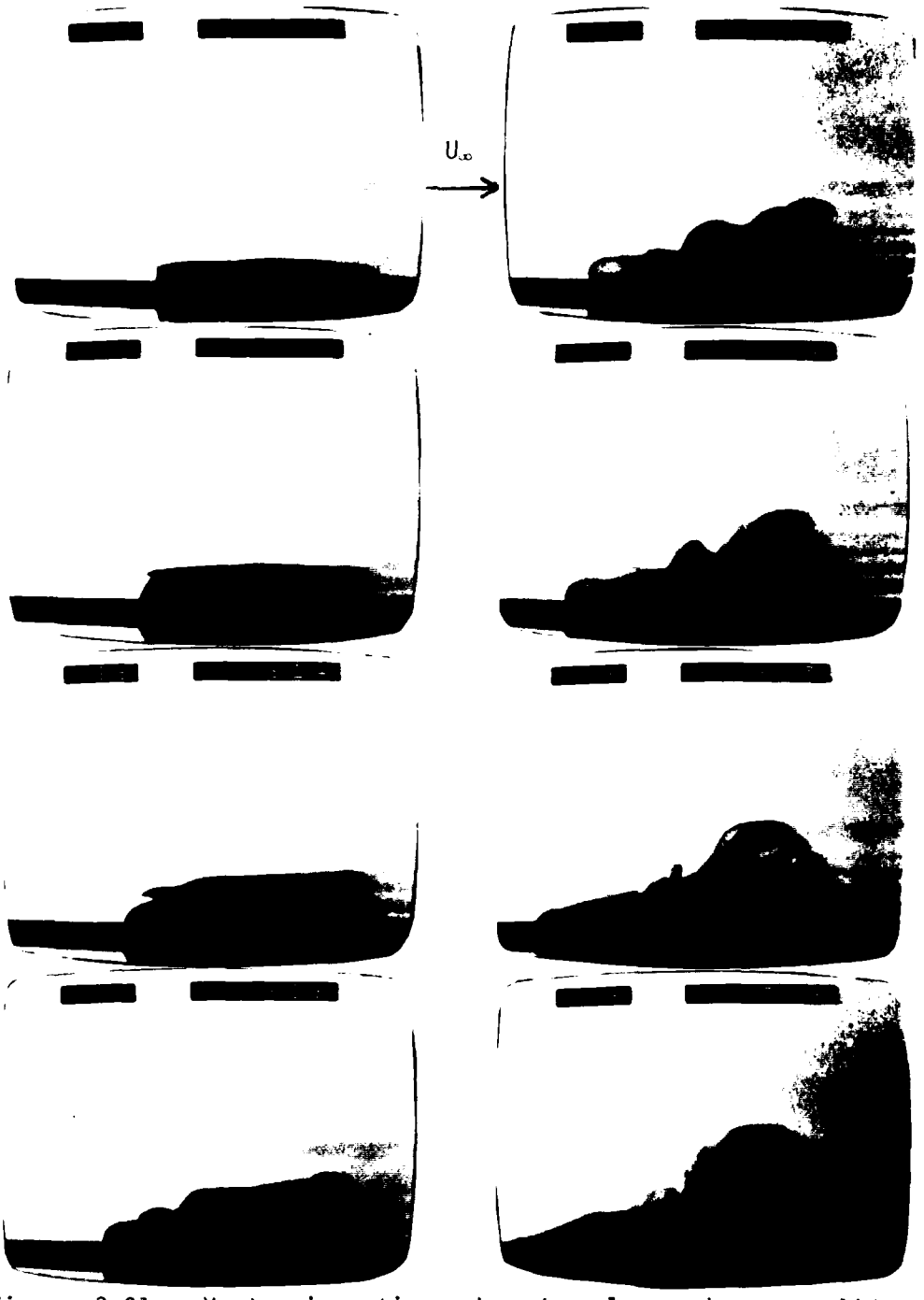

Figure 3.31 Vortex impacting a boundary layer above a solid surface (side view, dye placed on surface). Boundary layer flow is from left to right. Frame of reference is moving at the free-stream velocity. Vortex ID.#11.728, Re_0=567. Times of pictures are 0.0, 0.058, 0.125, 0.225, 0 342, 0.458, 0.633, 0.917 sec. U_∞ = 4.1 cm/s; δ = 3.8 cm.

position above the leading core of the PVR. Note that from picture six of Figure 3.31 on, the PVR, SVR, and TVR appear to almost cease further development and lose their coherency slowly by diffusive rather than convective effects. A comparison between picture six and eight (which represent a time interval equivalent to that between picture one and six) clearly illustrates this transition from vortex interaction to viscous dissipation.

3.3.3c Turbulence

It has been suggested (18) that the impact of vortex rings may be a primary mechanism for the causation of low-speed "streaks" and other wall region flow structures in the near-wall region of turbulent boundary layers. To examine this hypothesis, a series of vortex impacts with either dye in a sheet on the surface or with hydrogen bubble-line visualization were done to search for qualitative comparison between these vortex interactions and the turbulent streak structure. A series of three different representative cases from this study are presented and discussed below.

Figure 3.32 shows a plan-view of a vortex ring impacting a boundary layer as visualized by placing dye in the fluid layer adjacent to the surface (the camera is moving with the flow). The region around the impact appears to remain somewhat laminar after the impact of the vortex. The flow in the last photograph of the sequence indicates the evolution of dye concentrations, but is definitely not typical of the alternating high-speed, low-speed "streaky" pattern observed in the near-wall region of turbulent boundary layers. The dark regions are disorganized vortex filaments and not the regions of slow speed fluid normally characterized as streaks (88).

Figure 3.33 is a similar plan-view, in which the development of the secondary vortex is much more coherent. One can more clearly see the development of the SVR from azimuthal waviness, to a loop-structured SVR, and finally to disorganized vortex filaments which stretch ahead of the PVR. At first glance, these filaments may appear streak-like,

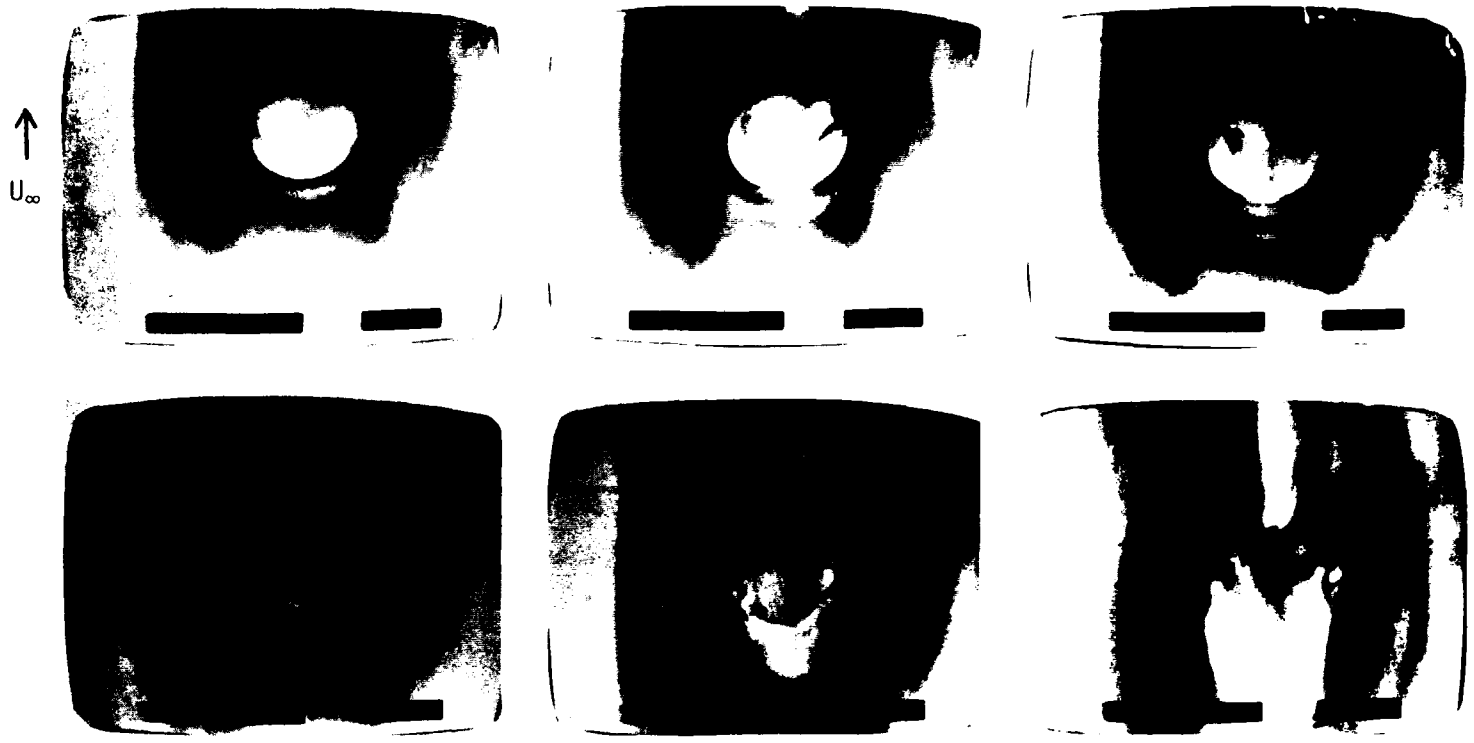

Figure 3.32 Vortex impacting a boundary layer above a solid surface (oblique plan view, dye placed on surface). Boundary layer flow is from bottom to top in each picture. Frame of reference is moving at the freestream velocity. U_∞ = 4.1 cm./sec., δ = 3.8 cm., Vortex ID.#31.323, Re_o=727. Times of pictures are 0.0, 0.267, 0.458, 0.783, 1.15, 1.82.

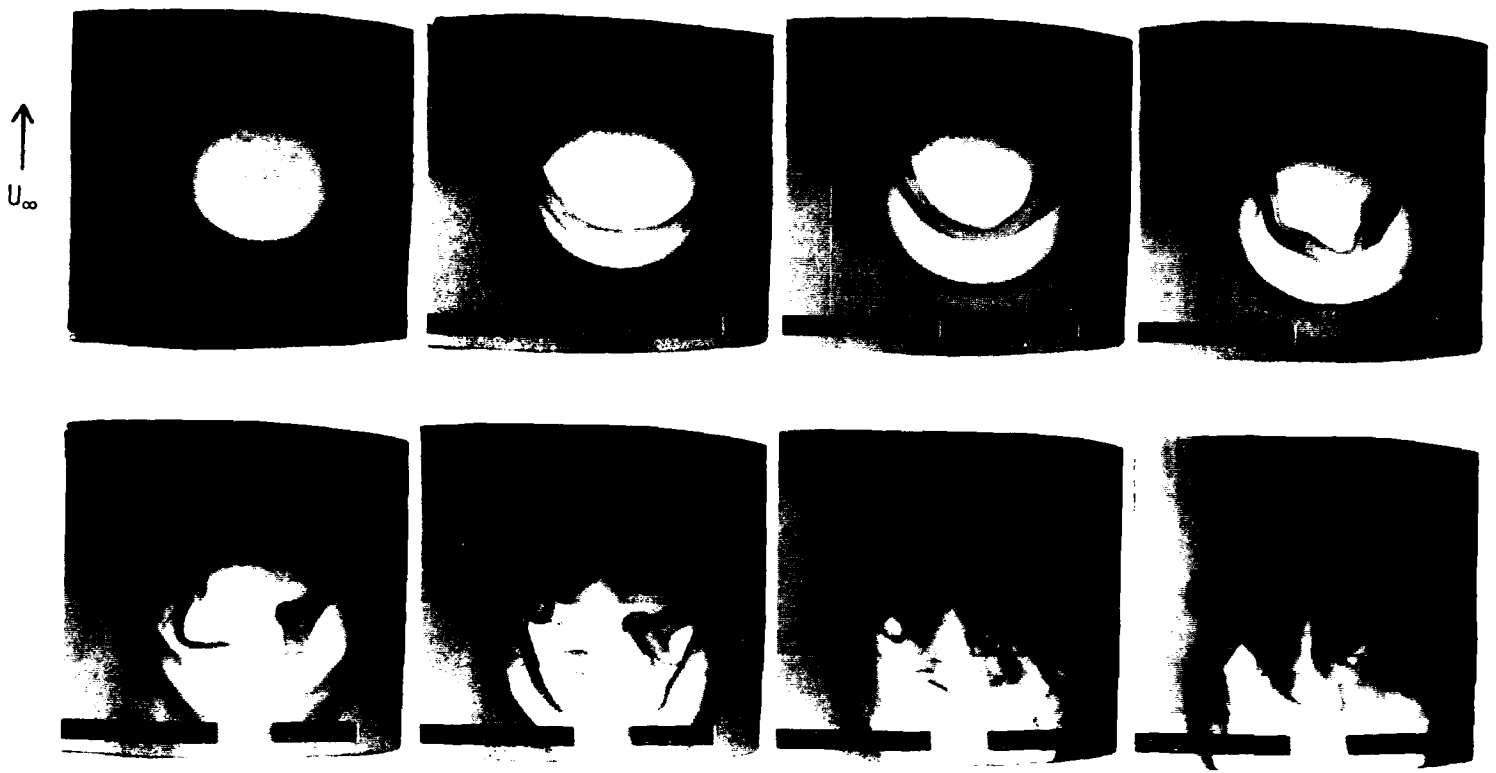

Figure 3.33 Vortex impacting a boundary layer above a solid surface (oblique plan view, dye placed on surface). Boundary layer flow is from bottom to top in each picture. Frame of reference is moving at the freestream velocity. U_∞ = 4.1 cm./sec., δ = 3.8 cm., Vortex ID.=11.728, Re_θ=567. Times of pictures are 0.0, 0.1, 0.2, 0.333, 0.492, 0.675, 0.917, 1.2 sec.

but again are not since they are formed well above the surface rather than essentially on the surface as is the observation for turbulent streak behavior (88).

Figure 3.34 is a plan-view of a vortex ring impacting a boundary layer visualized using the hydrogen bubble technique. This sequence is provided for those readers who are familiar with the visualization of turbulent boundary layer flows by this method. The flow at impact and in the region around the vortex ring appears to be laminar for quite some time. The flow in the latter part of the sequence appears to be highly three-dimensional, but no simple pattern characteristic of wall region turbulent structures appears to be present. Repeated observation of this type of visualization for vortex impacts in different phases of development relative to varied wire positions never revealed what could be construed as "characteristic" turbulence patterns (e.g. low-speed streaks) adjacent to the surface. In fact, although typical turbulent patterns often did ensue after the vortex impact, these were precipitated by the instability waves introduced by the disturbance which then broke down to yield turbulence. It was clear that the impacting vortex did not directly create turbulence type patterns, but only acted as a destabilizing influence on the boundary layer, causing a subsequent transition of the boundary layer to turbulence (which can be accomplished by any number of different types of disturbances). Thus, while the interaction of an impacting vortex ring within a laminar boundary layer is instructive with regard to vortex dynamics, it is fairly clear that such symmetric vortices are not a constituent flow structure of turbulent boundary layers.

The objective of these studies of a vortex ring impacting within a developing a boundary layer above a solid surface was to examine the resulting flow interaction, providing basic information which may prove useful in establishing the role of vortex elements within turbulent boundary layers. The flow behavior observed was in some respects similar to that observed for the stationary impact case; the diameter of the vortex ring increases rapidly in the vicinity of the surface, a secondary

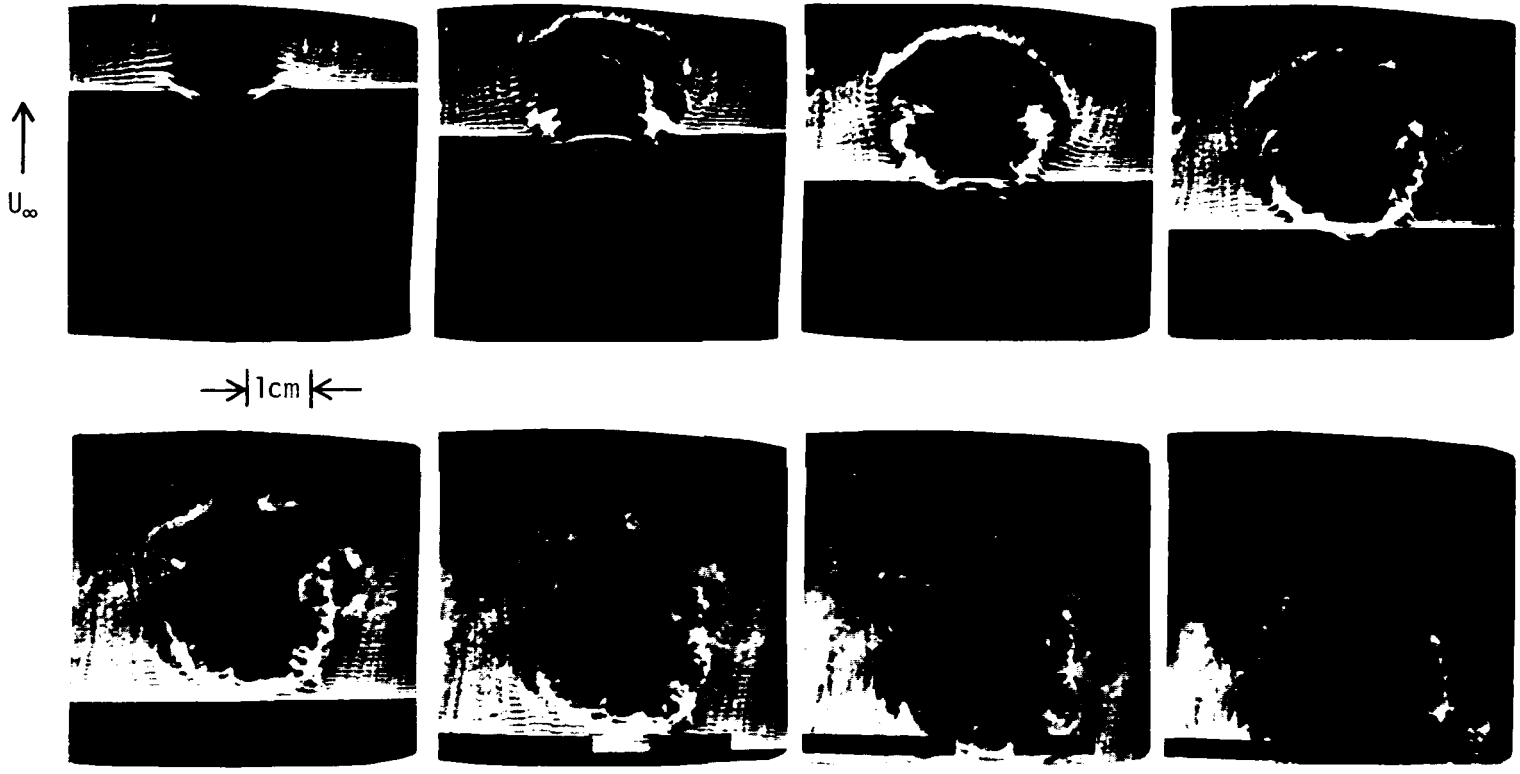

Figure 3.34 Vortex impacting a boundary layer above a solid surface visualized by a stationary bubble wire parallel to and 4 mm. above the surface (oblique plan view). Flow is from bottom to top in each picture. Frame of reference is moving at the freestream velocity. U_∞ = 4.1 cm./sec., δ = 3.8 cm., Vortex ID.#11.728, Re_D=567. Pictures are 0.25 seconds apart.

vortex if formed, and a rebound occurs in the trajectory of the vortex ring. The flow interaction, however, is complicated by the presence of the boundary layer which results in a tilting of the vortex ring which, though not completely understood, seems to be the result of the interaction with boundary layer vorticity.

As pointed out, no characteristic turbulent patterns were observed to be generated in response to the vortex ring's impact with the boundary layer. Turbulence generation at a surface is clearly not dominated by simple vortex rings impacting within a boundary layer, as has been suggested by Falco (18). However, this is not to imply that some of the dynamics which are observed during such vortex impacts are not similar to those which occur in the near-wall region of turbulent boundary layers, since turbulence depends on three-dimensional vortex stretching and interaction. Thus, it is hoped that this particular study may help provide some insight with regard to the effect that vortex elements may play in the development of a turbulent boundary layer.

CHAPTER 4: SUMMARY

When a vortex ring (PVR) impacts a solid surface, the flow interaction is marked by three features: 1) During its motion toward the surface the PVR rebounds away from the surface and may experience a reversal of its radial velocity; 2) The PVR generates at the surface secondary vorticity of opposite sign to itself, which if of sufficient strength will roll-up into a secondary vortex ring (SVR) and possibly a tertiary vortex ring (TVR); 3) The vorticity of the PVR s dispersed very rapidly in a process that appears to be chaotic, but is actually very organized. These three flow features are the result of an apparent viscid-inviscid flow interaction between the PVR and the fluid adjacent to the surface.

The initial stages of this interaction are primarily viscous in nature and result in the formation of the SVR. As the PVR approaches the surface, it induces a boundary layer flow which separates from the surface due to the adverse radial pressure gradient imposed by the presence of the PVR. If of sufficient strength, the separated boundary layer will roll-up into a SVR. Once formed, the SVR will orbit over the top of the PVR into its center, interacting in a primarily inviscid manner. After the SVR is formed, a tertiary vortex ring (TVR) may form in a manner similar to that which created the SVR, interacting with the PVR in a fashion similar to that of the SVR. The inviscid interaction of the PVR, SVR, and TVR is the mechanism which is responsible for the aforementioned first and third flow features, i.e., the rebound and reversal in the PVR trajectory and the rapid dispersal of PVR vorticity.

Contrary to the predictions of classical inviscid theory, the diameter of the PVR does not increase to infinity when it approaches the surface, rather it experiences only a finite growth in its diameter. The PVR also does not approach the surface asymptotically. The present study determined that a PVR with an Re_0 less than 600 will rebound away from the surface and a PVR with an Re_0 greater than 1300 will not only rebound away from the surface, but can also experience an intermittent

reversal of its radial velocity. This behavior is the result of an apparent Biot-Savart type interaction among the PVR, SVR, and TVR. As the three vortices interact, their relative positions change and therefore the directions of the induced velocities likewise change, creating the conditions for rebound and, depending on initial conditions, reversal of the PVR trajectory.

The interaction of the PVR, SVR, and TVR is also responsible for the ultimate dispersal of the vorticity of vortex rings with a Re_o greater than 350 (below 350 a SVR is not observed to form, with PVR vorticity apparently dispersed relatively slowly by laminar diffusion). The initial dispersal of vorticity occurs with the discrete formation of first the SVR and then the TVR. The continued dispersal of vorticity and breakdown in structure of the PVR results from the rather complex, three-dimensional, viscid-inviscid interaction of the PVR, SVR, and TVR. Because the structure of the SVR changes as the initial Re_o of the PVR increases, the nature of this interaction correspondingly changes. However, in all cases, the ultimate dispersal of vorticity is caused by vortex filaments which wrap around the core of the PVR and cause three-dimensional stretching and breakdown of the PVR.

After a SVR is formed, it orbits over the top and into the center of the PVR. As it does so, the diameter of the SVR is compressed, which destabilizes the SVR and results in the development of an azimuthal waviness in the SVR. From this point the structure of the SVR may develop along one of two paths. If the amplitude of the waves increases, the SVR may develop a loop structure. If the amplitude of the waves remains small, a kink structure will develop.

The loop structured SVR, which is observed for $470<Re_o<1600$, evolves from a ring with azimuthal waviness of relatively small amplitude into a three-dimensional vortex with azimuthally symmetric loops of large amplitude. After the SVR orbits into the center of the PVR, one end of each loop will generally migrate toward the center axis of the PVR and the other end of each loop will interact strongly with the core of the PVR. The ends of the loops which interact with the PVR are usually

the surface. When non-dimensionalized on initial PVR conditions, this time appears to remain relatively constant over the Re_o range investigated. The formation times determined experimentally compared well with similar results from a parallel numerical study by Doligalski (15) of boundary layer growth beneath an impacting vortex ring. The good agreement between his analysis and experiment is further support for the formation of the SVR being the result of an explosive boundary layer growth caused by a viscid-inviscid interaction. Unfortunately his analysis is only valid up to the point of formation of the SVR and cannot model the subsequent multiple vortex interaction.

As the SVR orbits into the center of the PVR, the SVR becomes unstable which leads to the development of an azimuthal waviness. The wavenumber of this instability was determined and plotted as a function of Re_o. An examination was done to determine whether the wavenumber of the SVR is related to an initial instability in the PVR before impact or is the result of the complex flow interaction of the PVR and the SVR. It was concluded that the resultant wavenumber appears to be a consequence of the interaction process, with the wavenumber resulting from an instability precipitated and amplified by the compression of the diameter of the SVR as it orbits the PVR.

To investigate the effect of surface conditions on the flow interaction, several experiments were performed for which vortex rings of identical initial conditions impacted solid and free surfaces. It was determined that the flow behavior in each case was very similar if not identical. In each case the impact of the vortex ring causes the formation and separation of an induced boundary layer flow which develops into a SVR. This result leads to the unanswered question of why the free surface behaves similarly to the solid surface with respect to slip. The logical explanation appears to be the effect of surface tension, but this could not be proven.

The flow interaction of a vortex ring impacting within a developing laminar boundary layer above a solid surface was also examined in an effort to provide basic information which may prove useful in establishing the role of vortex elements within turbulent boundary layers. The observed flow behavior was in some respects similar to that observed

for the stationary impact case; the diameter of the PVR increases rapidly in the vicinity of the surface, a SVR forms, and rebound occurs in the trajectory of the PVR. There are also several aspects of the flow behavior which are unique to the boundary layer case. The PVR experiences a slight tilting behavior after entering the boundary layer, with the degree of tilt increasing as the PVR approaches the surface. The leading and trailing edges of the PVR behave differently in the vicinity of the surface with the SVR developing much more rapidly at the trailing edge of the vortex ring than at the leading edge. After an initial rebound, the trailing edge of the PVR migrates closer to the surface until it dissipates; the leading edge rebounds and continues to move away from the surface. The tilting of the PVR and the difference in behavior of the leading and trailing edges can be basically attributed to a flow interaction complicated by the presence of boundary layer vorticity.

A detailed examination of the surface dye and hydrogen bubble flow visualization patterns generated by the vortex impacts within a laminar boundary layer indicated that the patterns are not consistent with turbulent structure patterns typically encountered in the wall region of turbulent boundary layers. Although the vortex ring interactions are very instructive with regard to three-dimensional vortex dynamics and the modes of vorticity dispersal of concentrated vortices, such interactions do not appear to be a dominant flow structure of the wall region of turbulent boundary layers.

BIBLIOGRAPHY

(1) Achenback, Elmar (1974). "Vortex Shedding from Spheres", J. Fluid Mech., 62, 209-221.

(2) Barker, S.J. and Crow, S.C. (1977). "The Motion of Two-Dimensional Vortex Pairs in a Ground Effect", J. Fluid Mech., 82, 659-671.

(3) Batchelor, G.K. (1965). An Introduction to Fluid Dynamics, Cambridge University Press, England.

(4) Bisgood, P.L., Maltby, R.L., and Dee, F.W. (1971). "Some Work at the Royal Aircraft Establishment on the Behavior of Vortex Wakes", Aircraft Wake Turbulence and its Detection, Olsen, J.H., Goldberg, A., and Rogers, M., eds., 171-206, New York: Plenum.

(5) Boldes, U. and Ferreri, J.C. (1973). "Behavior of Vortex Rings in the Vicinity of a Wall", Physics of Fluids, 16, 2005-2006.

(6) Brasseur, James G. and Chang, I-Dee (1981). "Combination of Kinematics with Flow Visualization to Compute Total Circulation", A.I.A.A. Journal, 19, 878-884.

(7) Cerra, A.W. and Smith, C.R. (1979). "Experimental Observations of Vortex Loop - Boundary Layer Interaction", Bull. Am. Phys. Soc., 24, 1134.

(8) Claus, Hans-Heinrich (1978). Experimentelly Untersuchung den Wechselwirkung zweier Ringwirbel mit gemeinsamer Symmetrieachse, Gottingen: Max-Planck-Institut fur Stromungsforschung.

(9) Clutter, D.W., Smith, A.M.O., and Brazier, J.F. (1961). "Techniques of Flow Visualization Using Water as the Working Medium", Aerospace Engineering, 20, January.

(10) Crow, S.C. (1970). "Stability Theory for a Pair of Trailing Vortices", A.I.A.A. Journal, 8, 2172-2179.

(11) Dee, F.S. and Nicholas, O.P. (1968). "Flight Measurements of Wing Tip Vortex Motion Near the Ground", CP 1065, Jan. British Aeronautical Research Council, London, England.

(12) Degremont Water Treatment Handbook (1979). Translation by Language Consultants France Ltd. Translation reviewed and edited by Donald F. Long, 5th ed. New York: Halsted Press Book, John Wiley and Sons.

(13) Didden, Norbert (1977). Untersuchung laminarer, instabiler Ringwirbel mittels Laser-Doppler-Anemometrie, Mitt Nr. 64, Gottingen: Max-Planck-Inst. Stromungsforschung.

(14) Didden, Norbert (1979). "On the Formation of Vortex Rings: Rolling up and Production of Circulation", Journal of Applied Math and Physics (ZAMP), 30, 102-116.

(15) Doligalski, Thomas L. (1980). "The Influence of Vortex Motion on Wall Boundary Layers", Ph.D. dissertation, Lehigh University.

(16) Doligalski, T.L., Smith, C.R., and Walker, J.D.A. (1980). "A Production Mechanism for Turbulent Boundary Layer Flows", Viscous Flow Drag Reduction, Gary Hough, editor, Progress in Astronautics and Aeronautics, 72.

(17) Falco, R.E. and Wiggert, D.C. (1980). "Effects of Dilute Polymer Solutions on Vortex Ring/Wall Interactions - A Mechanism for Drag Reduction", A.I.A.A., 275-289.

(18) Falco, R.E., (1982). "A Synthesis and Model of Turbulence Structure in the Wall Region", in Structure of Turbulence in Heat and Mass Transfer, Z.P. Zaric, ed. Hemisphere.

(19) Fohl, T. and Turner, J.S. (1975). "Colliding Vortex Rings", Physics of Fluids, 18, 433-436.

(20) Fraenkel, L.E. (1970). "On Steady Vortex Rings of Small Cross-Section in an Ideal Fluid", Proceedings of Royal Society of London Ser, A316, 29-62.

(21) Fraenkel, L.E. (1972). "Examples of Steady Vortex Rings of Small Cross-Section in an Ideal Fluid", J. Fluid Mech., 51, 119-135.

(22) Gaster, M. (1962). "A Note on the Relation Between Temporally-Increasing and Spatially-Increasing Disturbances in Hydrodynamic Stability", J. Fluid Mech., 14, 222-224.

(23) Guhler, Manfred and Sallet, Dirse W. (1979). "The Formation of Vortex Rings and Their Initial Motion", Z. Flugwiss, Weltraumoforsch., 3, 109-115.

(24) Hackett, J.E. and Theisen, J.G. (1971). "Vortex Wake Development and Aircraft Dynamics", Aircraft Wake Turbulence and its Detection, Olsen, J.H., Goldberg, A., and Rogers, M., eds., 243-263, New York: Plenum.

(25) Hama, Francis R. (1959). "Some Transition Patterns in Axisymmetric Boundary Layers", Physics of Fluids, 2, 664-667.

(26) Hama, Francis R. (1962). "Streaklines in a Perturbed Shear Flow", Physics of Fluids, 5, 644-690.

(27) Hama, Francis R., Long, James D., and Hegarty, John C. (1957). "On Transition from Laminar to Turbulent Flow", Journal of Applied Physics, 28, 388-394.

(28) Harvey, J.K. and Perry, F.J. (1971). "Flow Field Produced by Trailing Vortices in the Vicinity of the Ground", A.I.A.A. Journal, 9, 1659-1660.

(29) Head, M.R. and Bandyopadhyay, P. (1981). "New Aspects of Turbulent Boundary-Layer Structure", J. Fluid Mech., 107, 297-338.

(30) Hecht, A.M., Bilamin, A.J., and Hirsh, J.E. (1981). "Turbulent Trailing Vortices in Stratified Fluids", A.I.A.A. Journal, 19, 691-698.

(31) Helmholtz, H. (1867). "On Integrals of the Hydrodynamic Equations Which Express Vortex Motion", Trans. P.G. Tait, Philos. Mag., 33, 485-512.

(32) Hicks, W.M. (1922). "On the Mutual Threading of Vortex Rings", Proc. R. Soc. London Ser. A102, 111-131.

(33) Hooker, S.G. (1936). "On the Action of Viscosity in Increasing the Spacing Ratio of a Vortex Sheet", Proc. Roy. Soc., A154, 67-89.

(34) Huffaker, R.M., Jelalian, A.V., Keene, W.H., and Sonnenschein, C.M. (1971). "Application of Laser Doppler Systems to Vortex Measurement and Detection", in Aircraft Wake Turbulence and its Detection, Olsen, J.H., Goldberg, A. and Rogers, M., eds., 113-129, New York: Plenum.

(35) Huwahara, Kunio and Takami, Hideo (1973). "Numerical Studies of Two-Dimensional Vortex Motion by a System of Point Vortices", Journal of Physical Society Japan, 34, 247-253.

(36) Kline, S.J. and McClintock, F.A. (1953). "The Description of Uncertainties in Single Sample Experiments", Mechanical Engineering, January.

(37) Kline, S.J., Reynolds, W.C., Schraub, F.A., and Runstadler, P.W. (1967). "The Structure of Turbulent Boundary Layers", J. Fluid Mech., 30, 741.

(38) Krauch, Thomas (1980). Die Bildung eines Ringwirbels an einer kreisformigen Dusenmundung und seine Umbildung beim Ausfstieg in einer Flussigkulsschicht und an der Flussigkeitsoberflache, Gottingen: Max-Planck-Inst., Stromungsforschung.

(39) Krutzsch, C.H. (1939). "Uber eine Experimentelle Beobachtete Erscheinung an Wirbelringen bei irher Tranlatorischen Bewegung in Wirklicher Flussigkeit", Ann. Phys. 35, 497-523.

(40) Lamb, H. (1932). Hydrodynamics, 6th ed., Dover, 223.

(41) Landahl, M.T. and Widnall, S.E. (1971). "Vortex Control", in Aircraft Wake Turbulence and Its Detection, Olsen, J.H., Goldberg, A., and Rogers, M., eds., 137-152, New York: Plenum.

(42) Leonard, A. (1979). "Vortex Simulation of 3-Dimensional Spotlike Disturbances in a Laminar Boundary Layer", NASA TM 78579.

(43) Lezius, D.K. (1974). "Water Tank Study of the Decay of Trailing Vortices", A.I.A.A. Journal, 12, 1065-1071.

(44) Lighthill, M.J. (1963). Introduction to boundary layer theory in Laminar Boundary Layers, L. Rosenhead, ed. Oxford University Press.

(45) Loehrke, R.I. and Nagib, H.M. (1975). "Control of Free Stream Turbulence by Means of Honeycombs: A Balance Between Suppression and Generation", A.S.M.E., 76-FE-2.

(46) MacCready Jr., P.B. (1971). "An Assessment of Dominant Mechanisms in Vortex-Wake Decay", in Aircraft Wake Turbulence and its Detection, Olsen, J.H., Goldberg, A., Rogers, M., eds., 289-304, New York: Plenum.

(47) MaGarvey, R.H. and Bishop, R.L. (1961). "Wakes in Liquid-Liquid Systems", Physics of Fluids, 4, 800-805.

(48) MaGarvey, R.H. and Blackford, B.L. (1962). "Wake Metamorphism Behind a Sphere", Canadian Journal of Physics, 40, 1036-1040.

(49) MaGarvey, R.H. and MacLatchy, C.S. (1964). "The Formation and Structure of Vortex Rings (I)", and "The Disintegration of Vortex Rings (II)", Canadian Journal of Physics, 42, 678-689.

(50) MaGarvey, R.H. and MacLatchy, C.S. (1965). "Vortices in Sphere Wakes", Canadian Journal of Physics, 43, 1649-1656.

(51) Maxworthy, T. (1972). "The Structure and Stability of Vortex Rings", J. Fluid Mech., 51, 15-32.

(52) Maxworthy, T. (1974). "Turbulent Vortex Rings, J. Fluid Mech., 64, 227-239.

(53) Maxworthy, T. (1977). "Some Experimental Studies of Vortex Rings", J. Fluid Mech., 81, 465-495.

(54) Metzler, S.P. (1980). "Processes in the Wall Region of a Turbulent Boundary Layer", Masters Thesis, Dept. of ME/Mech, Lehigh University.

(55) Michalke, A, (1964). "On the Inviscid Instability of the Hyperbolic-Tangent Velocity Profile", J. Fluid Mech., 19, 543-556.

(56) Michalke, A. (1965). "On Spatially Growing Disturbances in an Inviscid Shear Layer", J. Fluid Mech., 23, 512-544.

(57) Miloh, T. and Shlien, D.J. (1977). "Passage of a Vortex Ring Through a Circular Aperture in an Infinite Plane", Physics of Fluids, 20, 1219-1227.

(58) Moffatt, H.K. (1969). "The Degree of Knottedness of Tangled Vortex Lines", J. Fluid Mech., 35, 117-129.

(59) Moore, D.W. and Saffman, P.C. (1971). "Structure of a Line Vortex in an Imposed Strain", in Aircraft Wake Turbulence and its Detection, Olsen, J.H., Goldberg, A., and Rogers, M., eds., 339-354, New York: Plenum.

(60) Moore, D.W. and Saffman, P.G. (1975). "The Density of Organized Vortices in a Turbulent Mixing Layer", J. Fluid Mech., 69, 465-473.

(61) Morel, T. (1976). "Design of Two-Dimensional Wind Tunnel Contractions", A.S.M.E. Publication 76-WA/FE-4.

(62) Norbury, J. (1973). "A Family of Steady Vortex Rings", J. Fluid Mech., 57, 417-431.

(63) Okabe, Jun-ichi and Inoue, Susumu (1961). "The Generation of Vortex Rings I", Reports of Research Institute for Applied Mechanics, 8, 91-101.

(64) Okabe, Jun-ichi and Inoue, Susumu (1961). "The Generation of Vortex Rings II", Reports of Research Institute for Applied Mechanics, 9, 147-161.

(65) Ornberg, Torsten. "A Note on the Flow Around Delta Wings", KTH-AERO TN 38, Royal Inst. of Technology, Sweden.

(66) Oshima, Yuko and Saburo, Asaka (1977). "Interaction of Multi-Vortex Rings", Journal of the Physical Society of Japan, 42, 1391-1395.

(67) Pao, Hsien-Ping and Kao, Timothy W. (1977). "Vortex Structure in the Wake of a Sphere", Physics of Fluids, 20, 187-191.

(68) Parks, P.C. (1971). " A New Look at the Dynamics of Vortices with Finite Cores", in Aircraft Wake Turbulence and its Detection, Olsen, J.H., Goldberg, A., and Rogers, M., eds., 355-388, New York: Plenum

(69) Perry, A.E. and Lim, T.T. (1978). "Coherent Structures in Coflowing Jets and Wakes", J. Fluid Mech., 88, 451-463.

(70) Pocklington, H.C. (1895). "The Complete System of the Periods of a Hollow Vortex Ring", Philosophical Transaction, pp. 603-617.

(71) Praturi, A.K. and Brodkey, R.S. (1978). "A Stereoscopic Visual Study of Coherent Structures in Turbulent Shear Flow", J. Fluid Mech., 80, 251-272.

(72) Pullin, D.I. (1979). "Vortex Ring Formation at Tube and Orifice Openings", Physics of Fluids, 22, 401-403.

(73) Saffman, P.G. (1971). "The Velocity of Viscous Vortex Rings", in Aircraft Wake Turbulence and its Detection, Olsen, J.H., Goldberg, A., and Rogers, M., eds., 9-10, New York: Plenum.

(74) Saffman, P.G. (1975). "On the Formation of Vortex Rings", Studies in Applied Mathematics, 54, 261-268.

(75) Saffman, P.G. (1979). "The Approach of a Vortex Pair to a Plane Surface in Inviscid Fluid", J. Fluid Mech., 92, 497-503.

(76) Saffman, P.G. and Baker, R.G. (1979). "Vortex Interactions", Annual Review of Fluid Mechanics, 11, 95-122.

(77) Sallet, D.W. (1975). "Impulsive Motion of a Circular Disk which Causes a Vortex Ring", Physics of Fluids, 18, 109-111.

(78) Sallet, D.W. and Kraemer, Kurt (1975). "On the Translational Velocity of Vortex Rings", Gottingen: Max-Planck-Inst. fur Stromungsforschung. 174-179.

(79) Sallet, D.W. and Widmayer, R.S. (1974). "An Experimental Investigation of Laminar and Turbulent Vortex Rings in Air", Z. Flugwiss., 22, 207-215.

(80) Schneider, Peter E.M. (1978). Morphologisch-phanomemologische Untersuchung der Umbildung von Ringwirbeln, die Korper anstromen, Gottingen: Max-Planck-Inst. Stromungsforschung.

(81) Schneider, Peter E.M. (1978). "Werden, Bestehen, Instabilitat, Regeneration, Vergchen eines Ringwirbels, Gottingen: Max-Planck-Inst. Stromungsforschung.

(82) Schneider, Peter E.M. (1980). Die Warmestruktur eines turbulenten Ringwirbels, Gottingen: Max-Planck-Inst. Stromungsforschung.

(83) Schneider, Peter E.M. (1980). Umbildung und Reflexion eines Ringwirbels an einer Platte, die schrag zu seiner Translationsrichtung orientiert ist, Gottingen: Max-Planck-Inst. Stromungsforschung.

(84) Schneider, Peter E.M. (1980). Experimentelle Untersuchung der Instabilitatsphasen eines laminoren Ringwirbels mit Hinblick auf vergleichbar Instabilitatsereignisse in turbulenter Scherschicht-Grenzschicht-und Hanalstromungen, Gottingen: Max-Plank-Inst. Stromungsforschung.

(85) Schneider, Peter E.M. (1980). "Sekundarwirbelbildung bei Ringwirbeln und in Freistrahlen", Z. Flugwiss. Weltraumforsch, 4, 307-318.

(86) Schraub, F.A., Kline, S.J., Henry, J. Runstadler Jr., P.W., and Littel (1965). "Use of Hydrogen Bubbles for Qualitative Determination of Time-Dependent Velocity Fields in Low-Speed Water Flows", Transactions of A.S.M.E., Journal of Basic Engineering, 87, 429-444.

(87) Schultz-Grunow, F. (1980). "Sudden Transition to Turbulence Demonstrated by Impinging Laminar Smoke Rings", Proceedings of International Symposium on Flow Visualization, Bochum, Germany, Ruhr-Universitat Bochum, Inst. Fur Thermo und Fluid-dynamik, 523-527.

(88) Smith, C.R. and Abbott, D.E. (1978). Proceedings of Workshop on Coherent Structure of Turbulent Boundary Layers, Lehigh University, November.

(89) Smith, C.R. (1981). "Flow Visualization Using High Speed Videography", Photomethods, 24, November.

(90) Smith, C.R. and Metzler, S.P. (1982). "A Visual Study of the Characteristics, Formation, and Regeneration of Turbulent Boundary Layer Streaks", Developments in Theoretical and Applied Mechanics, XI, T.J. Chung and G.R. Karr, eds., University of Alabama in Huntsville, April, 533-544.

(91) Sterns, Samuel D. (1975). Digital Signal Processing, Rochelle Park, NJ: Hayden Book Company, Inc.

(92) Sullivan, J.P., Widnall, S.E. and Ezekiel, S. (1973). "Study of Vortex Rings Using a Laser Doppler Velocimeter", A.I.A.A. Journal, 11, 1384-1389.

(93) Ting, L. (1971). "Studies in the Motion and Decay of Vortices", in Aircraft Wake Turbulence and its Detection, Olsen, J.H., Goldberg, A., and Rogers, M., eds., 11-39, New York: Plenum.

(94) Tung, C. and Ting, L. (1967). "Motion and Decay of a Vortex Ring", Physics of Fluids, 10, 901-910.

(95) Viets, H., and Sforza, P.M. (1972). "Dynamics of Bilaterally Symmetric Vortex Rings", Physics of Fluids, 15, 230-240.

(96) Walraven, A. (1970). "Energy and Motion of Vortex Rings in Liquid Helium II in the Presence of Various Plane Obstacles", Physical Review, 1, 145-157.

(97) Widnall, Sheila E. (1975). "The Structure and Dynamics of Vortex Filaments", Annual Review of Fluid Mechanics, 7, 141-165.

(98) Widnall, S.E. and Bliss, D.B. (1971). "Slender-Body Analysis of the Motion and Stability of a Vortex Filament Containing an Axial Flow", J. Fluid Mech., 50, 335-353.

(99) Widnall, S.E., Bliss, D.B., and Zalay, A. (1971). "Theoretical and Experimental Study of the Stability of a Vortex Pair", in Aircraft Wake Turbulence and its Detection, Olsen, J.H., Goldberg, A., Rogers, M., eds., 305-338, New York: Plenum.

(100) Widnall, S.E. and Sullivan, J.P. (1973). "On the Stability of Vortex Rings", Proc. R. Soc. London, Ser, A 332, 335-353.

(101) Widnall, S.E. and Tsai, Chon-Yin (1977). "The Instability of the Thin Vortex Ring of Constant Vorticity", Philosophical Trans. Royal Soc. London, 287, 273-305.

(102) Worthington, A.M. (1963). A Study of Splashes, MacMillan.

(103) Yamada, Hideo, and Matsui, Tatsuya (1980). "Visualization of Vortex Interaction Using Smoke-Wire Technique", International Symposium on Flow Visualization, Bochum Germany, Ruhr-Universitat Bochum, Inst. Fur Thermo und Fluiddynamik.

APPENDIX A: EVALUATION OF VORTEX RING CIRCULATION

A.1 INTRODUCTION

Among the parameters which characterize fully formed vortex rings are D, U_T, and Γ, which are respectively the ring diameter, translational velocity, and circulation. Many investigators including Maxworthy (53) and Didden (13) have established that these parameters are functions of the vortex generator parameters which include the diameter of the vortex ring generator orifice, D_M, the length of the ejected fluid slug, L_M, and the time history of the fluid slug velocity, $U_M(t)$. Because there exists no satisfactory theory relating to these quantities, much experimental work has been done to determine the relationships between these parameters.

There are a variety of experimental methods available to evaluate the vortex ring parameters D, U_T, and Γ. The ring diameter and translational velocity are accurately evaluated using any of the following methods: flow visualization, hot film anemometry, and laser doppler velocimetry. It is more difficult to accurately determine the circulation of a vortex ring because the velocity field associated with the vortex ring must be instantaneously evaluated.

In this appendix, a review of some of the work that has been done to establish vortex ring circulation will be presented. Evaluations of the circulation of the vortex rings examined in this study will then be presented.

A.2 REVIEW OF PREVIOUS WORK

A.2.1 An Estimate of Circulation from the Translational Velocity

Lamb (40) derived the classical Kelvin formula relating the translational velocity to the circulation of a circular vortex ring of small cross-section in a perfect fluid as

$$U_T = \frac{\Gamma}{2\pi D} (\ln(8D/d) - 1/4) \qquad (A\text{-}1)$$

The critical assumptions for this derivation are circular cores of small cross-section (i.e. $d/D << 1$ where d is the core diameter) and uniform vorticity in the core (i.e. the core rotates as a solid body).

If the translational velocity and the core and ring diameters can be determined, then an estimate for the vortex ring circulation may be established. There are two difficulties with using this method to estimate vortex ring circulation. The first difficulty occurs in determining the core diameter. It is difficult to determine accurately the core diameter using the same flow visualization techniques used to determine U_T and D. The second difficulty with this method is in the accuracy of this relation for real vortex rings, particularly when some of the assumptions used for the derivation of this relationship may not be valid. Normally, the cores of real vortex rings are not of small circular cross-sections, nor do they generally have uniform vorticity contained entirely within their cores. The accuracy of this relationship for real vortex rings will be discussed later with the results of other experimental studies.

Saffman (74) presented a relation for U_T for a vortex ring or arbitrary circulation distribution, $\Gamma(s)$, as

$$U_T = \frac{\Gamma}{2\pi D} (\ln (8D/d) - 1/2 + A) \qquad \text{(A-2)}$$

where

$$A = \int_0^{d/2} \left(\frac{\Gamma(s)}{\Gamma}\right)^2 \frac{ds}{s} \qquad \text{(A-3)}$$

and s is a streamline of radius s in the core. These relations are presented to show how the relation (A-1) will change with the assumed or actual vorticity distribution in the ring.

It thus appears that the relationship between the translational velocity and the circulation of a vortex ring is of limited utility to the experimentalist in determining the circulation of a vortex ring primarily because of the difficulty in obtaining accurate core diameter measurements.

Sallet and Widmayer (79) conducted an experimental investigation of laminar and turbulent vortex rings generated in air. Using hot wire anemometry techniques, they measured ring diameter, D, effective core diameter, d_c, and velocities of several points within the ring. The effective core diameter was defined as the distance between peaks in the measured velocity profile. The effective core circulation, Γ_c, was then calculated from the relation

$$\Gamma_c = \pi d_c (U_{MAX} - U_T) \tag{A-4}$$

One of their objectives was to verify the relationship between translational velocity and circulation. To do this, they needed to determine the total circulation of the vortex ring, which they estimated by resorting to theory. They determined that the core growth predicted by the Hamel-Oseen solution of the viscous decay of a line vortex agreed well with their measurements for laminar vortex rings. Using this solution they established that the total circulation, Γ, and the solid body core diameter, d, are given by,

$$\Gamma = \frac{\Gamma_c}{0.715} \tag{A-5}$$

and

$$d = 0.891\ d_c. \tag{A-6}$$

Relation (A-2) then becomes

$$U_T = \frac{\Gamma_c}{2(0.715)\pi D}\ \left[\ln\left(\frac{8D}{0.891 d_c}\right) - 1/2 + A\right] \tag{A-7}$$

From their data and relation (A-7), they determined that a value of ln(2) for the constant, A-1/2, gave good agreement between their predicted and measured translational velocities.

A.2.2 Direct Measurement of Circulation and Vorticity

A.2.2a Sullivan, Widnall, and Ezekiel

Sullivan, Widnall, and Ezekiel (92) measured the axial and radial velocity distribution in a vortex ring with a two-component laser Doppler velocimeter. The vortex ring was generated in air and had a Reynolds number ($Re = \Gamma/\nu$) of 7780 and a d/D of 0.27, indicating that this vortex ring had a fat rather than a thin core. They were able to determine the circulation by two methods: in the first they calculated Γ from the line integral of the velocity for a path around and far outside of the core of the ring; in the second they calculated Γ from the vorticity distribution within the ring. (The vorticity was rather concentrated with roughly 85% of the vorticity within the $\psi/(D/2)^2 U_T = 0.4$ streamline.) These two circulation calculations gave results which were within 3.4% of each other.

From their measurements, they determined that neither Hill's spherical vortex model, where vorticity is distributed throughout a sphere, nor a model using a small core in solid body rotation properly described the vorticity distribution in their experimentally produced vortex ring. By numerically integrating their vorticity distribution, they established a value for A in relation (A-2) of 0.136. This yields an A-1/2 value of -0.364, in sharp contrast with Sallet and Widmayer's (79) value of ln(2).

A.2.2b Maxworthy

Maxworthy (53) performed a series of experiments with vortex rings generated in water with Reynolds numbers (Re_M) ranging from 10,000 to 100,000. Among other quantities, he determined the circulation of the rings using a one-component laser Doppler velocimeter. He determined that although the vorticity distribution was peaked in the center of the core, significant vorticity was contained in the fluid outside of the core. Only 50% of the circulation was contained within the core of the ring, which is much less than indicated in the work of Sallet and Widmayer (79) and Sullivan et al. (92).

Maxworthy also compared the measured circulation, Γ, to an estimate of the initial circulation, Γ_s, based on the vorticity present at the orifice during formation of the ring. From a simple "slug" model and the ejected slug nozzle velocity (determined from the vortex generator piston displacement curve, as measured with a displacement transducer), Γ_s was estimated from the relation

$$\Gamma_s = \frac{1}{2} \int_0^L U_M dL_m \quad . \tag{A-8}$$

He determined that Γ_s was approximately equal to Γ. Generally, one would expect Γ_s to be greater than Γ by the amount of negative vorticity which is created at the outside wall of the nozzle and is ingested into the vortex ring, cancelling some of the positive vorticity present in the ring. This negative vorticity was observed and reported by Maxworthy (51) in some flow visualization experiments. Since the amount of negative vorticity was not measured, he could not comment quantitatively on the expected difference between the estimated circulation, Γ_s, and the actual measured circulation, Γ. In addition the "slug" model is very simple and does not properly model the roll-up process that occurs at the nozzle exit. The usefulness of the estimated Γ_s is as a simple reference value with which the actual measured value can be compared.

A.2.2c Didden

In 1977 Didden (13) published a report at the Max Planck-Institut fur Stromungsforschung in which he comprehensively investigated laminar vortex rings using both flow visualization and laser Doppler anemometry techniques. Only his results with respect to circulation will be discussed here. These comments should not be considered a complete representation of his work because of the limited translation we have of the original German text.

The circulation, Γ, was measured with a laser Doppler velocimeter at a point three orifice diameters downstream from the orifice. This measurement was then compared to the "slug" estimate of circulation, Γ_s, by the relation

$$\Gamma_s = \frac{1}{2} \int_0^T U_M^2 \, (t)dt \ , \qquad \text{(A-9)}$$

which, by assuming constant velocity across the nozzle exit plane, reduces to

$$\Gamma_s = \frac{1}{2} U_M \, L_M \ . \qquad \text{(A-10)}$$

Comparing Γ with Γ_s, he found that Γ was generally 30% to 60% greater than Γ_s. Again, the effects of the negative vorticity generated at the orifice are not included in Γ_s. In this case Γ_s underestimates the actual vorticity generated at the orifice even more than it did in Maxworthy's study (53). One difference between the two studies is the difference in the Reynolds numbers of the vortices; in this study the Reynolds number, Re_o, is much lower, ranging from 650 to 6600.

Didden (14) published the results of another study in 1979 in which he attempted to determine the vortex circulation from the flow conditions at the nozzle. Using a laser Doppler velocimeter he measured the unsteady velocity field in the nozzle exit plane during the vortex formation process. From these measurements, the circulation of vortical fluid convected through the nozzle exit plane was evaluated. This work is perhaps the first attempt to directly measure all flows contributing to the initial circulation of the vortex ring, including the boundary layer of negative vorticity, which is produced at the outer wall of the nozzle and convected into the vortex ring.

In addition to calculating the circulation in the region X>0 (X is the downstream distance from the nozzle exit plane), created by convective transport of vorticity through the plane X = 0 during the piston displacement, Didden also determined the circulation of the ring at

a position $X = 3D_M$. Many detailed results are presented including plotted distributions of velocity, vorticity, and vorticity flux. The following comments will be made regarding a plot he presents of dimensionless circulation $\hat{\Gamma} = \Gamma/U_M D_M$ versus L_M/D_M.

The positive circulation, produced by the boundary layer at the inner wall of the nozzle, $\hat{\Gamma}_i$, was greater than the circulation measured at $X = 3\ D_M$, $\hat{\Gamma}_W$. Didden speculates that the deviation is probably the result of an inability to exactly determine the vorticity flux, $d\Gamma_i/dt$, during the initial start-up period of the piston, since it is sensitive to the interpolation of the velocity near the wall. He also plots an estimate of circulation established by assuming a constant velocity across the nozzle exit plane as was assumed in his earlier work, and shows that it is much less than both $\hat{\Gamma}_W$ and $\hat{\Gamma}$. A significant result of this work is that the negative circulation produced at the outer wall is a significant and measurable amount; at one point in the early development of the ring the negative circulation, Γ_a, is as much as 25% of Γ_i.

In conclusion, he presents the following three effects which are not accounted for in the simplified "slug" flow model:

(i) The starting flow around the nozzle edge produces a large flow velocity $u > U_M$ near the edge, causing a large vorticity flux into the vortex ring, especially at small t.

(ii) At larger t, the maximum velocity u_i in the exit cross-section remains larger than U_M because of the displacement effect of the boundary layer.

(iii) The net vorticity flux into the vortex ring is considerably diminished by the negative vorticity of the external boundary layer, which is produced by the flow of the rolling-up vortex at the outside nozzle wall. (14)

Didden's last study (14) appears to be the best description to date of the production of circulation in vortex rings generated from a nozzle. He has shown that the circulation of a vortex ring can be accurately determined from a detailed measurement of the flow velocities at the nozzle during the formation of the vortex ring.

A.2.3 Measurement of Circulation with Flow Visualization Techniques

A.2.3a The Bubble Line Method

The bubble line method consists of using the hydrogen bubble technique to measure the velocity along a closed path around the core. According to the assumptions of classical theory, all the vorticity is contained within the core of the ring, which is rotating in solid body rotation; the region outside the core is irrotational. To determine the circulation one must measure the rotational velocity $\dot{\theta}$ along a closed path at the edge of or outside of the core. The expression for circulation then becomes

$$\Gamma = \pi d^2 \dot{\theta}/2 \qquad \text{(A-11)}$$

where d and $\dot{\theta}$ are the diameter and rotational velocity at the point of measurement with respect to the center of the core.

The method seems simple enough to use, but the present authors know of no work where it has been employed successfully, if at all. Maxworthy (51) used the hydrogen bubble technique to visualize vortex rings, but he made no reports of any circulation measurements using this method. He did make some qualitative comments concerning the vorticity of the vortices; presumably these comments may have been based on observations of experiments for which this method was used.

This method was one of those used to determine circulation in the present study. Results of these experiments will be reported in a following section.

A.2.3b A Combination of Kinematics and Flow Visualization

Brasseur and Chang (6) describe a method in which simple flow visualization measurements are combined with relationships derived from kinematic properties of a vortical flow field using potential flow theory to compute the total circulation of a vortex ring. Using simple flow visualization data, they were able to determine the change in the circulation of a fully developed vortex ring as it evolved.

This is a powerful method because it can easily determine the circulation at multiple points in the trajectory of a ring from a single data realization. Other techniques, such as those using an L.D.V. require multiple data realizations.

The method will be discussed in general terms below; the reader who is interested in the details may refer to their published work (6). The Biot-Savart law as reported by Batchelor (3) kinematically relates the velocity field to the vorticity field at each instant in time. Assuming the vorticity is sufficiently concentrated in the core, the vortex ring can be modelled as a filament of strength Γ and the flow field can be calculated using a much simpler relation:

$$\phi(x) = \iint_A \frac{\partial}{\partial n} \left(\frac{\Gamma}{4\pi r}\right) dA(\rho) + \phi_i(x) \qquad \text{(A-12)}$$

where A is the surface bounded by the filament, n is the outward normal to that surface, $r = x-\rho$ where ρ is the point at which the vorticity exists, and ϕ_i is the potential field induced by the presence of boundaries and must satisfy Laplace's equation. Thus, there exists a kinematic relationship between the potential flow field and the strength and geometry of the vortex. From knowledge of the potential flow field and the geometry of the vortex ring, the total circulation can be calculated. The necessary knowledge of the flow field and geometry of the ring is obtained from the flow visualization experiments in the form of U_T and T/R' where U_T is the translational velocity, T is the half thickness of the bubble of fluid moving with the ring, and R' is the radius to the outer edge of this bubble of fluid. Using the kinematic relationships, a/R is determined as a function of T/R'. Relationship (A-13), which is a modified form of the Kelvin/Lamb formula, is used in the determination of the circulation of the ring.

$$\frac{U_T}{\Gamma/4\pi R} = \ln (8R/a) - 1/3 \qquad \text{(A-13)}$$

Brasseur and Chang used this method to compute the circulation and its variation with time for vortex rings over a range from Re_o = 690 to 50,100 as they propagated through a fluid filled tube. To check this method, they computed an estimate of the circulation, Γ_s, using a simple slug theory and compared this value to the circulation computed using their method. The estimate of circulation, Γ_s, is given by relations A-14 and A-15

$$\Gamma_s = C\int_0^L U(z)dz \qquad \text{(A-14)}$$

where

$$C = \frac{\text{vortex ring bubble volume}}{\text{ejected fluid volume}} \quad . \qquad \text{(A-15)}$$

They reported excellent agreement between the values of circulation obtained using their method and Γ_s. This result should be compared to similar results of Maxworthy (53) and Didden (13). Maxworthy, who examined vortex rings in an Re_o range of 10,000 to 100,000, also found that Γ_s was very close to measured values of circulation using an L.D.V. Didden, who examined rings in an Re_o range of 650 to 6600, found that the measured value of Γ was 30% to 60% greater than the value of Γ_s. There is a difference in how Γ_s was computed for these cases. Maxworthy and Didden use a factor of 1/2 in place of C. Didden does show the origin of the factor of 1/2, although Maxworthy does not. Brasseur and Chang fail to report any of their C values so no meaningful comparisons can be made amongst these studies.

Questions regarding the accuracy of this method also arise concerning the two critical assumptions used in their analysis: (1) that the vorticity is sufficiently concentrated such that the finite extent of the core can be neglected, and (2) that the circulation in the wake is such a small fraction of the total circulation that it can be ignored. The first hypothesis was tested by computing the potential fields for two vortices: the first had the assumed concentrated vorticity, the second had vortex filaments distributed over the core of the vortex.

The differences between the calculated potential fields were extremely small with virtually no difference in T and R' values. The second hypothesis was tested by allowing vortex filaments to exist in the wake region of the vortex ring, calculating the potential field for the ring, and comparing it to that obtained for a ring with no vorticity in the wake. The difference in T was found to be only 3%, well within the precision of their measurements.

From these results Brasseur and Chang concluded that a vortex filament model is satisfactory for computing the size and shape of the vortex bubble. They do expect, however, that inaccuracies due to finite noncircular cores and wake vorticity will become significant at very low Reynolds numbers when vorticity is diffused over a large volume and not strongly peaked.

The authors acknowledge that to fully assess the accuracy of their method, calculations of circulation using their method should be directly compared to independent measurements of circulation such as those obtained using a laser Doppler velocimeter. In this regard they were able to compare only one independent measurement of circulation using an L.D.V., that of Sullivan et al. (92). The agreement for this one data point appeared excellent, falling within 1%.

In conclusion, the method of Brasseur and Chang appears to be a very powerful and attractive method, particularly because of the ease with which flow visualization techniques may be employed. However, a good check of its accuracy for a variety of cases using an independent method, such as measurement of circulation with a laser Doppler velocimeter, remains to be performed.

A.3 RESULTS OF CIRCULATION MEASUREMENTS

A.3.1 Review of Methods Used

In the present study, three different methods were used to determine the circulation of the vortex rings: (1) the hydrogen bubble-line method, (2) the estimate of circulation in the ejected fluid slug, and (3) the method of Brasseur and Chang (3).

The bubble line method consisted of using a hydrogen bubble wire to generate a line or lines of bubbles which mark the flow in the vortex ring as it propagates by the bubble wire. The necessary data could best be obtained when the center of the core of the vortex ring exactly coincided with the bubble wire at the instant a line of bubbles was generated. If this occurred, the initial deformation of the bubble line would show a velocity profile across the core with velocity peaks indicating the edges of the core. One of the problems with this method is that such an exact coincidence of a bubble line with the vortex core occurred very infrequently. Because it could not be repeated with any degree of regularity, many realizations were required to obtain a few "good" (relatively speaking) data points.

To determine the circulation, Γ_B, using this method, the diameter and rotational velocity, obtained from the flow visualization and measured with respect to the center of the core, were used with relation A-11. Because the center of the core is translating with respect to the field of view, it is difficult to properly determine the data if the center is poorly marked by the bubbles.

The second method used was to estimate the vortex ring circulation derived from a simple slug model of the fluid ejected from the orifice. The circulation Γ_M was determined using relation A-16 as discussed in Maxworthy (53) and Didden (13).

$$\Gamma_M = \frac{1}{2}\int_0^T U_M^2(t)dt \qquad \text{(A-16)}$$

$U_M(t)$ is the mean velocity of the fluid ejected from the orifice as determined from the velocity of the piston and the area ratio of the piston and orifice. The velocity of the piston was determined from the time history of a displacement transducer attached to the piston. Relation A-16 was then numerically evaluated to determine the circulation Γ_M.

The third method used was that of Brasseur and Chang (6). From the flow visualization the following data was obtained: the

translational velocity, U_T, the radius of the ring, R, the half thickness, T, and the outer radius of the dyed bubble of fluid moving with the vortex ring, R', as previously defined. Data giving a/R as a function of T/R' for a vortex ring in an unbounded fluid is shown in Table A-1, as obtained from a figure in Brasseur and Chang (6). a/R is the ratio of core radius to ring radius.

Table A-1. T/R' vs a/R

Obtained from Brasseur and Chang (6)

T/R'	a/R
0.338	0.04
0.412	0.07
0.452	0.10
0.48	0.13
0.505	0.16
0.525	0.19
0.542	0.22
0.558	0.25
0.57	0.28
0.585	0.31
0.595	0.34
0.635	0.49

The a/R for a given ring was estimated from the measured T/R' and the data in Table A-1. The circulation Γ_{BC} was then calculated using the U_T, R, and a/R data, in conjunction with relation A-13 (the modified Kelvin/Lamb formula used by Brasseur and Chang (6)) which is repeated here in rearranged form as A-17.

$$\Gamma_{BC} = \frac{4\pi R\ U_T}{\ln(\frac{8}{a/R}) - \frac{1}{3}} \qquad \text{(A-17)}$$

A.3.2 Comparison of Three Methods of Circulation Calculation

Table A-2 shows the values of circulation computed using each of the three methods for four vortex ring cases. The bubble method

was used in only four cases because of the aforementioned difficulties in obtaining useable data.

Table A-2. Comparison of Three Methods of Circulation Calculation

Vortex Ring No.	Γ_B cm^2/S	Γ_M cm^2/S	Γ_{BC} cm^2/S
21.635	7.74	13.3	15.4
31.340	11.2	27.4	18.1
42.825	4.71	8.06	8.12
51.245	5.82	6.32	9.84

The data indicates a wide variation in the circulation calculated using the three methods. Γ_B ranges from 58% to 92% of Γ_M and Γ_{BC} ranges from 66% to 156% of Γ_M.

There are at least three sources of error in the bubble method calculation besides the normal measurement error. The first possible source is that the bubble velocity may not be the same as the fluid velocity. No attempt has been made to evaluate this error, but it is believed to be small based on the results of Schraub et al. (86). A second source of error is the existence of vorticity to the outer edge of the fluid moving with the vortex ring. As Maxworthy (53) reported, 50% of the vorticity is within the core, with vorticity existing out to the edge of the vortex bubble volume. To eliminate this error, the data measurement would have to be taken at the outer edge of the vortex bubble volume. The third source of error is due to the difficulty in determining the exact center of the core, as already mentioned.

Because of the difficulties associated with the data measurements, the necessity to rearrange equipment and lighting when changing from dye visualization to hydrogen bubble visualization, and the variation in the data, it was not considered practical to determine the circulation using the bubble method for each vortex case studied.

Because of the large variation between Γ_{BC} and Γ_M and the small data population, it was decided to investigate the relation between Γ_{BC}

and Γ_M for a much larger data population. Γ_{BC} and Γ_M were calculated for each vortex case studied; the ratio Γ_{BC}/Γ_M was then plotted in Figure A.1 as a function of L_M/D_M. The results were somewhat surprising in that the large variation persisted. Just about all the data points were in a range of 0.8 to 2.0 with an average value of 1.44. This data contrasts sharply with the excellent agreement reported by Brasseur and Chang. It is not expected that such a large variation in the data can be due to the difference in relations for Γ_M where they used a factor, C, defined in A-15 instead of the factor 1/2 used in A-16. What is surprising is the agreement with Didden's research (13), where he determined Γ_{LDV}/Γ_M to vary from 1.3 to 1.6 (Γ_{LDV} is the circulation of the vortex ring measured with an L.D.V.). Note that the average of 1.3 and 1.6 is 1.45 which is very close to the average of 1.44 reported here.

One source of error in the Γ_{BC} measurements is the T measurement. In the wake region there often was no sharp interface delineating the dyed region of the vortex ring. This alone could cause as much as $\pm$10% error. Another possible source of error in the Brasseur and Chang method is in the accuracy of the method itself for the range of Reynolds number (Re_o) investigated here, 105 to 4940. Brasseur and Chang report that they expect that inaccuracies due to finite noncircular cores and wake vorticity may become significant at very low Reynolds numbers when vorticity is diffused over a large volume and not highly peaked.

It is difficult to adequately evaluate this data without a better, independent estimate of the circulation in the vortex as might be obtained using a L.D.V. The data presented here must therefore be regarded as somewhat inconclusive in regard to the accuracy of the Brasseur and Chang method for determining circulation.

Likewise Γ_M has not been proven to be a reliable estimate of the circulation in a vortex ring. The studies by Maxworthy (53) and Didden (13) seem to indicate that as Re_o decreases, Γ_M worsens as an estimate of the circulation in a vortex ring, underestimating the actual circulation by as much as 60% in Didden's study.

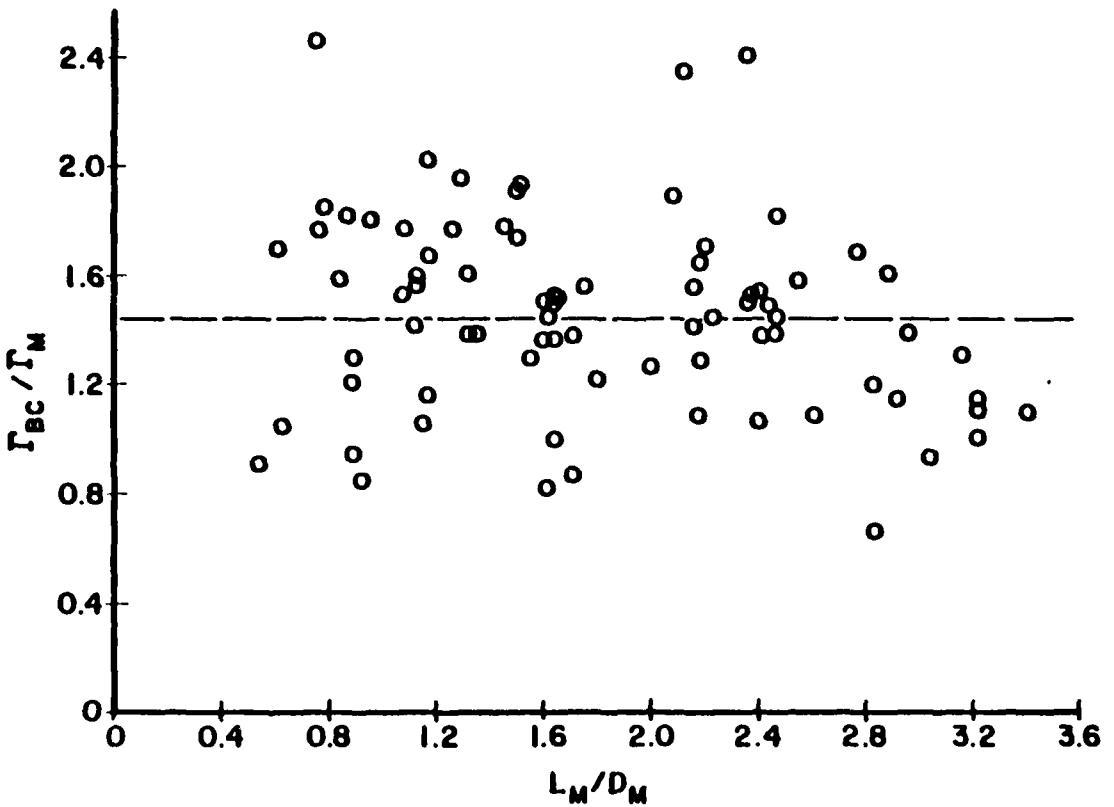

Figure A.1 Plot of Γ_{BC}/Γ_M vs L_M/D_M. Γ_{BC}: Circulation determined using the method of Brasseur and Chang (6). Γ_M: Estimate of circulation of fluid slug ejected from orifice.

It appears that the most accurate method for measurement of the circulation of a vortex ring is the use of LDV velocity measurements. Brasseur and Chang's method offers the promise of a very simple and accurate method, but its accuracy remains to be established by an accurate independent method over a range of vortex Reynolds numbers.

APPENDIX B: UNCERTAINTY ANALYSIS OF RESULTS

B.1 ESTIMATES OF ERRORS: UNCERTAINTIES

Errors, i.e. the difference between the measured value and the "true" value of an experimentally determined quantity, arise from finite sample sizes and inaccuracies in the experimental techniques used.

The best measure of an experimental quantity is obtained by making many measurements using many different experimental techniques. To the extent that the sample size and number of experimental methods are limited, there exists the possibility of error in the value of the quantity being measured. The error in a quantity determined from a limited sample size can be estimated using statistical methods. Unfortunately, in this as in many engineering experiments, the sample size may be very limited. In these experiments for a given experimental realization, generally only one and at most three measurements were made. Because the sample sizes are so small, the error will not be determined using statistical methods of standard deviations and means, but instead will be estimated using uncertainty analysis methods for single sample observations.

The total uncertainty, W_R, in an experimental result, $R = R(V_1, V_2,\ldots,V_N)$ may be calculated using relation B-1 (36):

$$W_R = \left[\left(\frac{\partial R}{\partial V_1} W_1\right)^2 + \left(\frac{\partial R}{\partial V_2} W_2\right)^2 \ldots\ldots \left(\frac{\partial R}{\partial V_N} W_N\right)^2\right]^{\frac{1}{2}} \qquad \text{(B-1)}$$

where $W_1, W_2,\ldots W_N$ are the uncertainty intervals in variables $V_1, V_2,\ldots V_N$ for a certain estimated level of confidence, generally 95%. $V_1, V_2,\ldots V_N$ must be independent and their statistical distributions must have only a single peak. If $V_1, V_2,\ldots V_N$ are normally distributed the expression is exact.

B.2 UNCERTAINTY IN EXPERIMENTAL RESULTS

B.2.1 Calibration Uncertainty

Generally, all results are based on length and time measurements of flow phenomena for selected frames of data from a video sequence. Measurements were taken directly from hard copy prints of the desired data frames. The prints were obtained using a videographic printer, which employs a latent image process with heat developed dry silver paper and interfaces directly with the video recorder.

Because the resulting images are larger than their actual size, a calibration must be used for any length measurement. The uncertainty in length calibration, C_L, is

$$\frac{W_{C_L}}{C_L} = \pm 1.4\% \text{ (95\% confidence)}$$

Time measurements are based on the displayed frame numbers and the framing rate of the video recorder, 120 frames per second. The error in the framing rate was assumed to be negligible, since the effective shutter speed for each frame was less than 1/10,000 second.

The uncertainties for the following measurements are for a typical vortex ring case #52.235 which had a D_o of 3.05 cm, a V_o of 6.65 cm/s, Re_o of 2140, T_s of 1.4 and Γ_{BC} of 44.2 cm^2/s, except where specified otherwise.

B.2.2 Uncertainty in Ring Diameter D_o

The uncertainty in D_o includes the expected uncertainty in any measurement of this type as well as the uncertainty due to the subjective determination by the observer of the location of the center of the vortex ring core. The uncertainty is calculated for a horizontal core center location error of .14 cm for each core on a diameter of 3.05 cm as shown below. The calibration error is also included.

$$\frac{W_{D_o}}{D_o} = \left[2\left(\frac{\partial D_o}{\partial d} \cdot \frac{Wd}{d}\right)^2 + \left(\frac{\partial D_o}{\partial C_L} \cdot \frac{W_{C_L}}{C_L}\right)^2\right]^{\frac{1}{2}}$$

$$= \left[2(.14/3.05)^2 + (.014)^2\right]^{\frac{1}{2}} = \pm 6.6\% \text{ (95\% confidence)}$$

This uncertainty is generally valid for all vortex ring cases since the zoom lens feature of the video system allowed each vortex ring to be magnitied to approximately the same image size on the video screen.

B.2.3 Uncertainty in Translational Velocity V_o

The uncertainty in the translational velocity V_o can be calculated as shown in B-2 from the uncertainties in the calibration, the distance traveled, and the measured time. (The uncertainty in the time is assumed to be zero.)

$$\frac{W_{V_o}}{V_o} = \left[\left(W_{C_L}/C_L\right)^2 + \left(W_L/L\right)^2 + \left(W_T/T\right)^2\right]^{\frac{1}{2}} \qquad \text{(B-2)}$$

The uncertainty in the distance travelled (W_L/L) is due to the uncertainty in determining the vertical location of the center of the vortex ring cores at two locations, estimated to be .23 cm at each location. W_L/L is calculated in B-3.

$$\frac{W_L}{L} = \left[\left(\left(\delta l_1/l_1\right)\left(l_1/L\right)\right)^2 + \left(\left(\delta l_2/l_2\right)\left(l_2/L\right)\right)^2\right]^{\frac{1}{2}}$$

$$= \left[\left((.23/3.45)(3.45/3.40)\right)^2 + \left((.23/6.86)(6.86/3.40)\right)^2\right]^{\frac{1}{2}}$$

$$= \pm 9.6\% \quad . \qquad \text{(B-3)}$$

The uncertainty in V_o is calculated using B-2.

$$\frac{W_{V_o}}{V_o} = [(2.4\%)^2 + (9.6\%)^2 + (0\%)^2]^{\frac{1}{2}}$$

$$= \pm 9.7\% \quad (95\% \text{ confidence})$$

This uncertainty also is generally valid for all vortex ring cases since all vortices were magnified to approximately the same image size on the video screen.

B.2.4 Uncertainty in Kinematic Viscosity

$$\frac{W_\nu}{\nu} = \pm 1.8\% \quad (\text{corresponds to a } \pm 1°C \text{ error in temperature})$$

B.2.5 Uncertainty in Reynolds Number Re_o

The uncertainty in Re_o can be calculated using relation B-1 as

$$\frac{W_{Re_o}}{Re_o} = [(\frac{W_{D_o}}{D_o})^2 + (\frac{W_{V_o}}{V_o})^2 + (\frac{W_\nu}{\nu})^2]^{\frac{1}{2}}$$

$$= [(6.6\%)^2 + (9.7\%)^2 + (1.8\%)^2]^{\frac{1}{2}}$$

$$= \pm 12\% \quad (95\% \text{ confidence})$$

B.2.6 Uncertainty in the Normalized Time for Formation of the Secondary Vortex T_s

Relation 3-3 defining T_s is repeated below as B-4:

$$T_s = t_s V_o/D_o \qquad (B\text{-}4)$$

The uncertainty in T_s can be calculated as shown in B-5 from the uncertainties in V_o, D_o, and t_s.

$$\frac{W_{T_s}}{T_s} = [(W_{V_o}/V_o)^2 + (W_{D_o}/D_o)^2 + (W_{t_s}/t_s)^2]^{\frac{1}{2}} \qquad \text{(B-5)}$$

The uncertainty in t_s, W_{t_s}/t_s, is calculated in B-6 where t_s = 0.62 sec and the uncertainty at each end of the time interval is 0.025 sec.

$$\frac{W_{t_s}}{t_s} = [2((\partial t_s/\partial_t)(\partial_t/\ _t)^2]^{\frac{1}{2}} \qquad \text{(B-6)}$$

$$= [2\ (0.025/0.62)^2]^{\frac{1}{2}} = 5.7\% \quad \text{(95\% confidence)}$$

The uncertainty in T_s can now be calculated from B-5.

$$\frac{W_{T_s}}{T_s} = [(9.7\%)^2 + (6.6\%)^2 + (5.7\%)^2]^{\frac{1}{2}} \qquad \text{(B-7)}$$

$$= \pm 13\% \quad \text{(95\% confidence)}$$

This uncertainty level is generally valid for most of the vortex ring cases except the very low Reynolds number cases which are marked by solid symbols in Figure 3.24. For these cases an outer limit of the uncertainty may be estimated by a fourfold increase in the t_s uncertainty which would cause the uncertainty in T_s to double to a level of $\pm$26%. The reader should refer to section 3.16 for a discussion of this uncertainty.

B.2.7 Uncertainty in Circulation Measurements

B.2.7a Uncertainty in Γ_{BC}

The uncertainty reported here is an uncertainty in the measurements and does not reflect any error which may be present in the theory or method. See Appendix A for a discussion of possible error in this method. The source of greatest error is the T measurement, the vortex ring half thickness. In the wake region of the vortex ring, the dye

interface was often not sharply defined, which made it difficult to precisely determine the T measurements. The uncertainty in the T measurement is ±11% and is the source of a rather larger uncertainty in Γ_{BC}.

The uncertainty in Γ_{BC} is a function of the uncertainty in a/R, D_o, and V_o as shown in B-8:

$$\frac{W\Gamma_{BC}}{\Gamma_{BC}} = \left[\left(\frac{\partial\Gamma_{BC}}{\partial a/R} \cdot \frac{W_{a/R}}{\Gamma_{BC}}\right)^2 + \left(\frac{\partial\Gamma_{BC}}{\partial D_o} \cdot \frac{W_{D_o}}{\Gamma_{BC}}\right)^2 + \left(\frac{\partial\Gamma_{BC}}{\partial V_o} \cdot \frac{W_{V_o}}{\Gamma_{BC}}\right)^2\right]^{\frac{1}{2}} \qquad \text{(B-8)}$$

which reduces to B-9:

$$\frac{W\Gamma_{BC}}{\Gamma_{BC}} = \left[\left(\frac{1}{\ln(8/a/R) - 1/3} \cdot \frac{W_{a/R}}{a/R}\right)^2 + \left(1 \cdot \frac{W_{D_o}}{D_o}\right)^2 + \left(1 \cdot \frac{W_{V_o}}{V_o}\right)^2\right]^{\frac{1}{2}} \qquad \text{(B-9)}$$

The functional relationship between T/R' and a/R is unknown to this author, but is represented by the data in table A-1. Using this data and the 11% uncertainty in T/R' yields the rather large uncertainty in a/R of ±58%. Substituting into B-9 yields an uncertainty in Γ_{BC} of ±23% at a 95% confidence level as shown below.

$$\frac{W_{BC}}{BC} = \left[(.3455 \times 58\%)^2 + (6.6\%)^2 + (9.7\%)^2\right]^{\frac{1}{2}} \qquad \text{(B-10)}$$

$$= \pm 23\% \quad \text{(95\% confidence)}$$

B.2.7b Uncertainty in Γ_M

The uncertainty reported here is also measurement uncertainty and does not reflect any error in the theory. It should be recalled that Didden (13) found that Γ_M underestimated the circulation measured using a LDV by 30% to 60%.

Γ_M was calculated by numerically evaluating relation A-16 using the vortex generator piston displacement vs. time curve. The velocity $U_M(t_i)$ is calculated by applying a displacement calibration to the

displacement transducer data as shown in B-11.

$$U_M(t_i) = \frac{x(t_{i+1}) - x(t_{i-1})}{\Delta t} \text{ cal}_{\text{disp}} \qquad \text{(B-11)}$$

The only assumed uncertainty in U_M results from uncertainty in the displacement calibration. The largest uncertainty occurred for the smallest piston stroke and is equal to $\pm$10%. The uncertainty in U_M is therefore $\pm$10%. The uncertainty in Γ_M is calculated below in B-12.

$$\frac{W\Gamma_M}{\Gamma_M} = \left[\left(\frac{\partial \Gamma_M}{\partial U_M} \cdot \frac{W_{U_M}}{\Gamma_M}\right)^2\right]^{\frac{1}{2}} \qquad \text{(B-12)}$$

$$= 2\,\frac{W_{U_M}}{U_M} = \pm 20\% \quad \text{(95\% confidence)}$$

B.2.7c Uncertainty in Γ_B

Again, the uncertainty reported here is a measurement uncertainty only. To the authors' knowledge, no reports have been published in which this method was used successfully.

The uncertainty in Γ_B, which is determined using relation A-11, is a function of the uncertainty in d and θ as shown in B-13.

$$\frac{W\Gamma_B}{\Gamma_B} = \left[\left(\frac{\partial \Gamma_B}{\partial d} \cdot \frac{W_d}{\Gamma_B}\right)^2 + \left(\frac{\partial \Gamma_B}{\partial \theta} \cdot \frac{W_\theta}{\Gamma_B}\right)^2\right]^{\frac{1}{2}} \qquad \text{(B-13)}$$

The uncertainties in d and θ are respectively $\pm$20% and $\pm$8%. Substituting these quantities and solving for the partial derivatives yields:

$$\frac{W\Gamma_B}{\Gamma_B} = \left[(2 \cdot 20\%)^2 + (8\%)^2\right]^{\frac{1}{2}}$$

$$= \pm 41\% \quad \text{(95\% confidence)}$$

This uncertainty is valid for all the cases so studied.

APPENDIX C: EXPERIMENTAL DATA

The following data tables present the quantitative data obtained during the course of this study. Table C.2 tabulates the data for the quiescent flow cases, including impacts with both solid and free surfaces. Table C.3 tabulates data for the boundary layer flow cases.

Each vortex case is identified by a five digit number which gives an indication of the generation parameters. The first digit indicates the orifice size, D_M, and ranges from 1 to 7 corresponding to orifice diameters of 0.95 to 3.81 cm. The D_M for each orifice size is listed in the table. The second and third digits correspond to L_M/D_M rounded to two digits. The fourth and fifth digits indicate the speed control setting for the electric motor used to drive the vortex generator.

Dashes in the data table indicate either no data was available for that case, or that measurement was not relevant to the particular vortex case.

At the bottom of each column are listed abbreviations under the heading "Comments". These abbreviations, which are explained in Table C.1, are not meant to give the reader a comprehensive description of the flow phenomenon for a particular case, but rather an indication of the general flow behavior. Only the most relevant abbreviations which best define the behavior for each case are included.

Table C.1 Flow Behavior Abbreviations and Their Definitions

WPVRNC	-	Weak Primary Vortex Ring Not Coherent. The PVR so formed was not coherent, unstable, and generally of no usefulness in this study.
WPVRCS	-	Weak Primary Vortex Ring Coherent and Stable. A Weak PVR, generally did not form a SVR.
LAMDIF	-	Laminar Diffusion. The PVR dispersed its vorticity by laminar diffusion.
NOSVR	-	No SVR was formed.
APPSEP	-	Apparent Separation. The boundary layer created by the PVR appeared to separate, but did not roll up into an SVR.
VWSVR	-	Very Weak SVR. The separated boundary layer had sufficient strength to just about roll up into a SVR. The fluid generally made one or slightly more revolutions in the SVR.
WSVR	-	Weak SVR. The SVR formed a very coherent ring but was very weak in comparison to the PVR.
SVR	-	SVR. The SVR interacted with the PVR in a significant manner.
RBND	-	Rebound. Rebound occurred in the trajectory of the PVR.
RVRSL	-	Reversal. Reversal occurred in the trajectory of the PVR.
LOOP	-	Loop-Structured SVR was formed.
UND	-	Under. Some of the loops of the loop-structured SVR would be pulled beneath the core of the PVR.
UP	-	Up. Some of the loops of the loop-structured SVR would propagate vertically in the center of the PVR which resulted in the stretching of the SVR.
L-KTRN	-	Loop to Kink Transition. The SVR would be in transition between a loop and a kink structure.

KINK - A Kink-Structured SVR was formed.

EJECT - Secondary Vortex Ring Ejection occurred.

TVR - Tertiary Vortex Ring.

MVR - Multiple Vortex Rings. Multiple vortex rings would form at the orifice if the ejected fluid slug was excessively long and/or ejected at too high a velocity.

TRB@FO - Turbulent at Formation. The PVR was turbulent at its formation.

UNSTBL - Unstable. The PVR was unstable before impact with the surface.

SHDVRT - Sheds Vorticity. The PVR would shed much vorticity into its wake as it propagated towards the surface.

AZWVIN - Azimuthal Waviness Instability. The PVR displayed an instability which was characterized by the azimuthal waviness observed by Maxworthy (53) and others as it approached the surface. This usually caused an immediate azimuthal waviness in the SVR when it was formed.

RADDSP - Rapid Dispersal. The PVR was dispersed in an almost explosive manner almost immediately after the formation of the SVR.

? - The question mark in conjunction with any of the above abbreviations indicates an uncertainty in the observation.

Table C.2 Experimental Data - Quiescent Flow Case

Vortex ID #	12.920	12.630	13.040	12.450	12.660	20.940	20.940
Piston Dia(cm)	1.90	1.90	1.90	1.90	1.90	1.90	1.90
Spd Cntrl #	20	30	40	50	60	40A	40B
Water Temp(c)	22.2	23.3	22.2	23.3	23.3	22.2	22.2
D_M (cm)	0.95	0.95	0.95	0.95	0.95	1.43	1.43
H_M/D_M	4.16	4.16	6.83	6.83	6.83	4.55	4.55
L_M/D_M	2.88	2.56	2.99	2.41	2.36	0.92	0.89
U_M (cm/s)	4.45	5.80	9.25	8.72	8.32	4.14	6.37
D_O (cm)	1.12	1.00	1.14	0.99	.91	1.06	1.02
T/R'	.677	.622	.659	.635	.652	.540	-
U_O (cm/s)	2.64	3.43	7.32	4.93	8.69	1.15	1.45
N	0	5,5	6,6	6,5,6	6,6,6	0	0
T_S	1.5	2.0	1.5	1.6	2.5	-	-
Re_o	313	376	880	537	867	129	155
Re_M	447	603	929	907	865	624	960
Γ_M (cm/s^2)	5.51	7.2	13.1	9.12	8.98	2.71	3.83
Γ_{BC} (cm/s^2)	8.86	8.35	23.34	12.6	21.6	2.32	-
Comments:	LAMDIF APPSEP RBND	LAMDIF APPSEP VWSVR	LOOP UND MVR UNSTBL	RBND RVRSL SVR TVR ?UNSTBL ?AZWVIN	LAMDIF LOOP AZWVIN UNSTBL	WPVRCS LAMDIF NOSVR APPSEP RBND	WPVRNC UNSTBL

Table-C.2 Experimental Data - Quiescent Flow Case

Vortex ID #	20.960	20.960	20.970	21.615	21.725	21.635	21.650
Piston Dia(cm)	1.90	1.90	1.90	1.90	1.90	1.90	1.90
Spd Cntrl #	60A	60N	70	15	25	35	50
Water Temp(c)	22.2	22.2	22.2	22.2	22.2	22.2	22.2
D_M (cm)	1.43	1.43	1.43	1.43	1.43	1.43	1.43
H_M/D_M	4.55	4.55	4.55	4.55	4.55	4.55	4.55
L_M/D_M	0.89	0.85	0.89	1.61	1.71	1.64	1.64
U_M (cm/s)	4.55	8.09	4.50	2.28	5.47	7.40	8.83
D_O (cm)	1.07	1.07	1.19	1.64	1.47	1.32	1.32
T/R'	0.617	-	0.56	0.541	0.615	0.619	0.62
U_O (cm/s)	1.12	-	1.47	0.61	2.37	3.40	4.50
N	0	-	-	0	0	7,6	7,7,7
T_S	-	-	-	-	1.4	1.3	1.5
Re_o	126	-	186	105	369	474	626
Re_M	686	1219	678	344	824	1115	1263
Γ_M (cm/s^2)	3.01	4.66	2.90	2.30	6.02	7.87	9.55
Γ_{BC} (cm/s^2)	2.84	-	3.50	1.89	8.28	10.78	14.3
Comments:	WPVRCS LAMDIF APPSEP RBND	WPVRNC TRB@FO MVR UNSTBL	MVR UNSTBL	WPVRCS LAMDIF APPSEP RBND	WPVRCS LAMDIF APPSEP RBND	SVR RBND LOOP UND&UP TVR	SVR RBND ?RVRSL LOOP UND&UP TVR

Table-C.2 Experimental Data - Quiescent Flow Case

Vortex ID #	21.675	22.418	22.525	22.433	22.545	22.475	23.215
Piston Dia(cm)	1.90	1.90	1.90	1.90	1.90	1.90	1.90
Spd Cntrl #	75	18	25	33	45	75	15
Water Temp(c)	22.2	22.2	22.2	22.2	22.2	22.2	21.7
D_M (cm)	1.43	1.43	1.43	1.43	1.43	1.43	1.43
H_M/D_M	4.55	4.55	4.55	4.55	4.55	4.55	4.55
L_M/D_M	1.64	2.40	2.47	2.40	2.47	2.44	3.16
U_M (cm/s)	8.89	3.71	6.22	8.12	10.7	10.9	2.85
D_O (cm)	1.32	1.63	1.65	1.63	1.68	1.50	1.75
T/R'	0.626	0.65	0.688	0.647	0.611	0.618	0.68
U_O (cm/s)	4.52	1.34	3.40	4.42	6.27	7.21	1.40
N	6677	-	6	666	6	6	0
T_S	1.5	-	1.5	1.3	1.1	1.4	1.5
Re_o	630	230	593	758	1109	1140	254
Re_M	1340	559	937	1224	1613	1643	422
Γ_M (cm/s^2)	9.62	5.53	9.53	12.5	16.9	17.4	5.64
Γ_{BC} (cm/s^2)	14.7	5.90	17.4	19.2	24.5	25.9	7.42
Comments:	SVR	LAMDIF	SVR	SVR	RBND	RVRSL	WPVRCS
	RBND	APPSEP	RBND	RBND	RVRSL	LOOP	LAMDIF
	RVRSL	RBND	?RVRSL	?RVRSL	LOOP	UND&UP	?APPSEP
	LOOP		LOOP	LOOP	UND&UP	TVR	RBND
	UND&UP		UND&UP	UND&UP	TVR	TRB@FO	
	TVR		TVR	TVR	SHDVRT	SHDVRT	

Table-C.2 Experimental Data - Quiescent Flow Case

Vortex ID #	23.225	23.230	23.050	23.425	22.850	31.230	31.255
Piston Dia(cm)	1.90	1.90	1.90	3.81	3.81	3.81	3.81
Spd Contrl #	25	30	50	25	50	30	55
Water Temp(c)	21.7	21.7	21.7	18.9	18.9	18.9	18.9
D_M (cm)	1.43	1.43	1.43	1.43	1.43	1.90	1.90
H_M/D_M	4.55	4.55	4.55	4.55	4.55	4.75	4.75
L_M/D_M	3.22	3.22	3.04	3.41	2.77	1.17	1.17
U_M (cm/s)	7.23	8.94	18.3	8.43	18.4	8.40	11.0
D_o (cm)	1.60	1.73	1.73	1.83	1.75	1.85	1.80
T/R'	0.646	0.601	0.550	0.587	0.628	0.619	0.571
U_o (cm/s)	3.94	5.21	9.98	5.72	12.4	4.06	4.75
N	6	-	-	8.8	?	8888	8,8
T_S	0.69	1.2	0.98	1.0	1.4	1.6	1.3
Re_o	654	933	1786	1015	2118	731	832
Re_M	1072	1325	2712	1170	2552	1554	2034
Γ_M (cm/s^2)	14.6	18.2	35.7	20.3	32.0	8.96	10.5
Γ_{BC} (cm/s^2)	16.8	20.2	33.5	22.4	54.1	18.1	17.5
Comments:	TRB@FC	MVR	MVR	MVR	MVR	SVR	SVR
	UNSTBL	UNSTBL	TRB@FO	UNSTBL	UNSTBL	RBND	RBND
	SHDVRT	LOOP	UNSTBL			LOOP	LOOP
	SVR	UND&UP	SVR			UND&UP	UND&UP
	TVR	RBND				TVR	TVR
	?RVRSL	?RVRSL					

Table-C.2 Experimental Data - Quiescent Flow Case

Vortex ID #	31.330	31.355	32.225	32.450	32.225	32.455	32.825
Piston Dia(cm)	1.90	1.90	2.54	2.54	5.08	5.08	3.81
Spd Contrl #	30	55	25	50	25	55	25
Water Temp (c)	20.6	20.6	18.9	18.9	19.4	19.4	18.9
D_M (cm)	1.90	1.90	1.90	1.90	1.90	1.90	1.9
H_M/D_M	4.75	4.75	4.75	4.75	4.75	4.75	4.75
L_M/D_M	1.31	1.29	2.23	2.37	2.19	2.37	2.83
U_M (cm/s)	5.69	7.07	5.56	12.6	12.2	18.3	10.6
D_o (cm)	1.73	1.88	2.13	2.13	2.03	2.29	1.96
T/R'	0.60	0.619	0.648	0.588	0.593	0.576	0.663
U_o (cm/s)	2.69	3.76	2.69	8.13	6.60	11.53	5.51
N	7	77	6,7,7	8	-	8	5,6,6
T_S	1.7	1.5	1,3	1.3	1.2	0.91	1.1
Re_o	470	714	558	1684	1322	2597	1047
Re_M	1095	1360	1028	2330	2290	3440	1960
Γ_M (cm/s^2)	6.47	8.66	10.6	24.8	22.8	35.7	25.5
Γ_{BC} (cm/s^2)	10.43	16.9	15.4	37.4	29.4	54.7	30.6
Comments:	APPSEP VWSVR RBND	SVR LOOP UND&UP RBND TVR	SVR LOOP AZWVIN	SVR LOOP AZWVIN	SVR RBND LOOP AZWVIN	AZWVIN UNSTBL	SVR MVR L-KTRN RVRSL

Table-C.2 Experimental Data - Quiescent Flow Case

Vortex ID #	32.650	40.925	40.860	41.325	41.555	41.525	41.555
Piston Dia(cm)	3.81	3.81	3.81	5.08	5.08	2.54	2.54
Spd Contrl # .	50	25	60	25	55	25	55
Water Temp (c)	18.9	18.9	18.9	15.6	15.6	18.9	18.9
D_M (cm)	1.9	2.22	2.22	2.22	2.22	2.22	2.22
H_M/D_M	4.75	4.07	4.07	4.07	4.07	4.07	4.07
L_M/D_M	2.61	0.87	0.78	1.26	1.50	1.45	1.50
U_M (cm/s)	19.1	4.88	6.00	7.84	13.0	5.29	9.64
D_o (cm)	2.16	2.16	1.80	2.21	2.21	2.74	2.16
T/R'	0.593	0.584	0.565	0.576	0.548	0.625	0.619
U_o (cm/s)	9.30	1.65	2.49	3.81	7.62	2.46	5.13
N	8	0	7,8	8,9,9	9,9,9	7,7,7	8,8,8
T_S	1.4	1.4	1.7	1.1	1.2	1.4	1.3
Re_o	1949	347	437	752	1503	535	1075
Re_M	3533	1053	1295	1556	2580	1140	2080
Γ_M (cm/s^2)	40.2	4.18	4.89	9.91	18.7	7.57	13.9
Γ_{BC} (cm/s^2)	43.9	7.59	9.06	17.5	32.5	13.5	26.6
Comments:	SVR	LAMDIF	SVR	TRB@FO	SHDVRT	SVR	SVR
	MVR	APPSEP	RBND	SVR	?TRB@FO	RBND	RVRSL
	RADDSP	VWSVR	LOOP	RBND	SVR	LOOP	LOOP
	TVR	RBND	UND&UP	?RVRSL	RVRSL	TVR	
	L-KTRN			LOOP	LOOP		
				TVR	TVR		

Table C.2 Experimental Data - Quiescent Flow Case

Vortex ID #	41.830	41.745	42.625	42.545	50.835	50.845	50.625
Piston Dia(cm)	3.81	3.81	3.81	3.81	2.54	2.54	3.81
Spd Contrl #	30	45B	25	45	35	45	25
Water Temp (c)	22.2	22.2	19.4	19.4	19.4	19.4	22.2
D_M (cm)	2.22	2.22	2.22	2.22	2.54	2.54	2.54
H_M/D_M	4.07	4.07	4.07	4.07	3.56	3.56	3.56
L_M/D_M	1.75	1.65	2.55	2.46	0.76	0.75	.63
U_M (cm/s)	10.0	20.0	9.77	16.9	4.93	5.74	3.22
D_o (cm)	2.24	2.18	2.57	2.54	1.85	1.98	1.35
T/R'	0.603	0.569	0.631	0.576	0.568	0.624	0.603
U_o (cm/s)	5.28	10.2	5.94	10.4	1.95	2.45	0.88
N	9,9,9	991010	77788	8,8	0	7	0
T_S	1.3	1.3	1.1	1.2	2.1	1.7	-
Re_o	1246	2353	1502	2593	356	479	126
Re_M	2344	4689	2139	3700	1234	1436	862
Γ_M (cm/s^2)	17.1	29.9	24.3	39.7	4.15	4.84	2.56
Γ_{BC} (cm/s^2)	26.7	45.4	38.3	54.6	7.33	11.9	2.69
Comments:	SVR RVRSL LOOP TVR	SVR RVRSL L-KTRN UND&UP	SVR RVRSL L-KTRN UND&UP	MVR ?UNSTBL SVR L-KTRN TVR	LAMDIF APPSEP ?VWSVR RBND	WSVR RBND LOOP TVR ?AZWVIN	WPVRCS LAMDIF APPSEP RBND

Table C.2 Experimental Data - Quiescent Flow Case

Vortex ID #	50.640	50.560	51.115	51.120	51.130	51.145	51.160
Piston Dia(cm)	3.81	3.81	3.81	3.81	3.81	3.81	3.81
Spd Contrl #	40	60	15	20B	30B	45	60B
Water Temp (c)	22.2	22.2	22.2	22.2	22.2	22.2	22.2
D_M (cm)	2.54	2.54	2.54	2.54	2.54	2.54	2.54
H_M/D_M	3.56	3.56	3.56	3.56	3.56	3.56	3.56
L_M/D_M	.61	0.54	1.15	1.13	1.08	1.13	1.08
U_M (cm/s)	4.65	4.83	3.36	4.95	7.70	9.43	17.9
D_o (cm)	1.96	1.22	2.67	2.57	2.57	2.33	2.26
T/R'	0.593	0.569	0.530	0.55	0.589	0.566	0.529
U_o (cm/s)	1.38	1.26	.937	2.08	3.00	4.06	7.29
N	0	02?	0,2?	7	889910	88910	9,10
T_S	-	2.3	1.1	1.5	1.1	1.2	1.2
Re_o	284	162	264	562	811	999	1680
Re_M	1246	1294	900	1326	2063	2527	4796
Γ_M (cm/s^2)	3.47	3.25	4.36	6.58	9.39	11.97	19.97
Γ_{BC} (cm/s^2)	5.89	2.96	4.64	10.3	16.6	19.1	30.5
Comments:	LAMDIF APPSEP ?VWSVR RBND	LAMDIF APPSEP ?VWSVR RBND	LAMDIF APPSEP RBND	WSVR RBND LOOP UND TVR	SVR RVRSL LOOP UND&UP TVR	SVR RVRSL LOOP UND&UP TVR	SVR RVRSL LOOP UND&UP TVR SHDVRT

Table C.2 Experimental Data - Quiescent Flow Case

Vortex ID #	51.620	51.625	51.530	51.640	51.665	52.218	52.220
Piston Dia(cm)	3.81	3.81	3.81	3.81	3.81	3.81	3.81
Spd Contrl #	20B	25B	30B	40B	65B	18	20B
Water Temp (c)	22.2	22.2	22.2	22.2	22.2	22.2	22.2
D_M (cm)	2.54	2.54	2.54	2.54	2.54	2.54	2.54
H_M/D_M	3.56	3.56	3.56	3.56	3.56	3.56	3.56
L_M/D_M	1.55	1.62	1.51	1.60	1.60	2.18	2.18
U_M (cm/s)	4.14	7.62	9.24	12.9	19.5	4.91	5.09
D_o (cm)	2.57	2.74	2.64	2.77	2.57	3.12	3.10
T/R'	0.599	0.575	0.605	0.588	0.586	0.620	0.60
U_o (cm/s)	1.67	3.40	4.80	5.59	8.38	1.75	3.00
N	8	8	99	991012	9910	67	7788
T_S	1.4	1.2	1.4	1.2	1.1	1.1	1.1
Re_o	451	985	1338	1632	2268	564	980
Re_M	1109	2042	2476	3456	5225	1316	1364
Γ_M (cm/s^2)	7.32	13.3	15.0	22.1	33.5	12.1	12.6
Γ_{BC} (cm/s^2)	9.55	19.3	28.9	33.3	46.1	13.2	20.8
Comments:	WSVR RBND RVRSL LOOP UND&UP TVR	SVR RVRSL LOOP UND&UP	SVR RVRSL LOOP UND&UP TVR	SVR RVRSL L-KTRN UP TVR	SVR RVRSL L-KTRN TVR	SVR RBND LOOP UND TVR SHDVRT	SVR RVRSL LOOP UND&UP TVR

Table C.2 Experimental Data - Quiescent Flow Case

Vortex ID #	52.235	52.250	52.265	52.265	52.170	51.035	52.030
Piston Dia(cm)	3.81	3.81	3.81	3.81	3.81	5.08	5.08
Spd Contrl #	35	50	65	65	70B	35	30
Water Temp (c)	22.2	22.2	22.2	25	22.2	17.5	17.8
D_M (cm)	2.54	2.54	2.54	2.54	2.54	2.54	2.54
H_M/D_M	3.56	3.56	3.56	3.56	3.56	3.56	3.56
L_M/D_M	2.20	2.16	2.16	2.25	2.12	0.96	2.0
U_M (cm/s)	10.9	15.8	16.6	-	23.2	8.74	14.0
D_o (cm)	3.05	2.79	2.79	2.82	3.28	2.31	2.69
T/R'	0.591	0.596	0.605	-	0.649	0.572	0.574
U_o (cm/s)	6.65	8.56	9.14	9.25	14.3	3.63	7.26
N	91010	101012	-	-	8	8,8,9	8,8
T_S	1.4	1.1	1.1	-	1.2	1.1	1.2
Re_o	2140	2546	2842	2962	4943	786	1845
Re_M	2921	4233	4448	-	6216	2080	3355
Γ_M (cm/s^2)	25.9	37.4	39.4	-	53.7	9.58	31.8
Γ_{BC} (cm/s^2)	44.2	52.9	61.5	-	126.2	17.2	40.32
Comments:	SVR RVRSL L-KTRN ?EJECT UND&UP	SVR RVRSL KINK EJECT SHDVRT TVR	SVR RVRSL KINK EJECT SHDVRT TVR	SVR RVRSL KINK EJECT SHDVRT TVR	?TRB@FO ?UNSTBL ?AZWVIN RADDSP ?EJECT	SVR RVRSL LOOP UND&UP TVR SHDVRT	UNSTBL AZWVIN RVRSL LOOP

Table C.2 Experimental Data - Quiescent Flow Case

Vortex ID #	52.155	52.930	53.055	51.825	60.840	61.135	70.940
Piston Dia(cm)	5.08	5.08	5.08	3.81	3.81	3.81	5.08
Spd Contrl #	55	30	55	25	40	35	40
Water Temp (c)	17.8	21.1	21.1	25	19.4	19.2	21.1
D_M (cm)	2.54	2.54	2.54	2.54	3.18	3.18	3.81
H_M/D_M	3.56	4.56	4.56	3.50	2.85	2.85	3.04
L_M/D_M	2.08	2.92	2.96	1.80	0.84	1.12	0.89
U_M (cm/s)	19.9	15.6	23.3	8.72	6.92	7.92	9.08
D_o (cm)	3.02	3.12	3.10	2.67	2.92	3.20	3.38
T/R'	0.609	0.554	0.597	0.557	0.539	0.565	0.525
U_o (cm/s)	12.3	9.70	15.8	3.96	2.26	2.64	2.84
N	8	8	-	8	6,7	-	10,9
T_S	1.1	1.1	1.2	1.2/1.14	1.1	1.0	1.1
Re_o	3505	3093	4987	1201	651	827	981
Re_M	4768	4043	6039	2517	2165	2460	3530
Γ_M (cm/s^2)	45.5	51.5	78.1	17.1	7.88	12.0	13.6
Γ_{BC} (cm/s^2)	86.0	59.39	108.4	20.9	12.5	17.02	17.7
Comments:	UNSTBL ?AXWVIN RVRSL LOOP TVR	UNSTBL TRB@FO MVR ?AZWVIN	UNSTBL TRB@FO AXWVIN	SOLID/ FREE SURFACE RVRSL LOOP UND	SVR RBND LOOP UND&UP	SVR RBND LOOP UND&UP TVR	WSVR RVRSL LOOP TVR

Table C.2 Experimental Data - Quiescent Flow Case

Vortex ID #	51.245	32.825	21.635	31.340
Piston Dia (cm)	3.81	3.81	1.90	1.90
Spd Contrl #	45	25	35	40
Water Temp (c)	17.8	20	20	20.6
D_M (cm)	2.54	1.90	1.43	1.90
H_M/D_M	3.56	4.75	4.55	4.75
L_M/D_M	1.17	2.83	1.64	1.33
U_M (cm/s)	10.7	11.7	7.58	6.34
D_o (cm)	2.49	2.29	1.50	2.01
T/R'	0.447	0.469	0.510	0.525
U_o (cm/s)	4.01	4.85	3.05	2.67
N	-	-	-	-
T_S	1.2	0.96	1.1	1.3
Re_o	942	1109	457	541
Re_M	2564	2229	1083	1220
Γ_M (cm/s^2)	13.3	27.4	8.08	7.09
Γ_{BC} (cm/s^2)	15.4	18.1	8.12	9.84
Comments:	Γ_B=7.74	Γ_B=11.2	Γ_B=4.71	Γ_B=5.82
	$\frac{d}{D_o}$=0.11	$\frac{d}{D_o}$=.086	$\frac{d}{D_o}$=0.11	$\frac{d}{Do}$=0.11
	BUBBLE VISUAL-IZATION	BUBBLE VISUAL-IZATION	BUBBLE VISUAL-IZATION	BUBBLE VISUAL-IZATION

Table C.3 Experimental Data - Boundary Layer Flow Case

Vortex ID #	11.728	13.030	13.125
Piston Dia(cm)	1.90	1.90	1.90
Spd Contrl #	28	30	25
Water Temp (c)	24.5	24.5	24.5
D_M (cm)	0.95	0.95	0.95
H_M/D_M	6.85	6.85	6.85
L_M/D_M	1.71	2.99	3.09
U_M (cm/s)	5.03	8.53	5.98
D_o (cm)	0.91	-	-
T/R'	0.502	-	-
U_o (cm/s)	5.51	-	-
N	7	-	-
δ (cm)	3.8	3.8	3.8
Re_o	567	-	-
Re_M	539	914	641
Γ_M (cm/s^2)	6.82	11.2	8.78
Γ_{BC} (cm/s^2)	8.83	-	-
U_∞ (cm/s)	4.08	4.08	4.08
U_{carr} (cm/s)	3.81	3.81	3.81

Table C.3 Experimental Data - Boundary Layer Flow Case

Vortex ID #	31.323	31.219	31.626	31.730	31.735	31.740
Piston Dia (cm)	3.81	3.81	3.81	3.81	3.81	3.81
Spd Contrl #	23	19	26	30	35	40
Water Temp (c)	23	24	24	24	24	24
D_M (cm)	1.90	1.90	1.90	1.90	1.90	1.90
H_M/D_M	4.75	4.75	4.75	4.75	4.75	4.75
L_M/D_M	1.33	1.17	1.65	1.71	1.71	1.71
U_M (cm/s)	7.68	5.78	7.58	7.72	9.50	11.04
D_o (cm)	1.90	-	-	-	-	-
T/R'	0.546	-	-	-	-	-
U_o (cm/s)	3.53	-	-	-	-	-
N	-	-	-	-	-	-
δ (cm)	3.8	3.8	3.8	3.8	3.8	3.8
Re_o	727	-	-	-	-	-
Re_M	1581	1226	1608	1638	2015	2342
Γ_M (cm/s^2)	8.56	6.07	11.11	12.74	14.6	16.2
Γ_{BC} (cm/s^2)	12.9	-	-	-	-	-
U_∞ (cm/s)	4.08	4.08	4.08	4.08	4.08	4.08
U_{carr} (cm/s)	3.81	3.81	3.81	3.81	3.81	3.81

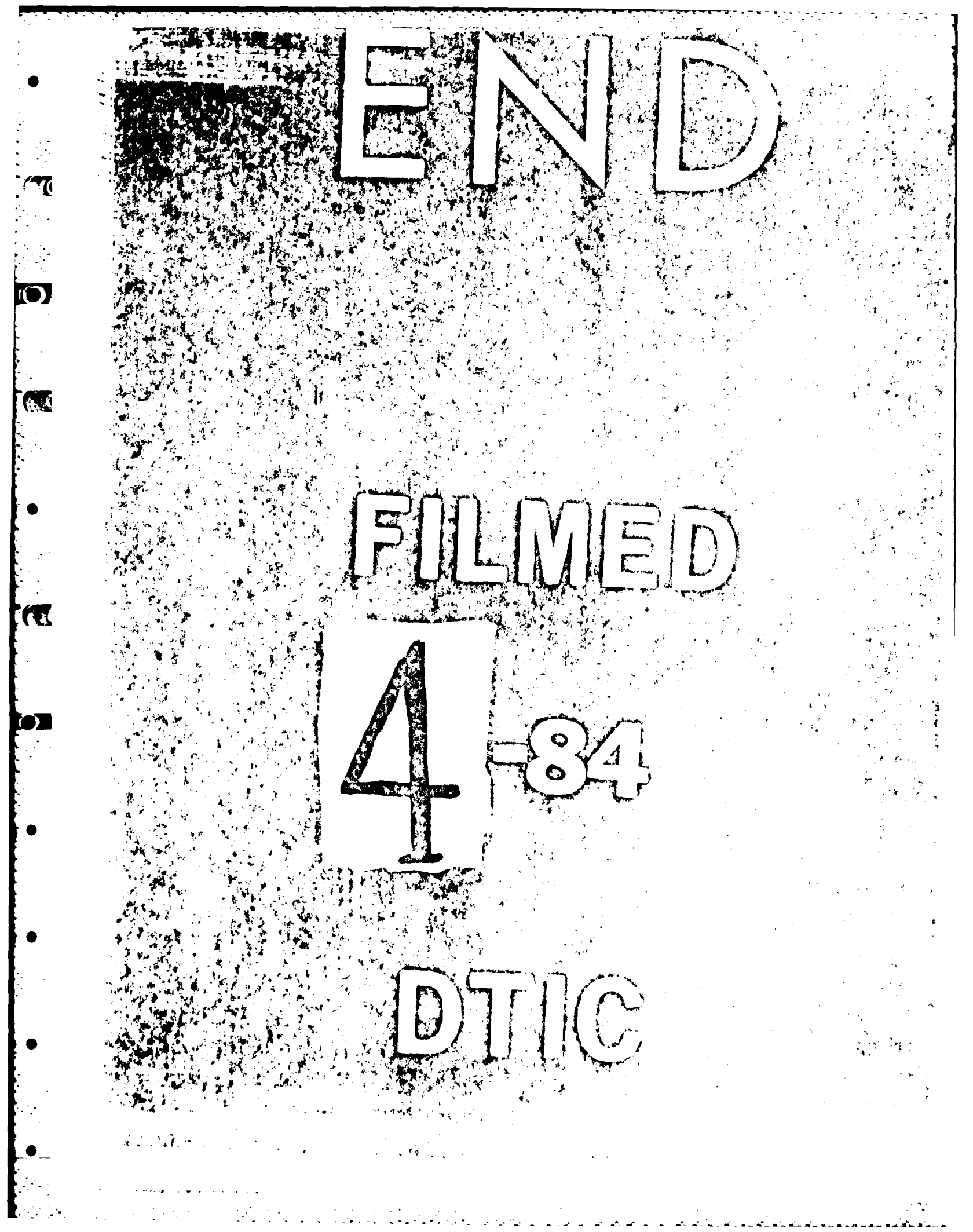
END
FILMED
4-84
DTIC